Technische Universität München
Max-Planck–Institut für Quantenoptik

Quantum Simulations of Out-of-Equilibrium Phenomena

Birger Christian Helge Horstmann

Vollständiger Abdruck der von der Fakultät für Physik
der Technischen Universität München
zur Erlangung des akademischen Grades eines

Doktors der Naturwissenschaften (Dr. rer. nat.)

genehmigten Dissertation.

Vorsitzende : Univ.-Prof. Dr. K. Krischer

Prüfer der Dissertation : 1. Hon.-Prof. I. Cirac, Ph.D.

2. Univ.-Prof. J. von Delft, Ph.D.
Ludwig-Maximilians-Universität München

Die Dissertation wurde am 07.03.2011 bei der
Technischen Universität München eingereicht und
durch die Fakultät für Physik am 30.03.2011 angenommen.

Abstract

The quantum world contains many counterintuitive phenomena and triggers the development of new technologies. Unfortunately, in most cases classical numerical simulations of quantum systems are intractable. A quantum simulator addresses this problem by running the simulation on a quantum system. In this thesis we discuss three proposals for quantum simulators of the following out-of-equilibrium phenomena: Anderson localization in disordered systems, dissipative quantum phase transitions, and Hawking radiation emitted by black holes.

We propose to realize Anderson localization of ultracold atoms in an optical lattice with a disorder potential generated via a secondary species frozen in a superposition of random configurations. We investigate two preparation schemes: the independent preparation of both species and the transfer of a part of the population into a different internal state, for bosonic gases with infinite and weak intra-species interactions. In all setups we observe dynamical localization, i.e., the wavefunctions of the steady states feature exponential tails and reduced coherence.

In a second proposal we study the dynamics of systems with quantum phase transitions in contact with a Markovian, i.e., memoryless, bath. For exactly solvable spin systems, e.g., the anisotropic XY chain, we derive a closed equation for the dynamics of the second moments. We find that the asymptotic decoherence rates of the dissipative dynamics reflect a quantum phase transition in the system and are related to ground state properties.

Finally, we discuss a proposal for the simulation of acoustic black holes with ions trapped on a ring geometry. If the ions are rotating with a stationary and inhomogeneous velocity profile, regions can appear where the ion velocity exceeds the group velocity of the phonons. In these regions phonons are trapped like light in black holes, even though they are described by a discrete field theory with a nonlinear dispersion relation. We

study the appearance of Hawking radiation in this setup and propose a scheme to detect it. The generation of entanglement between the inside and the outside of the black hole signals the quantum nature of this radiation.

Zusammenfassung

Die Welt der kleinen Teilchen, die Quantenwelt, überrascht mit vielen unerwarteten Phänomenen und ermöglicht neue technische Anwendungen. Die Möglichkeiten klassischer numerischer Simulationen sind bei vielen interessanten Quantensystemen jedoch sehr eingeschränkt. Ein Quantensimulator umgeht dieses Problem dadurch, dass die Simulation selbst auf einem Quantensystem abläuft. In dieser Doktorarbeit stellen wir drei Vorschläge für Quantensimulatoren folgender dynamischer Effekte vor: Anderson Lokalisierung in ungeordneten Systemen, dissipative Quantenphasenübergänge und Hawkingstrahlung aus schwarzen Löchern.

Wir schlagen vor, Anderson Lokalisierung von kalten Atomen in optischen Gittern mit einem ungeordneten Potential zu realisieren, das durch eine zweite, in einer Superposition von zufälligen Konfigurationen eingefrorenen, Teilchenart erzeugt wird. Wir untersuchen zwei mögliche Initialisierungen: die unabhängige Präparierung beider Teilchenarten und den teilweisen Transfer von Atomen in einen anderen internen Zustand, für bosonische Gase mit unendlich starken und mit schwachen Wechselwirkungen. In allen untersuchten Anordnungen ist dynamische Lokalisierung zu beobachten, d.h. die Wellenfunktionen der stationären Zustände fallen exponentiell ab und ihre Kohärenz ist verringert.

In einem zweiten Vorschlag betrachten wir die Dynamik von Systemen mit Quantenphasenübergängen, wenn diese mit einem Markovschen Bad, einer Umgebung ohne Erinnerung, in Kontakt sind. Für exakt lösbare Systeme, z.B. die anisotrope XY Kette, leiten wir eine geschlossene Differentialgleichung für die Dynamik der zweiten Momente her. Wir können zeigen, dass die asymptotische Dekohärenzrate der dissipativen Dynamik einen Quantenphasenübergang des Systems widerspiegelt. Darüber hinaus entsprechen sie Grundzustandseigenschaften des Systems.

Schließlich schlagen wir vor, akustische schwarze Löcher mit Ionen in einer Ringfalle zu simulieren. Wenn die Ionen mit einem stationären und

inhomogenen Geschwindigkeitsprofil rotieren, können Bereiche entstehen, in denen die Ionengeschwindigkeit größer als die Gruppengeschwindigkeit der Phononen ist. Obwohl sie durch eine diskrete Feldtheorie mit nichtlinearer Dispersionsrelation beschrieben werden, sind die Phononen in diesen Bereichen gefangen, so wie Licht in schwarzen Löchern. Wir untersuchen die Emission von Hawkingstrahlung in dieser Anordnung und diskutieren ihre Messung. Die Erzeugung von Verschränkung zwischen dem Inneren und dem Äußeren des schwarzen Loches zeigt uns die Quantennatur dieser Strahlung.

Publications

HCR07 B. Horstmann, J.I. Cirac, and T. Roscilde, *Dynamics of localization phenomena for hard-core bosons in optical lattices*, Phys. Rev. A **76**, 043625 (2007).

HRF$^+$10 B. Horstmann, B. Reznik, S. Fagnocchi, and J.I. Cirac, *Hawking Radiation from an Acoustic Black Hole on an Ion Ring*, Phys. Rev. Lett **104**, 250403 (2010).

HDR10 B. Horstmann, S. Dürr, and T. Roscilde, *Localization of Cold Atoms in State-Dependent Optical Lattices via a Rabi Pulse*, Phys. Rev. Lett. **105**, 160402 (2010).

HSR$^+$11 B. Horstmann, R. Schützhold, B. Reznik, S. Fagnocchi, and J.I. Cirac, *Hawking Radiation on an Ion Ring in the Quantum Regime*, New J. Phys. **13**, 045008 (2011).

HC11 B. Horstmann and J.I. Cirac, *Decoherence Dynamics and Quantum Phase Transitions*, to appear soon (2011).

Contents

Chapter 1

Introduction

This thesis is a contribution to the rapidly expanding field of *quantum simulations* [BN09, FT10]. In the following I will first pay tribute to the foundations of this research field and summarize the main results, before introducing my proposals for quantum simulations of out-of-equilibrium systems with ultracold atoms in artificial crystals of light, i.e., optical lattices, and trapped ions.

A quantum simulator is a quantum system that can solve quantum models. The description of reality with quantum theory was boosted by Schrödinger [Sch26] and Heisenberg [Hei25] in 1925. This description and its extensions make fascinating and counterintuitive predictions for the physics on small scales, e.g. for atoms, ions, electrons, quarks, photons, which have been confirmed again and again with unprecedented accuracy. The complexity of important (quantum) systems, e.g., strongly-interacting electrons in solids, quantum magnets undergoing phase transitions, and out-of-equilibrium systems, makes it unavoidable to create simplified effective model descriptions of reality. Furthermore, in the iterative refinement process (via simulations) of matching model and reality one can achieve an improved understanding of the (quantum) physical mechanisms.

Unfortunately, it is often a challenging task to determine the predictions of quantum models. Only for the simplest quantum models exact analytic solutions are at our disposal, and often perturbation theory is not applicable in the most interesting situations due to the lack of small parameters. The direct treatment of quantum systems with classical computers is often intractable, which can be illustrated by the *exponential explosion* [Fey82] of the memory size and processing time required for an arbitrary many-body quantum state. For example, the state of N spin-1/2

particles requires the storage of 2^N complex numbers and its processing requires the manipulation of a $2^N \times 2^N$ matrix. Another approach for the simulation of quantum systems is the use of approximate numerical techniques, among which quantum Monte Carlo methods (MC) and projected entangled pair state algorithms (PEPS), including density matrix renormalization group and matrix product state algorithms, are the most popular. However, both of them have severe limitations: MC is not suited for fermionic or frustrated systems, in more than one dimension PEPSs are so far limited to relatively small systems.

These difficulties in simulating quantum models could be overcome with a quantum simulator, an idea first put forward by Feynman [Fey82] in 1982. A quantum simulator is a quantum system that is described by a given model Hamiltonian, circumventing the exponential explosion by exploiting the quantum nature of the simulator. The key requirement for a quantum simulator is its *controllability*. Above all, this implies that it must faithfully realize a class of model Hamiltonians with controllable parameters. Both for stationary and dynamical simulations the parameters must be tunable during the simulation to start, stop, and modify the evolution. In contrast to the necessary tunability, controllable interactions of the quantum simulator with its environment are required. Furthermore, one must be able to initialize the simulation and perform a measurement of its outcome.

An even more challenging task is that of building a *quantum computer*, i.e., a universal computer based on the laws of quantum mechanics. The interest in processing information by the means of quantum mechanics arose in 1985, when Deutsch, driven by central questions of information theory, tried to define a computational device, capable of efficiently simulating an arbitrary physical system [Deu85]. This lead him directly to a model of computation, exploiting the theory of quantum mechanics. Subsequently, algorithms have been found for efficiently solving certain problems, that are believed not be efficiently tractable on classical computers, like finding the prime factors of an integer [Sho94] or searching through an unstructured database [Gro95]. Now several proof-of-principle experiments have demonstrated the principle feasibility of scalable quantum computation [ZBB$^+$05].

The circuit-based model is the most common description of quantum computation: a sequence of elementary unitary gates connects the qubits, the elementary memory units. By reproducing the evolution of model Hamiltonians with these elementary gates on appropriately interpreted

qubits, the universal quantum computer can serve as a *digital quantum simulator*. However, universal quantum computers sufficiently large to exceed the power of modern classical computers have still to be developed. Fortunately, for certain models the realization of *analog quantum simulators* can be much less demanding. In this case the simulating system is tuned such that it directly represents the model Hamiltonian. It requires less local control and gets by without the overhead for quantum error correction. In the long run a digital quantum simulator would certainly be more versatile, in the short run analog quantum simulators can generate useful insights and promote the experimental progress towards a universal quantum computer.

An extensive list of proposal for and implementations of analog quantum simulators including their physical principle and the simulated model, can be found in [BN09]. The simulated models range from condensed matter theory to relativistic field theories. A lot of activity is aiming at challenging open questions in condensed matter physics, e.g., strongly-interacting systems, phase transitions, or high-temperature superconductivity. Such systems are relatively straightforward to simulate with arrays of qubits, e.g., with atoms in optical lattices, arrays of trapped ions, atoms in cavity arrays, quantum dots, or arrays of Josephson junctions [BN09]. In this thesis we address the full spectrum of analog quantum simulations from disorder in condensed matter physics to black holes in astrophysics. We will proceed with an introduction to quantum simulations in optical lattices and ion chains, the systems studied in this thesis.

An *optical lattice* is made up of standing electromagnetic waves created by counter-propagating laser beams [BDZ08, LSA+07]. The frequency of these lasers is adjusted to an optical transition within a species of neutral atoms. If the laser frequency is far detuned from this transition, the atoms will remain in their ground state, but feel an effective periodic potential. Naturally, only sufficiently cold atoms feel a noticeable lattice potential. In modern experiments atoms are first cooled with the help of Bose-Einstein condensates and subsequently loaded into the lowest band of an optical lattice [GME02]. Atoms in this band are described by Hubbard models [JBC+98], i.e., versions of the celebrated Fermi-Hubbard model describing correlated electrons in solids and possibly high-temperature superconductivity.

The Bose-Hubbard model, for example, contains a quantum phase transition between an insulating and a superfluid phase: In lattices with suppressed hopping of bosons between neighboring sites, each boson is lo-

calized on a single site and the bosons tend to occupy different sites (Mott insulator). In lattices with huge hopping strengths each boson is spread over the whole lattice and all bosons are occupying the same state (superfluid). The transition between these phases was probed in a pioneering quantum simulation experiment [GME02]. Here the lattice depth, i.e., the ratio between hopping and interaction strength, was tuned through the intensity of the laser beams. An alternative method of tuning the interaction strength is offered by Feshbach resonances [CGJ+10]. The momentum distribution of particles in optical lattices is routinely probed through time-of-flight imaging. Recently, two research groups succeeded in demonstrating microscope imaging and control with single-site resolution [SWE+10, BGP+09] paving the way for new and exciting quantum simulations. In the last decade optical lattices have attracted a huge interest from the theoretical as well as the experimental side [LSA+07], especially addressing condensed-matter phenomena for bosons, fermions, anyons, or their mixtures. With this thesis we contribute to the field of disordered optical lattices in chapter 2.

The confinement of cold *atomic ions* in an electrodynamic trap provides another system suitable for quantum simulations [WMI+98]. In contrast to optical lattices, the control and manipulation of single trapped ions is relatively simple, whereas the realization of scalable interacting systems is a challenging task. Early experiments with trapped ions motivated by the quest for accurate frequency standards were performed on single ions, where the occupation of two internal states was manipulated with electrodynamic radiation. These internal states can represent quasi-spins or qubits, but their natural interactions are typically negligible. Thus, the proposal by Cirac and Zoller for using phononic modes to mediate interactions between the quasi-spins was a milestone towards scalable quantum computation and quantum simulations with ions [CZ95]. To summarize, each ion typically represent one spin/qubit, easily addressable with lasers; interactions between these spins/qubits are mediated by the collective motional degrees of freedoms of the ions.

Following the invention of the Cirac-Zoller gate, universal quantum computation with chains of cold ions has attracted a lot of interest for offering great local control and very long coherence times. These properties make cold ions an ideal candidate for the quantum simulation of spin chains [PC04] as recently demonstrated experimentally [FSG+08]. Quantum spin models can tackle unsolved issues of condensed matter theory related to quantum magnetism, quantum phase transitions, or frustra-

tion. In chapter 3 we study the dynamics of spin systems in contact with a memoryless bath which can be simulated with chains of trapped ions. In chapter 4 we propose to use ion rings to simulate astrophysical black holes.

We will now proceed with an *overview* over the proposals for quantum simulations presented in this thesis [HCR07, HDR10, HC11, HRF$^+$10, HSR$^+$11], introducing their main ideas and motivating them in the context of current research. Note that we give more detailed introductions at the beginning of each chapter.

First, we propose the realization of disordered potentials in optical lattices with two species of particles in chapter 2 [HCR07, HDR10]. *Disorder* can trigger insulating behavior in metals stemming from *Anderson localization* of electronic matter waves [And58], i.e., wavefunctions with exponentially localized tails. While disorder can induce localization of classical particles, Anderson localization of quantum particles is possible even when their energy exceeds the energy scale of the disorder due to an interference effect, the coherent backscattering of matter waves. Though Anderson localization is a single-particle effect, in interacting many-particle systems it brings into force a variety of interesting phases. In recent years a huge theoretical and experimental effort has been aiming at the observation of Anderson localization for bosons with ultracold atoms culminating in two successful experiments using speckle potentials and incommensurate lattices to generate a disorder potential [BJZ$^+$08, RDF$^+$08].

An alternative approach for creating the disorder potential is the pinning of a secondary (frozen) species of atoms [GC05], where we consider two hyperfine states of the atoms. This allows to explore different statistics of the disorder potential by adjusting the state of the frozen species. We can even consider the frozen species to generate a superposition of random configurations such that the mobile atoms sample all realizations of the disorder potential in one measurement [PVC05]. We investigate two preparation schemes: First, we discuss the dynamics of two independently prepared species of hardcore bosons in one dimension after the sudden on-turn of the inter-species interactions [HCR07]. These hardcore bosons are effectively non-interacting as they are equivalent to non-interacting fermions. Alternatively, we propose to dynamically dope frozen bosons into a gas of weakly interacting mobile bosons in two dimensions via a Rabi pulse [HDR10]. In both schemes we observe dynamical localization with exponentially localized wavefunctions and the reduction of coherence. The case of weakly-interacting bosons further allows to numerically explore the

counterintuitive role of intra-species interactions in the dynamical-doping scheme.

Second, we propose the quantum simulation of spin chains in contact with a Markovian, i.e., memoryless, bath in chapter 3 [HC11]. This simulation can be realized in a chain of trapped ions. In the field of quantum computation and quantum simulation *decoherence* due to the interaction with an environment is traditionally regarded as a source of difficulty. Recently, however, it has been proposed to engineer the interaction with a bath to prepare interesting quantum states as the steady state of a decoherent evolution [VWC09, KBD$^+$08]. In a recent experiment the naturally present two-body interactions have been exploited for the quantum simulation of a Tonks-Girardeau gas [SBL$^+$08]. In this thesis we try to detect properties of the system in the decoherence dynamics, especially in the asymptotic decoherence rate.

We restrict ourselves to Markovian environments described by a Lindblad master equation. For our analysis, we develop a framework that allows for its exact solution for quadratic fermionic Hamiltonians and quadratic Hermitian Lindblad operators. This framework can also be applied to certain spin chains, e.g., the anisotropic XY chain in a transverse magnetic field, which correspond to such fermionic models via the Jordan-Wigner transformation. We find a *dissipative phase transition* in the asymptotic decoherence rate, i.e., the decoherence rate after a long evolution, reflecting a phase transition in the system and can relate this rate to ground state properties.

Third, we propose the realization of acoustic black holes on ion rings in chapter 4 [HRF$^+$10, HSR$^+$11]. The existence of *black holes* is predicted by the classical theory of general relativity at points of huge mass densities. No particle, not even massless ones, should be able to leave such a black hole. Surprisingly, using concepts of quantum theory Hawking could show in 1974 that black holes emit thermal radiation [Haw74]. *Hawking radiation* can be intuitively understood as the spontaneous pair creation of particles close to the black hole horizon, i.e., its border. Some pairs are subsequently separated by the horizon and cannot recombine. Unfortunately, the temperature of Hawking radiation from astrophysical black holes is very small and the original theoretical derivation relies on modes with infinite frequencies.

These issues can be addressed with acoustic black holes: Analogous hydrodynamical systems with a transition from subsonic to supersonic flow emit Hawking radiation [Unr81]. In such systems the Hawking effect

can be observed experimentally and its robustness against changes in the microphysics, i.e., the behavior at large frequencies, can be examined. Let us now illustrate the idea of analogous black holes. A one-dimensional hydrodynamical system contains two modes of excitations that travel into opposite directions with the same sound velocity $\pm c$. If the the fluid is moving with velocity v, the excitation velocity in the lab frame becomes $v \pm c$. Thus, in regions of supersonic flow with $v > |c|$ both modes are dragged along with the fluid ($v \pm c > 0$) and an analog black hole appears. In recent years many experimental realizations of this idea have been proposed and some have been implemented [BLV05]. Nevertheless, quantum Hawking radiation, i.e., spontaneously emitted radiation induced by quantum fluctuations, has not been definitely observed in experiments, yet.

In this thesis we are proposing the observation of the quantum Hawking effect with ions trapped on a ring. Here the rotation of the ions with an inhomogeneous, but stationary velocity profile constitutes the hydrodynamic flow, and the longitudinal oscillations of the ions, i.e., the phonons, constitute the excitations and the emitted Hawking radiation. A special ingredient of our proposal is its discreteness. The dispersion relation is, additionally, non-trivial at low wavenumbers because of the long-range Coulomb force. Nevertheless, we still obtain quantum Hawking radiation; the emitted radiation has a thermal spectrum, comes in pairs, and generates entanglement between the inside and the outside of the black hole.

After this introduction, we will present the details of our proposals for the quantum simulation of disordered lattice systems (see chapter 2), open spin systems (see chapter 3), and black holes (see chapter 4).

Chapter 2

Anderson Localization

2.1 Introduction

The control and manipulation of ultracold atoms in magnetic and optical traps has made enormous progresses towards the quantum simulation of fundamental condensed matter phenomena [JBC+98, GME02, BDZ08, LSA+07]. On the one hand, known fundamental models for the physics of solid state systems can be literally implemented in optical lattices [JZ04, JVD+03]. On the other hand, they offer the further advantage of controlling the Hamiltonian parameters in real time, and this enriches the range of correlated phases that can be implemented, if one can guide the evolution of the system towards an off-equilibrium state which is not necessarily an eigenstate of a known Hamiltonian.

In this chapter we are studying the phenomenon of quantum localization of matter waves induced by a random potential, observed in a variety of condensed-matter setups [KM93]. The fundamental model describing this rich phenomenology in presence of a lattice is the Bose-Hubbard model in a random potential [FWG+89], where, beside the conventional Mott insulating and superfluid phases, a Bose-glass phase appears, either associated with the fragmentation of weakly repulsive bosons into exponentially localized states, or with the localization of collective gapless modes for strong repulsion.

In fact, the capability of fine tuning the disorder potential as well as the interaction among atoms within the same sample leads to the possibility of investigating the Anderson localization transition with unprecedented control, and to monitor the complex effect of interparticle inter-

actions [SPL10, FFI08]. In 2008 substantial progress has been made in this direction with optical disorder potentials, leading to the observation of Anderson localization for weakly interacting bosons [BJZ+08, RDF+08, DZR+10] and to experiments aiming at the realization of a strongly interacting Anderson insulator (Bose glass) with bosons in optical lattices [FLG+06, WPM+09, PMW+10].

However, the task of realizing Anderson localization in ultracold atoms started a few years earlier with several experimental attempts [LFM+05, CVH+05, FFG+05, SDK+05, SDK+06, FLG+06] and theoretical proposals/discussions [DZS+03, RB03a, RB03b, SCL+07, KMD+05, CVR+06, LCB+07, San06, GWS+05, SRH07, SKS+04]. The disorder potential is realized optically, either through laser speckles [BJZ+08, LFM+05, CVH+05, FFG+05, SDK+05] in presence or absence of an optical lattice, or, in optical lattices, through a secondary incommensurate standing wave [RDF+08, FLG+06]. In the former case, the typical length scale associated with the disorder potential was quite extended with respect to the correlation length of the bosons in the early experiments, so that classical trapping rather than quantum localization was responsible for the observed suppression of transport properties [SDK+06]. In the latter case, an incommensurate superlattice [RDF+08, FLG+06] realizes a potential which is strongly fluctuating over the distance of a few lattice sites, but its *pseudo*-disordered nature requires to take also into account gapped insulating phases at incommensurate fillings, competing with the Bose glass [RSC06].

An alternative route to Anderson localization of cold atoms is that of creating a disorder potential by pinning a random distribution of a frozen atomic species. A second atomic species is mobile and experiences a disorder potential due to interspecies collisions. This localizes the mobile species [GC05, PVC05, RC07, HCR07, HDR10]. Its huge advantage is that the correlations in the disorder potential are given by the correlations within the frozen species, and are thus naturally of the order of the lattice spacing.

In this chapter we are discussing refinements of this proposal, where the two species correspond to two different hyperfine states of the atoms. This approach has the unique advantage that the disorder potential can be prepared in a quantum superposition of different realizations, such that the time evolution of the mobile atoms samples all realizations of the potential at once, and measurements on the mobile particles deliver disorder-averaged observables [PVC05, HCR07, HDR10].

One strategy to achieve this is the independent preparation of the

Figure 2.1: Sketch of the Bose-Hubbard model (see Eq. (2.1)). Bosons can hop to the nearest-neighbor site with amplitude J, bosons on the same site feel an interaction with strength U.

mobile and frozen atoms, and subsequent switching of their mutual interaction [HCR07], which can be realized by controlling the spatial phase of different polarization components of the lattice [JBC+99, BCJ+99, MGW+03] (see Sec. 2.3). This analysis has the advantage of a great flexibility in the generated disorder potential, but the independent preparation and control of two species is experimentally demanding. Another strategy is the preparation of a single mobile species, and subsequent transfer of some atoms into a frozen hyperfine state, i.e., the "dynamical doping" of frozen atoms into a cloud of mobile atoms. (see Sec. 2.4), which can be less demanding to achieve in experiments. In the former case we are treating effectively non-interacting hardcore bosons in one dimensions (see Sec. 2.3), in the latter case weakly interacting bosons in two dimensions (see Sec. 2.4). After the presentation of the two schemes we discuss their experimental realization in Sec. 2.5 before summarizing our findings in Sec. 2.6.

2.2 System and Method

An interesting proposal for the implementation of quantum simulation is that of using optical lattices. An optical lattice is made up of standing electromagnetic waves that can easily be created by two counter propagating laser beams. The frequency of these standing waves is adjusted to the transition between the ground state and an excited internal state of some neutral atoms, e.g. Rubidium ^{87}Rb. If the laser frequency is far detuned from this transition, the atoms will always remain in their ground state, but an effective periodic potential is created [JZ04].

It has been shown in [JBC+98] that the atoms in this lattice can be

described by the Bose-Hubbard model (see Fig. 2.1).

$$\mathcal{H}_{\mathrm{BH}} = -J \sum_{\langle ij \rangle} \left(a_i^\dagger a_j + \mathrm{H.c.} \right) + \frac{U}{2} \sum_i \left[n_i \big(n_i - 1 \big) \right], \tag{2.1}$$

which allows tunneling to nearest-neighbor sites with hopping amplitude J and includes an on-site interaction with strength U. In this chapter we propose to introduce a disorder potential in an optical lattice via a frozen secondary species of light. The full system of two trapped interacting bosonic species in an optical lattice is described by the Hamiltonian

$$\mathcal{H} = \mathcal{H}_0 + \mathcal{H}_{\mathrm{f}} + \mathcal{H}_{\mathrm{int}}, \tag{2.2}$$

where $\mathcal{H}_0$ is the Hamiltonian of the bosons which will remain mobile,

$$\begin{aligned} \mathcal{H}_0 = \; & - \; J \sum_{\langle ij \rangle} \left(a_i^\dagger a_j + \mathrm{H.c.} \right) \\ & + \; \sum_i \left[\frac{U}{2} n_i \big(n_i - 1 \big) + V \big(i - i_0 \big)^2 n_i \right], \end{aligned} \tag{2.3}$$

$\mathcal{H}_{\mathrm{f}}$ is the Hamiltonian for the bosons to be frozen,

$$\begin{aligned} \mathcal{H}_{\mathrm{f}} = \; & - \; J^{\mathrm{f}} \sum_{\langle ij \rangle} \left(a_i^{\mathrm{f}\dagger} a_j^{\mathrm{f}} + \mathrm{H.c.} \right) \\ & + \; \sum_i \left[\frac{U^{\mathrm{f}}}{2} n_i^{\mathrm{f}} \big(n_i^{\mathrm{f}} - 1 \big) + V^{\mathrm{f}} \big(i - i_0 \big)^2 n_i^{\mathrm{f}} \right], \end{aligned} \tag{2.4}$$

and $\mathcal{H}_{\mathrm{int}}$ is the interaction Hamiltonian

$$\mathcal{H}_{\mathrm{int}} = W \sum_i n_i n_i^{\mathrm{f}}. \tag{2.5}$$

Here $a_i^\dagger$ and a_i are boson creation and annihilation operators and $n_i = a_i^\dagger a_i$ is the number operator for site i. Symbols with the superscript f are the corresponding operators for the frozen bosons that create the disorder potential. In Eqs. (2.3), (2.4) we also consider an external harmonic trap, where $V = \frac{m}{2}\omega^2 d^2$ and $V^{\mathrm{f}} = \frac{m}{2}\omega^{\mathrm{f}2} d^2$ determine the size of an overall harmonic trap of frequency $\omega/2\pi$. Here m is the atomic mass and d the lattice spacing. We consider repulsive interactions $W > 0$.

2.3 Independent Preparation

We are now discussing a specific proposal for the realization of disorder with two species of particles, where a frozen species creates a disorder potential for a mobile species [HCR07, Hor07]. After the independent preparation of two species of particles in two different hyperfine states, the two species are brought into interaction (see Fig. 2.2). Subsequently the mobile one evolves in a quantum superposition of all possible realizations of the random potential associated with the Fock components of the state of the frozen species $|\Phi^{\mathrm{f}}\rangle$, and expectation values over the evolved state are therefore automatically averaged over the disorder distribution [PVC05]. In this proposal not only is the disorder potential strongly fluctuating over the length scale of a few lattice sites, but in principle one can also vary its statistics by preparing the frozen bosons in different states $|\Phi^{\mathrm{f}}\rangle$.

In this section we investigate the above proposal in detail in the exactly solvable case of a one-dimensional gas of hardcore bosons on a lattice [LSM61, PWM$^+$04]. We consider both species of bosons (the mobile one and the frozen one) to be hardcore repulsive, which is not only experimentally feasible [PWM$^+$04, KWW04], but it has three fundamental theoretical advantages:

1. The state $|\Phi^{\mathrm{f}}\rangle$ of the frozen bosons can be obtained exactly from the Hamiltonian of the system before freezing, and disorder averaging can therefore be accurately performed.

2. Jordan-Wigner diagonalization [LSM61] allows to calculate the exact real-time evolution of the mobile particles [RM04a, RM05a, RM04b, RM05b] after they are brought into interaction with the frozen ones.

3. Most importantly from a conceptual point of view, localization phenomena of hardcore bosons are perfectly understood in terms of Anderson localization of non-interacting fermions.

While the observation of localization for interacting bosons is limited by screening of the disorder potential and the reduction of the healing length due to the interaction, many-body effects enter the system of non-interacting fermions only through Fermi statistics.

In particular we focus on the case in which the frozen bosons are initially prepared in the superfluid ground state $|\Phi^{\mathrm{f}}\rangle$ of the hardcore boson Hamiltonian at *half* filling with periodic boundary conditions. The resulting disorder potential has the structure of a bimodal random on-site

energy, with algebraically decaying correlations, but also with a very rich Fourier spectrum dominated by short-wavelength components. Most importantly, such a potential is found to lead to Anderson localization of all single-particle eigenstates (apart from possibly a set of zero measure) as expected for uncorrelated disorder [Ish72, Tho74, AAL$^+$79]. The evolution of the mobile bosons in such a potential is found to invariably lead to a localized steady state with exponentially decaying correlations and absence of quasi-condensation for a wide variety of realistic initial conditions. In particular phenomena of quasi-condensation in finite-momentum states [RM04b] and fermionization [RM05b], reported upon expansion of the hardcore bosons from a Mott-insulating state and a superfluid state respectively, are completely washed out by the disorder potential. Hence we can conclude that this setup allows for a robust implementation of a localized state as the off-equilibrium steady state of the system evolution.

This section is structured as follows: Sec. 2.3.1 describes the system of two bosonic species, the exact diagonalization method for the study of real-time evolution, the Monte Carlo sampling of the disorder distribution, and the main features of the random potential. Sec. 2.3.2 is devoted to the study of localization of the single-particle eigenstates in the random potential. Sec. 2.3.3 investigates the evolution of the mobile bosons after interaction with the frozen ones when both species are prepared on a ring. Finally, Sec. 2.3.4 is dedicated to the study of the expansion of the mobile bosons in the random potential, starting from different initial confined states.

2.3.1 System and Method

In this section we present the system of two hardcore bosonic species which is used to study the effect of a disorder potential. We then briefly describe the numerical procedure to exactly treat the equilibrium and out-of-equilibrium properties of the system, and the sampling of the disorder distribution. Finally, we examine the nature of the correlations in the disorder potential created by a frozen species of hardcore bosons.

Hamiltonian Dynamics

We have presented the full Hamiltonian for two interacting bosonic species trapped in an optical lattice in Sec. 2.2. In this section we consider one-dimensional optical lattices with L sites and the possibility of both species

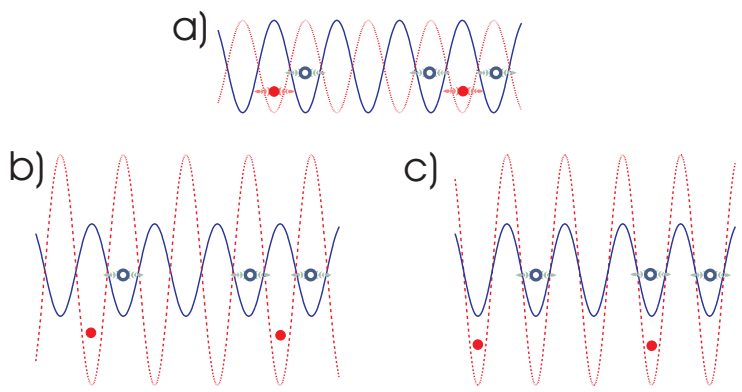

Figure 2.2: Sketch of the preparation of the disorder potential and of the tuning of its strength using state-dependent optical lattices for a mixture of atoms in two internal states. The two species are first prepared in two shifted optical lattices *(a)*, then one of the two optical lattice is increased in strength so as to freeze one of the two bosonic species *(b)*, and finally the spatial phase of the two lattices is changed to bring the two species into interaction *(c)*.

being confined by a parabolic trap with different trapping strengths V, V^{f} for the two species.

At times $t < 0$ the two species of bosons are not interacting with each other ($W = 0$), and they are prepared in the factorized ground state $\left|\Psi\right\rangle_{t=0} = \left|\Phi^{\mathrm{f}}\right\rangle \otimes \left|\Phi\right\rangle_0$ of their respective Hamiltonian with fixed numbers of particles N and N^{f}. The ground state $\left|\Phi^{\mathrm{f}}\right\rangle$ of the frozen particles can be decomposed in the Fock basis

$$\left|\Phi^{\mathrm{f}}\right\rangle = \sum_{\{n_i^{\mathrm{f}}\}} c\left(\{n_i^{\mathrm{f}}\}\right) \left|\{n_i^{\mathrm{f}}\}\right\rangle, \tag{2.6}$$

where the sum extends over all Fock states,

$$\{n_i^{\mathrm{f}}\} = \left(n_1^{\mathrm{f}}, n_2^{\mathrm{f}}, \ldots, n_L^{\mathrm{f}} : \sum_{i=1}^{L} n_i^{\mathrm{f}} = N^{\mathrm{f}}\right). \tag{2.7}$$

At some time $t \leq 0$ the frozen bosons are made immobile ($J^{\mathrm{f}} = 0$), and subsequently at $t = 0$ the interaction between the two species is turned on ($W > 0$). Furthermore, releasing the mobile bosons from their trap ($V = 0$) allows us to study their expansion properties.

The time evolution of the initially prepared state for $t > 0$ is described by

$$\big|\Psi\rangle_t = e^{-i\mathcal{H}t/\hbar} \sum_{\{n_i^{\rm f}\}} c\left(\{n_i^{\rm f}\}\right) \big|\{n_i^{\rm f}\}\rangle \otimes \big|\Phi\rangle_0 \tag{2.8}$$

$$= \sum_{\{n_i^{\rm f}\}} c\left(\{n_i^{\rm f}\}, t\right) \big|\{n_i^{\rm f}\}\rangle \otimes \big|\Phi\left(\{n_i^{\rm f}\}\right)\rangle_0, \tag{2.9}$$

where the coefficients

$$c(\{n_i^{\rm f}\}, t) = \exp\left[-i\phi\left(\{n_i^{\rm f}\}\right) t\right] \; c\left(\{n_i^{\rm f}\}\right) \tag{2.10}$$

have acquired a phase factor which will become irrelevant, and the state

$$\big|\Phi\left(\{n_i^{\rm f}\}\right)\rangle_t = \exp\left\{-i\left[\mathcal{H}_0 + \mathcal{H}_{int}\left(\{n_i^{\rm f}\}\right)\right] t/\hbar\right\} \big|\Phi\rangle_0 \tag{2.11}$$

represents the time evolution of the initial state of the mobile bosons interacting with a single Fock state $\big|\{n_i^{\rm f}\}\rangle$ of the frozen bosons, which determines the static external potential. We have used the property that, for $J^{\rm f} = 0$, $[\mathcal{H}_{\rm f}, \mathcal{H}_0 + \mathcal{H}_{\rm int}] = 0$.

Hence, equation (2.8) describes the parallel time evolution of the mobile bosons in a *quantum superposition* of different realizations of the disorder potential $V_i = V n_i^{\rm f}$, each appearing with a probability

$$P\left(\{n_i^{\rm f}\}\right) = |c\left(\{n_i^{\rm f}\}\right)|^2. \tag{2.12}$$

Remarkably, the time evolution of the expectation value of an operator A acting only on the mobile bosons is automatically averaged over the disorder statistics [PVC05]:

$${}_t\langle\Psi\big|A\big|\Psi\rangle_t = \sum_{\{n_i^{\rm f}\}} \left|c\left(\{n_i^{\rm f}\}\right)\right|^2 \; {}_t\langle\Phi\left(\{n_i^{\rm f}\}\right)\big|A\big|\Phi\left(\{n_i^{\rm f}\}\right)\rangle_t. \tag{2.13}$$

Hardcore limit and Jordan-Wigner Transformation

From here onwards we will restrict ourselves to the exactly solvable case of *hardcore* bosons, obtained in the limit $U, U^{\rm f} \to \infty$ for filling smaller than or equal to one. It is convenient to incorporate the hardcore constraint directly in the operator algebra, passing to hardcore boson operators which *anti*commute on the same site, $\{a_i, a_i^\dagger\} = 1$, $\{a_i^{(\dagger)}, a_i^{(\dagger)}\} = 0$,

and $\{a_i^{\mathrm{f}}, a_i^{\mathrm{f}\dagger}\} = 1$, $\{a_i^{\mathrm{f}(\dagger)}, a_i^{\mathrm{f}(\dagger)}\} = 0$. The hardcore boson operators for different sites $i \neq j$ commute like normal bosons, $[a_i, a_j^\dagger] = [a_i^{(\dagger)}, a_j^{(\dagger)}] = 0$, and $[a_i^{\mathrm{f}}, a_j^{\mathrm{f}\dagger}] = [a_i^{\mathrm{f}(\dagger)}, a_j^{\mathrm{f}(\dagger)}] = 0$.

Making use of the Jordan-Wigner transformation [LSM61],

$$a_i^\dagger = f_i^\dagger \prod_{k=1}^{i-1} e^{-i\pi f_k^\dagger f_k}, \quad a_i = \prod_{k=1}^{i-1} e^{i\pi f_k^\dagger f_k} f_i, \tag{2.14}$$

one can map the hardcore boson operators onto spinless fermion operators $f_i^\dagger$ and f_i, obeying the same Hamiltonian as the bosonic one, apart from a boundary term depending on the number of particles in the case of periodic/antiperiodic boundary conditions. The fermionic problem is exactly solvable, and its eigenstates can be written in the following form

$$\big|\Phi\rangle = \prod_{m=1}^{N} \sum_{n=1}^{L} P_{nm} f_n^\dagger |0\rangle, \tag{2.15}$$

where the N columns of the matrix $P_{nm} = \{\mathbf{P}\}_{nm}$ represent the first N single-particle eigenstates. Following the recipe given in [RM04a, RM05a], from the matrix P_{nm} one can efficiently calculate the one-particle density matrix (OPDM)

$$\rho_{ij} = \langle a_i^\dagger a_j \rangle, \tag{2.16}$$

and hence the momentum distribution

$$\langle n_k \rangle = \frac{1}{L} \sum_{m,n=1}^{L} e^{-ik(m-n)} \langle a_m^\dagger a_n \rangle, \tag{2.17}$$

which represents a fundamental observable in trapped atomic systems. At a more fundamental level, the knowledge of the eigenvalues λ_η of the OPDM, associated to eigenvectors ϕ_i^η also known as natural orbitals (NO), allows one to rigorously study condensation phenomena through the scaling of the maximum eigenvalue λ_0 with the particle number [PO56, RM04a, RM05a]. In absence of an external potential the OPDM of the hardcore bosons decays algebraically as $\rho_{ij} \sim |i-j|^{-\alpha}$, where $\alpha = 0.5$, signaling off-diagonal quasi-long-range order in the system [KIB93]. Correspondingly the occupation of the $k = 0$ momentum state, which coincides with the natural orbital with largest eigenvalue for a translationally invariant system, scales as $n_{k=0} \sim \sqrt{N}$ with the particle number N for

any fixed density $n = N/L < 1$, namely it exhibits *quasi-condensation*. Remarkably, quasi-long-range order and quasi-condensation (in the form of a $\sqrt{N}$ scaling of the largest eigenvalue λ_0 of the OPDM) survive also in presence of a trapping potential $V\big(i - i_0\big)^a$ when the particle number is increased and correspondingly the trap strength V is decreased so that the characteristic density in the trap

$$\tilde{\rho} = N \left(\frac{V}{J}\right)^{1/a}, \tag{2.18}$$

is kept constant and smaller than a critical value ρ_c (≈ 2.6 for $a = 2$) to avoid formation of a Mott plateau in the trap center [RM04a, RM05a].

Finally, the exact solution of the fermionic Hamiltonian allows one to calculate the real-time evolution of the fermionic wavefunction, and in particular of the P matrix as

$$\mathbf{P}\,(t) = e^{-i\mathbf{H}t}\mathbf{P} \tag{2.19}$$

with the single-particle time evolution operator given by

$$\left(e^{-i\mathbf{H}t}\right)_{ij} = \langle 0 \big| f_i e^{-i\mathcal{H}t/\hbar} f_j^\dagger \big| 0 \rangle. \tag{2.20}$$

Making use of this approach, Refs. [RM04b, RM05b] have shown that quasi-condensation is a robust feature of the system after expansion starting from an initially trapped quasi-condensed state, and it is even dynamically recovered when the initial state before expansion is a fully incoherent Mott insulator state.

Disorder Averaging

Eq. (2.37) shows that, ideally, the unitary evolution of the system explores all possible realizations of the disordered potential at once. Numerical calculations based on a matrix-product-state representation of the system state also enjoy this feature of "quantum parallelism" of the Hamiltonian evolution [PVC05] by treating the disorder potential as a quantum variable in the system. In this chapter we use the more traditional approach of exactly calculating the ground-state properties and the Hamiltonian evolution of hardcore bosons for a single realization of disorder at a time, averaging then over the disorder distribution through Monte Carlo importance sampling. Accepting the overhead of disorder averaging, this approach has the advantage that, unlike the method proposed in [PVC05], the time evolution is exact for arbitrarily long times.

According to Eq. (2.13), the weights of the disorder configurations are defined by the coefficients of the Fock-state decomposition for the initial state of the frozen bosons through Eq. (2.12). Introducing the bosonic Fock state

$$\left|\left\{n_i^{\mathrm{f}}\right\}\right\rangle = a_{i_1}^\dagger a_{i_2}^\dagger \dots a_{i_{N^{\mathrm{f}}}}^\dagger \left|0\right\rangle \tag{2.21}$$

and the $N^{\mathrm{f}} \times L$ matrix $Q_{nm} = \{\mathbf{Q}\}_{nm} = \delta_{i_n,m}$, after some algebra we get

$$c\left(\left\{n_i^{\mathrm{f}}\right\}\right) = \left\langle\left\{n_i^{\mathrm{f}}\right\}|\Phi_{\mathrm{f}}\right\rangle = \det\left(\mathbf{Q}^\dagger\mathbf{P}\right). \tag{2.22}$$

The energy eigenstates of noninteracting fermions with periodic boundary conditions, contained in the columns of the $\mathbf{P}$ matrix, are given by plain waves. Thus it can be shown that the Slater determinant of Eq. (2.22) is a Vandermonde determinant, which can be evaluated analytically. The disorder weights finally become

$$\left|c\left(\left\{n_i^{\mathrm{f}}\right\}\right)\right|^2 = \frac{1}{L^{N^{\mathrm{f}}}} \prod_{1\le n<m\le N^{\mathrm{f}}} \sin^2\left[\frac{\pi}{L}\left(i_n - i_m\right)\right]. \tag{2.23}$$

Throughout the section we will compare the effect of the disorder potential generated by the frozen superfluid state of N^{f} bosons with that of the potential generated by N^{f} *fully uncorrelated* frozen bosons (The uncorrelated frozen bosons are considered to be in the state $\left|\Phi^{\mathrm{f}}\right\rangle = \otimes_{i=1}^{L}(1+a_i^\dagger)\left|0\right\rangle$ projected on the subspace with a fixed number of particles. This state cannot straightforwardly be prepared in an optical lattice.), with the flat distribution

$$\left|c\left(\left\{n_i^{\mathrm{f}}\right\}\right)\right|^2 = (N^{\mathrm{f}}!(L-N^{\mathrm{f}})!)/L!. \tag{2.24}$$

Even when equipped with the exact statistics of disorder as in Eqs. (2.23) and (2.24), it is generally hopeless to fully average the results of any calculation on the $L!/(N^{\mathrm{f}}!(L-N^{\mathrm{f}})!)$ disorder configurations. Hence we opt for Monte Carlo importance sampling, where starting from an initially chosen random configuration $\left|\left\{n_i^{\mathrm{f}}\right\}\right\rangle$, we propose a new one $\left|\left\{n_i^{\mathrm{f}}\right\}'\right\rangle$, e.g. by swapping the occupation of two sites, and accept it with Metropolis probability

$$p = \min\left(\left|c(\left\{n_i^{\mathrm{f}}\right\}')\right|^2 / \left|c\left(\left\{n_i^{\mathrm{f}}\right\}\right)\right|^2, 1\right). \tag{2.25}$$

The real-space properties are typically averaged over 10^5 disorder realizations, obtained one from the other by updating $O(L)$ sites, while the OPDM is averaged over 10^2 realizations (due to the computational overhead of the OPDM calculation). This provides full convergence of the disorder-averaged quantities.

Characteristics of Disorder

A fundamental figure of merit for the proposed setup to introduce disorder in optical lattices is represented by the correlation properties of the disorder potential generated by the frozen particles. As discussed in the introduction, the aspect of correlations represents one of the main weaknesses of the optical implementation of disorder through laser speckles [SDK+06]. In particular, we focus on the density-density correlation function

$$C_r\left(\left|\Phi^f\right\rangle\right) = \frac{\frac{1}{L}\sum_{i=1}^{L}\left\langle\left(n_i^{\mathrm{f}}-n^{\mathrm{f}}\right)\left(n_{i+r}^{\mathrm{f}}-n^{\mathrm{f}}\right)\right\rangle}{\frac{1}{L}\sum_{i=1}^{L}\left\langle\left(n_i^{\mathrm{f}}-n^{\mathrm{f}}\right)^2\right\rangle}, \tag{2.26}$$

where $n^{\mathrm{f}} = \langle n_i^{\mathrm{f}}\rangle = N^{\mathrm{f}}/L$. This correlation function for the frozen hardcore bosons is identical to the one for the corresponding fermions, and can be calculated exactly in the homogeneous system ($V^{\mathrm{f}} = 0$) with periodic boundary conditions; for $N^{\mathrm{f}} < L$, namely in the superfluid state of hardcore bosons,

$$C_r\left(\left|\Phi^f\right\rangle\right) = \begin{cases} 1 & \text{for } r = 0 \\ -\left[N^{\mathrm{f}}\left(L-N^{\mathrm{f}}\right)\right]^{-1}\frac{\sin^2\left(\pi\frac{N^{\mathrm{f}}r}{L}\right)}{\sin^2\left(\pi\frac{r}{L}\right)} & \text{for } r \geq 1. \end{cases} \tag{2.27}$$

Hence, in the limit $r \ll L$ (which is always satisfied in the thermodynamic limit) the correlator decays algebraically like $C_r\left(\left|\Phi^f\right\rangle\right) \sim r^{-2}$ with a superimposed oscillation at twice the Fermi wavevector $k_{\mathrm{F}} = \pi n^{\mathrm{f}}$. The negative values of the correlator can be understood as resulting from an effective long-range repulsion between the hardcore bosons due to the kinetic energy, which enjoys as much free space around each boson as possible.

From Eq. (2.27) we deduce that the disorder potential created by the frozen bosons has slowly decaying correlations. Nonetheless it has fast oscillations on short distances, which are captured by the structure factor, namely the Fourier transform of the correlator:

$$C_k = \frac{1}{L}\sum_{r=0}^{L-1} C_r \cos\left(kr\right). \tag{2.28}$$

This function can be evaluated to give for $k \in [-\pi, \pi]$ and $n^{\mathrm{f}} \leq 0.5$

$$C_k = \begin{cases} \frac{1}{L\left(1-n^{\mathrm{f}}\right)}\cdot\frac{|k|}{2k_{\mathrm{F}}} & \text{for } |k| \leq 2k_{\mathrm{F}} \\ \frac{1}{L\left(1-n^{\mathrm{f}}\right)} & \text{for } 2k_{\mathrm{F}} \leq |k| \leq \pi. \end{cases} \tag{2.29}$$

The expression for $n^{\mathrm{f}} > 0.5$ follows from particle-hole symmetry. The corresponding functions for an uncorrelated random potential generated by randomly displayed frozen particles are $C_r = \delta_{r0}$ and $C_k = 1/L$. We observe that the Fourier spectrum of the frozen-boson potential is extremely broad, and it has a flat maximum for $k \geq k_{\mathrm{F}}$, reflecting the short wavelength oscillations of the potential. Hence we are in presence of a correlated but strongly fluctuating potential. In the following section we will see that such a potential generally leads to Anderson localization of all single-particle states and to the suppression of quasi-condensation at all fillings. Throughout the rest of the section, we will take the case of half-filling for the frozen bosons, $N^{\mathrm{f}} = L/2$.

2.3.2 Ground-State Localization

In this section we investigate the properties of the eigenstates of the Hamiltonian $\mathcal{H}_0 + \mathcal{H}_{int}$ (see equations (2.3) and (2.5)) for the mobile bosons moving in the potential created by the frozen bosons. Here we consider an homogeneous system ($V = V^{\mathrm{f}} = 0$) with periodic boundary conditions for both species of bosons. We start with an analysis of the localization properties in real space and continue with an analysis of coherence in momentum space.

We investigate the localization properties in the frozen-boson potential through the *participation ratio* (PR) defined as

$$\mathrm{PR}\left(\left|\Phi\right\rangle\right) = \frac{\left(\sum_{i=1}^{L}\langle n_i\rangle\right)^2}{\sum_{i=1}^{L}\langle n_i\rangle^2}, \tag{2.30}$$

where $\langle n_i\rangle$ is the average particle density on site i. In the case of a rectangular density profile the participation ratio gives the support of the density profile, for exponentially localized states it is proportional to the decay length of the wavefunction, and for a Gaussian-shaped density profile it is proportional to its standard deviation.

The average PR of single particle eigenstates in the potential created by a half-filled system of frozen bosons at $W = 0.5J$ is shown in Fig. 2.3a as a function of energy, for various system sizes. The PR essentially becomes size independent for $L \geq 1000$, clearly indicating the localization of all single-particle eigenstates, except for possibly a subset of zero measure; we find a similar result for all strengths of the potential we investigated. Still a non-extensive number of extended eigenstates, not captured by this

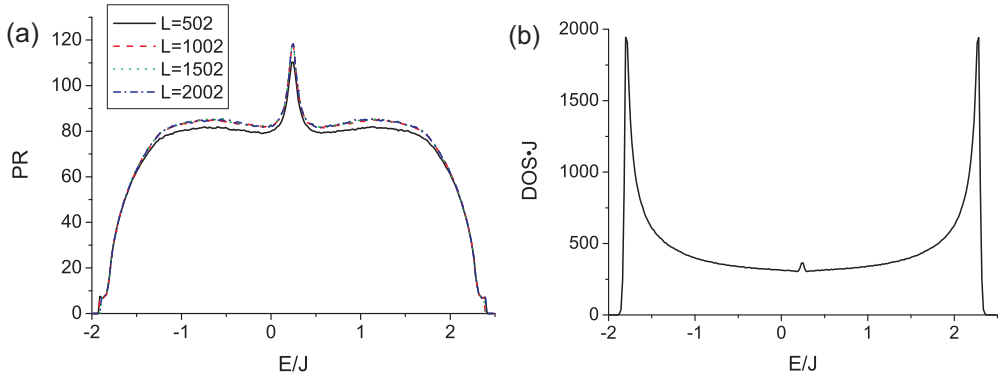

Figure 2.3: (a) Average participation ratio and (b) density of states (DOS) of the single-particle energy eigenstates in the correlated random potential created by frozen bosons with disorder strength $W = 0.5J$. The DOS is the disorder averaged number of eigenstates per energy interval; it is calculated for the system size $L = 2002$.

analysis, is in principle sufficient to suppress localization, e.g. in transport experiments [DWP90], so that further analysis is required to complete the picture on the localization properties of the frozen-boson potential (see Sec. 2.3.4). The peak in the PR at the center of the band can be understood by the following argument: Without disorder the single-particle eigenstates in the center of the band are plain waves with wavenumber $k = \pm\pi/2$. Thus, in the presence of a shallow disorder potential the corresponding states have dominant $k = \pm\pi/2$ components. As these are also the dominant Fourier components of the random potential for half filling, the eigenstates in the center of the bands are less localized.

We now move on to discuss the properties of the *many-body* ground state for hardcore bosons in the frozen-boson potential. Making contact with the discussion of Sec. 2.3.1, such a ground state can be reached by adiabatically turning on the interaction W between the two species after having prepared each of them separately and having quenched the hopping of the frozen bosons. In particular we analyze the properties of the disorder-averaged OPDM, which is translationally invariant, so that its eigenvalues correspond to the momentum distribution function (MDF), and hence average condensation properties are studied in momentum space through the scaling of $\lambda_0 = n_{k=0}$ with the number of particles N.

The scaling analysis of the disorder-averaged occupations of the lowest

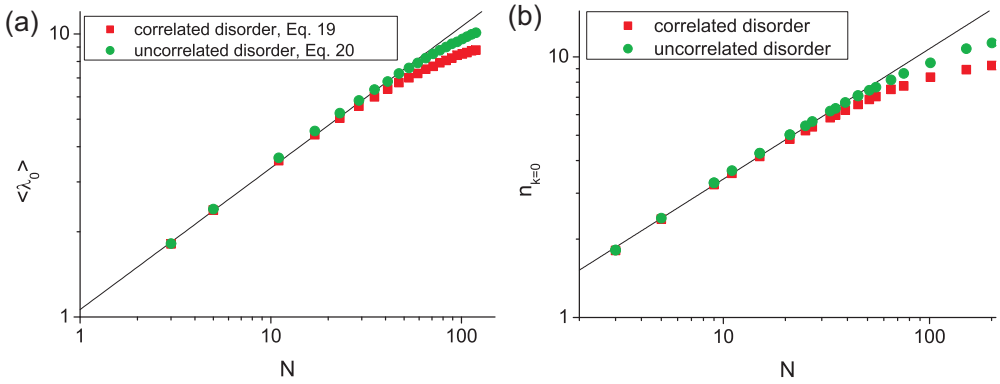

Figure 2.4: Scaling of the (a) disorder-averaged largest eigenvalue λ_0 of the OPDM and (b) the occupation of the zero momentum state $n_{k=0}$ for the ground state of a half-filled system of mobile bosons, interacting with the disorder potential. The cases of a correlated potential resulting from the superfluid state, Eq. (2.23), and that of a fully uncorrelated potential, Eq. (2.24), are compared. Here the strength of disorder is $W = 0.5J$. The black lines are fits to $n_{k=0}, \langle\lambda_0\rangle \propto \sqrt{N}$ for the first four data points.

natural orbitals λ_0 is shown in Fig. 2.4a where, as N grows, N^{f} and L are grown correspondingly such that $N = N^{\mathrm{f}} = L/2$. For small system sizes the hardcore bosons show quasi-condensation behaviour $\lambda_0 \sim N^{\alpha}$, with $\alpha = 0.5$ within the error given by the simulation, but for larger system sizes λ_0 saturates, hence revealing the absence of quasi-condensation in the thermodynamic limit. As shown in Fig. 2.4a, the same quantity for the potential generated by fully uncorrelated frozen particles gives a completely analogous picture. This crossover can be qualitatively explained as a fragmentation effect. The lowest natural orbital in each disorder configuration is localized, namely it does not scale with the system size and hence it can can only accommodate a finite number of particles, since the bosons repel each other.

As translational invariance is restored after disorder-averaging, the eigenvalues of the disorder-averaged OPDM correspond to the momentum distribution function. The peak at zero momentum, in which quasi-condensation appears in the case without disorder, is significantly reduced in presence of disorder. A scaling analysis of $n_{k=0}$ of the mobile bosons, shown in Fig. 2.4b detects a similar crossover from algebraic increase to saturation as for the disorder-averaged λ_0. Therefore, the con-

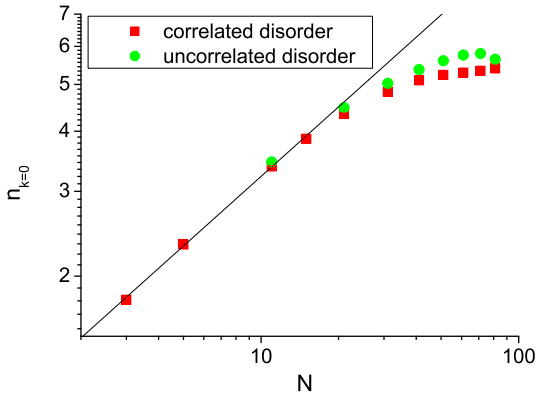

Figure 2.5: Scaling of the steady-state zero-momentum occupation $n_{k=0}$ with the particle number N in a homogeneous system of mobile and frozen bosons ($V = V^{\mathrm{f}} = 0$) at half-filling ($N = N^{\mathrm{f}} = L/2$), with interaction strength $W = 0.5J$. The line corresponds to a fit $n_{k=0} \sim \sqrt{N}$ to the first four data points.

sequences of fragmentation extends to this experimentally accessible observable, and we can conclude on the absence of quasi-condensation in the disorder-averaged OPDM of the ground state of the system. (Although the disorder-averaged largest eigenvalue $\langle \lambda_0 \rangle$ and the disorder-averaged $k = 0$ occupation $n_{k=0}$ show a similar scaling with system size, they have no simple relationship to each other; indeed λ_0 refers to localized natural orbitals, while $n_{k=0}$ is associated with an extended one.) Moreover, the density of states, shown in Fig. 2.3b, reveals a continuous excitation spectrum at all energies. Hence, for a system of interacting bosons, the absence of quasi-condensation, together with the absence of gaps in the density of states, leads to classify the state of the system as a Bose glass. At the same time the Jordan-Wigner transformation translates this phase into an ideal Anderson insulator of non-interacting fermions. Thus, remarkably, the gas of hardcore boson subjected to a disorder potential can be regarded as both a Bose glass and an Anderson glass.

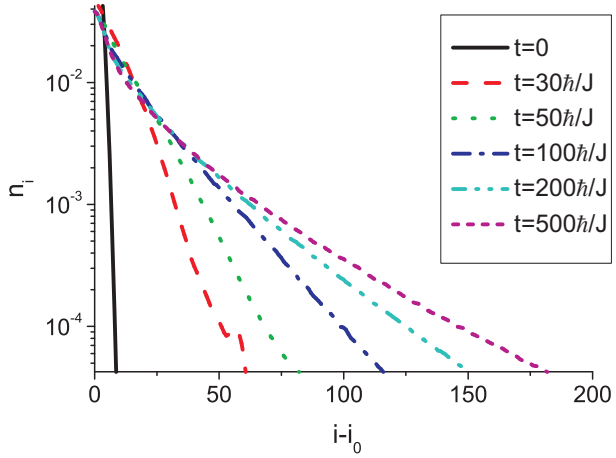

Figure 2.6: Snapshot of the evolution of the real-space density n_i for a single particle, initially in the ground state of a harmonic trap with $V = 0.01J$, and interacting with a correlated disorder potential. Here the interaction strength is $W = 0.5J$, and the system size is $L = 502$.

2.3.3 Dynamical Localization

While the previous section investigated the state of the mobile bosons after an adiabatic on-turn of the interaction with the disorder potential created by the frozen bosons, in this section we consider the evolution of the mobile bosons after turning on that interaction suddenly. We consider such a time evolution in the homogeneous system, i.e., $V = V^{\mathrm{f}} = 0$, with periodic boundary conditions, mimicking the situation in which both species of particles are prepared in the same region of space before being brought into interaction. In this situation, the disorder-averaged real-space density of the mobile bosons remains uniform during time evolution, so that real-space localization effects are not visible. Nonetheless, even in a more realistic experimental scenario, in which both species of particles are kept in the same nonvanishing trap ($V = V^{\mathrm{f}} > 0$), the disorder-averaged density profile of the mobile species does not reveal marked localization effects, and it is even expanding during time evolution in order to reduce the overlap with the confined frozen bosons [PVC05].

The fundamental effect of disorder on the time evolution can be very clearly detected in momentum space, which can be measured in time-of-flight experiments. The initial quasi-condensation peak in the MDF at

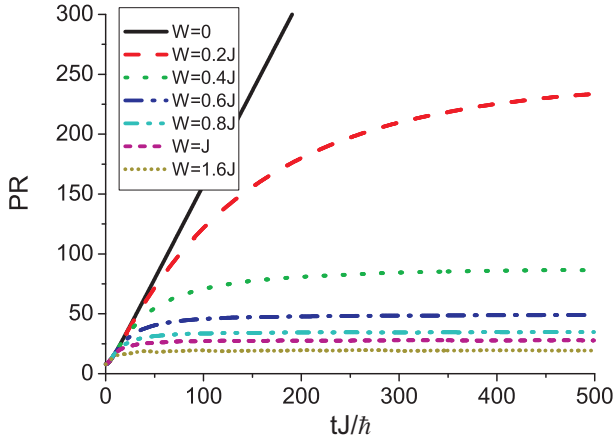

Figure 2.7: Time evolution of the participation ratio of a single particle for various disorder strengths. Other parameters as in Fig. 2.6.

$k = 0$ decreases quickly during time evolution until a stationary regime is reached, in which the value of $n_{k=0}$ is oscillating with a small amplitude ($\sim 1\%$). The scaling analysis for the value of $n_{k=0}$, time-averaged over the small oscillations, is shown in Fig. 2.5 for a half-filled system of mobile bosons. The occupation of the zero momentum state $n_{k=0}$ increases approximately like $\sqrt{N}$ for small N, but it then deviates from an algebraic increase and saturates for larger N; a completely analogous behavior is found for the case of uncorrelated disorder. Hence the scaling of $n_{k=0}$ reveals a crossover from quasi-condensation to fragmentation, with close similarity to the case of adiabatic evolution described in Sec. 2.3.2; in analogy to that case, we conclude that the steady state reached by time evolution realizes *dynamically* a Bose glass.

2.3.4 Transport Properties

In this section we discuss the expansion properties of initially confined mobile bosons in the potential created by the frozen particles. The initial confinement for the mobile particles is provided by a tight parabolic trap ($V > 0$), while the frozen particles can be imagined as prepared in a much shallower trap, whose effect is ignored for simplicity, so that the random potential they generate is the same as the one studied in the homogeneous case in Sec. 2.3.1. In particular we imagine that at time $t = 0$ the trap

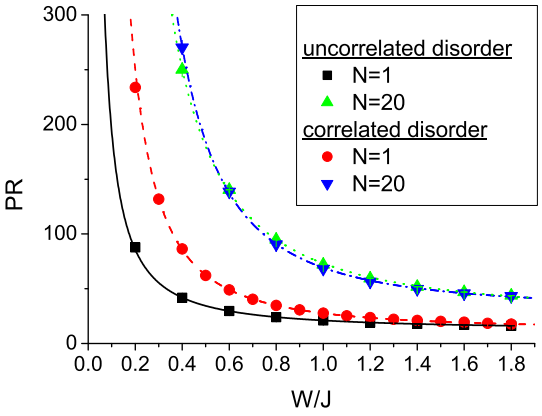

Figure 2.8: Steady-state participation ratio (recorded at $t = 500\hbar/J$) for N particles, time-evolved in a system of size $L = 702$ starting from the ground state of a harmonic trap ($V = 0.01J$) and interacting with a correlated random potential or with a fully uncorrelated random potential. The lines show a fit to the data points with an algebraically decaying function.

confining the mobile bosons is released ($V = 0$) and simultaneously the two species are brought into interaction ($W > 0$). After release from the trap, the mobile particles would expand forever in absence of disorder, so that a halt in presence of disorder explicitly shows localization effects.

The first subsection deals with the evolution of the real-space properties during expansion, while the second subsection studies the evolution of the condensation properties of the system.

Real-space localization

In this subsection we focus on the real-space properties of the time-evolved hardcore bosons in the frozen-boson potential, starting from a confined state in a parabolic trap. Snapshots from a disorder-averaged time evolution of a *single* particle starting from the ground state in the trap are depicted in Fig. 2.6. It is shown that the expansion reaches a *localized* steady state in the long-time limit; in particular the spatial decay of the particle density undergoes a dramatic change from *Gaussian* - as expected in a parabolic trap - to *exponential* - as expected in presence of Anderson

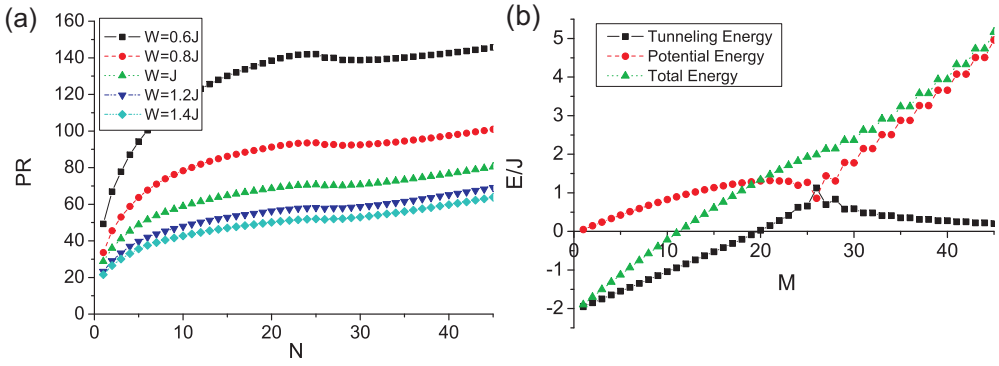

Figure 2.9: (a) Steady-state participation ratio (recorded at $t = 400\hbar/J$) of N particles as a function of the particle number for various disorder strengths. Other parameters as in Fig. 2.8. (b) Total, kinetic, and potential energy of the Mth single-particle eigenstate of the initial system in the trap.

localization. Hence an Anderson localized state is realized dynamically during expansion; it is fundamental to stress that this steady state does not correspond to the ground state of the system, as the energy of the particle is conserved during expansion and hence it does not relax to the ground-state value.

The dynamical localization of the single particle wavefunction is fully captured by the time evolution of the PR, depicted in Fig. 2.7 for various strengths W of the disorder potential. Without disorder, the wavefunction spreads ballistically without changing its Gaussian shape [RM04b]. In the presence of disorder, the PR saturates instead to a finite value, which decreases when increasing the disorder potential; a fit to the final value of the PR, shown in Fig. 2.8, suggests that saturation in the PR takes place for any arbitrarily small value of the potential, as it would be expected for uncorrelated disorder, although exploring very small strengths of the disorder is numerically demanding as the steady state is reached for prohibitively large values of the PR.

The time evolution of the participation ratio of many particles initially confined in a harmonic trap is similar to that exhibited by a single particle, and a saturation of the PR to a steady-state value is observed for the smallest value of W that we could treat numerically (Fig. 2.8).

Nonetheless, upon increasing the particle number in the trap beyond

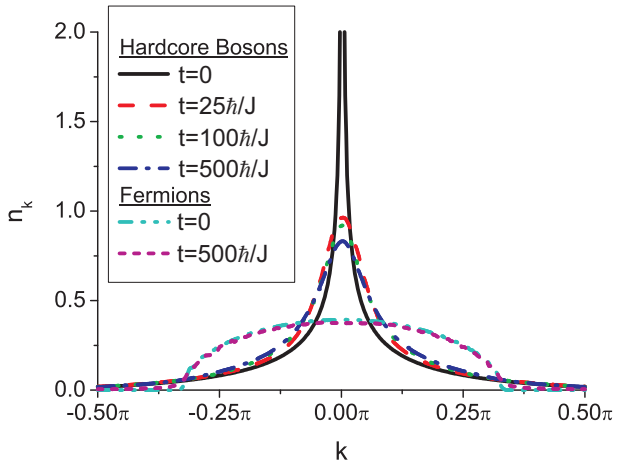

Figure 2.10: Snapshots of the time evolution of the momentum distribution n_k for a system of $N = 100$ hardcore bosons, initially in a trap with density $\tilde{\rho} = 0.5$, interacting with a correlated disorder potential. Here the system size is $L = 1002$ and the interaction strength is $W = 0.5J$. The momentum distribution for the corresponding spinless fermions is shown for comparison.

a critical value $N_c \approx 26$ (see Eq. (2.18) with $V = 0.01$) a Mott plateau at unit filling starts forming in the center, and the properties of the initial trapped ground state change drastically. It is then interesting to study whether the different initial conditions for the time evolution reflect themselves in the steady state of the system after the halt of the expansion. Fig. 2.9a shows the PR of the steady state as a function of the number of particles N. The steady state PR increases with the number of particles for $N \leq N_c$, showing a small peak for $N = N_c$ beyond which the increase with N is much slower. This feature can be understood in terms of the time evolution of the fermionic wavefunction Eq. (2.15), whose real-space properties such as the PR are equivalent to those of the hardcore bosons, and whose time evolution is simply obtained through the time evolution of single-particle eigenfunctions. For $N > N_c$ the single particle wavefunctions that are populated for increasing N are more and more confined to the sides of the trap, as the center has already a saturated density, and their energy is dominated by the trapping term, while the single-particle kinetic energy *decreases* with increasing N beyond N_c (see Fig. 2.9b). Given that the trapping energy vanishes at $t = 0$ after the trap release,

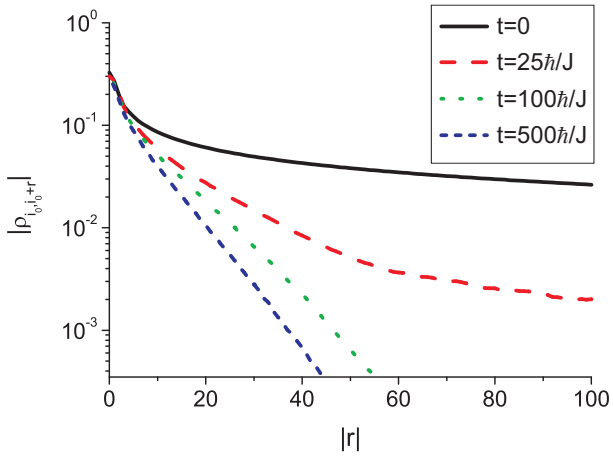

Figure 2.11: Decay of the modulus of the OPDM $|\rho_{i_0,i_0+r}|$ from the system center i_0 at various times during evolution. Parameters as in Fig. 2.10.

the fermions occupying levels beyond the N_c-th expand with an energy which is less than that of the N_c-th level, so that they are expected to be localized by the disorder potential with a final participation ratio which is similar (or even less than) that of the N_c-th particle. The time-evolved particle density of the many-body system is the simple sum of the squared time-evolved wavefunctions of the free fermions, so that the total participation ratio is not expected to increase significantly when adding particles beyond the N_c-th.

Coherence properties

In the previous subsection the real-space properties of initially confined hardcore bosons expanding in a disorder potential have been discussed. This subsection addresses the condensation properties of the same system, motivated by the rich physical scenario offered by expanding hardcore bosons in absence of disorder [RM04b, RM05b]. The first part is devoted to the time evolution of hardcore bosons initially confined in a superfluid state, while the second part analyses the expansion from a Mott insulator.

Time evolution starting from a superfluid state This part focuses on the expansion of the hardcore bosons initially confined in a shallow trap with characteristic density $\tilde{\rho} = 0.5$ (see Eq. (2.18)) well below the

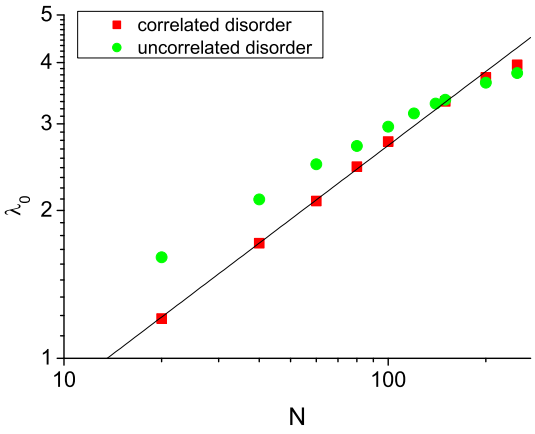

Figure 2.12: Scaling of the steady-state λ_0 (recorded at time $t = 500\hbar/J$) for varying number of particles in a system of size $L = 1502$; other parameters as in Fig. 2.10. The data for correlated frozen bosons are compared with those for fully uncorrelated ones. The line corresponds to a fit to $\lambda_0 \sim \sqrt{N}$.

critical value $\tilde{\rho}_c \approx 2.6$ for the onset of a Mott plateau in the trap center. With this initial condition quasi-condensation in the first NO is present, and the MDF is peaked around $k = 0$ at $t = 0$ [RM05b]. In the absence of disorder the MDF evolves towards that of the fermions (which is a constant of motion), namely the bosons *fermionize* in momentum space, although they still quasi-condense in the lowest NO which contains many momentum components [RM05b]. Furthermore, the OPDM is decaying algebraically like $\rho_{i,i+r} \sim |r|^{-0.5}$, showing quasi-long-range order, whereas the phase of the OPDM is oscillating at large distances leading to fermionization in momentum space. The decay of the OPDM is measured from the center of the trap, i.e., the center of the lowest NO and the site with maximum occupation.

We now move on to the analysis of the evolution of the MDF during expansion from a shallow trap in the presence of disorder created by the frozen bosons. The MDF of the mobile hardcore bosons is depicted in Fig. 2.10 at different times t, compared to the MDF of fermions in the same system. In presence of disorder the MDF of the fermions is no longer a constant of motion, but it is only slightly broadening in time due

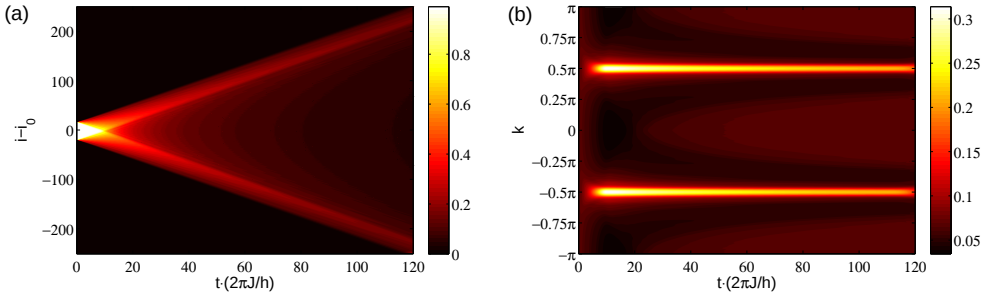

Figure 2.13: Time evolution of (a) the density profile and (b) the momentum distribution function of $N = 35$ hardcore bosons, initially in a perfect Mott insulator, in a system of size $L = 502$ without disorder.

to its interaction with the frozen species of particles. The effect of the disorder potential on the hardcore bosons is more significant. The $t = 0$ peak at zero momentum reduces its height, but, contrary to the expansion without disorder, it does not disappear and fermionization is not present. Following [RM05b], fermionization in absence of disorder is understood through the argument that, after a long-term expansion, the hardcore-boson system is dilute enough to be considered essentially non-interacting, and so it becomes equivalent to its fermionic counterpart. In presence of disorder, on the contrary, the expansion is stopped by localization, so that the extremely dilute limit is never reached and the hardcore bosons preserve their nature of strongly interacting particles. Furthermore, the interaction with a disorder potential leads to the loss of quasi-long-range order during time evolution, as shown in Fig. 2.11 by the decay of the OPDM at various times. The system finally reaches a steady state with an exponentially decaying OPDM.

The loss of quasi-long-range order during expansion strongly suggests the loss of quasi-condensation in the system. As the initial conditions break the translational symmetry, condensation properties are not captured by the scaling of the occupation of the zero-momentum state, and direct diagonalization of the disorder-averaged OPDM is necessary to extract the scaling of the occupation λ_0 of the lowest natural orbital. λ_0 decreases during time evolution, reaching a constant value in correspondence with the steady state observed in real-space. The scaling analysis of λ_0 is performed for this constant value in Fig. 2.12. The scaling of λ_0 deviates from the quasi-condensation behavior at sufficiently large particle

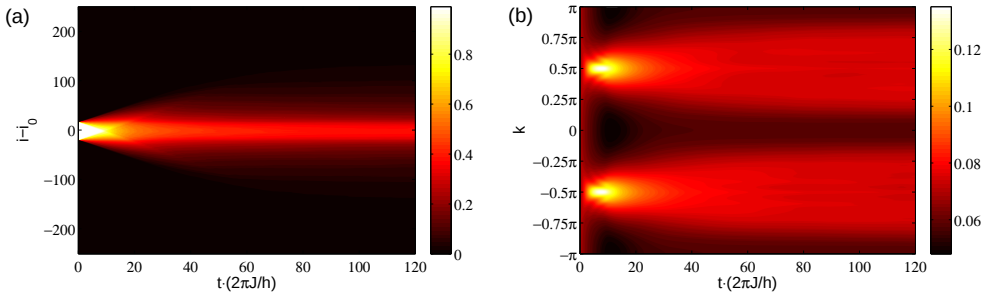

Figure 2.14: Time evolution of (a) the density profile and (b) the momentum distribution function of $N = 35$ hardcore bosons, initially in a Mott insulator, interacting with the disorder potential created by frozen particles at half-filling. Here the interaction strength is $W = 0.5J$.

numbers, revealing a crossover from quasi-condensation to fragmentation due to the localized nature of the lowest NO. Fully uncorrelated disorder leads to a similar behavior, although the crossover appears to be much broader, and a quasi-condensation regime at low N could not be identified.

Time Evolution starting from a Mott insulator As reported in [RM04b], hardcore bosons prepared in a perfect Mott insulating state (corresponding to an infinitely steep trap) and subsequently time evolved exhibit the phenomenon of dynamical quasi-condensation at finite momentum. Indeed, from the initially flat MDF of the Mott insulator two quasi-condensation peaks emerge at momenta $k = \pm\pi/2$ during time evolution [RM04b], as reproduced in Fig. 2.13. Strictly speaking quasi-condensation happens in two degenerate NOs whose Fourier transform is sharply peaked around $k = \pm\pi/2$; the NOs propagate at a velocity $v = \pm 2J$ corresponding to the maximal group velocities $\partial\epsilon_k/\partial k$ for the single-particle dispersion relation $\epsilon_k = -2J\cos k$ at momenta $k = \pm\pi/2$.

The occupation of the degenerate lowest NOs, λ_0, follows initially a universal power-law increase with time, independent of the number of particles N; at an N-dependent characteristic time τ_c, the two degenerate lowest NOs begin to move in opposite directions, and λ_0 starts to algebraically decrease, although its scaling with particle number shows the typical quasi-condensation behavior $\lambda_0 \sim \sqrt{N}$. The two lowest NOs

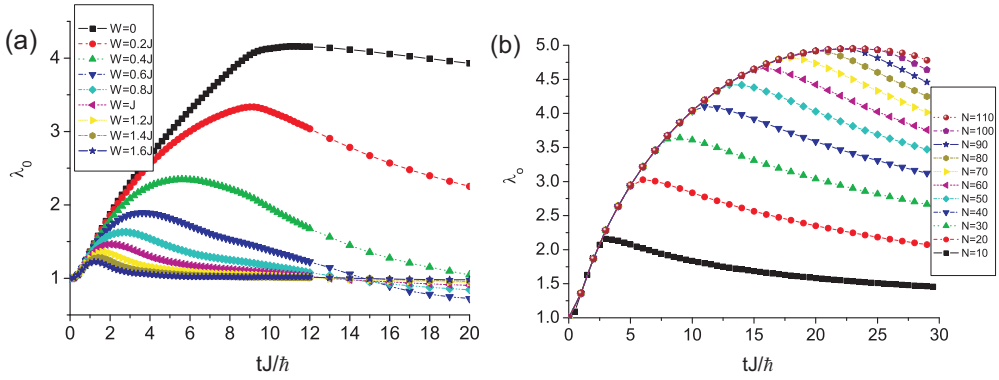

Figure 2.15: Time evolution of λ_0, (a) for various disorder strengths and $N = 35$ particles, (b) for various numbers of particles and disorder strength $W = 0.1J$. Other parameters as in Fig. 2.14.

clearly appear in the real-space densities as coherent fronts of the atomic cloud moving in opposite directions (see Fig. 2.13). This aspect suggests the use of this setup to produce an atom laser [RM04b].

We now consider the case of expanding hardcore bosons in the disorder potential created by frozen particles. Fig. 2.14 shows the density profile and the MDF for the expansion from a perfect Mott insulator in the presence of disorder created by frozen particles. Initially peaks at momenta $k = \pm\pi/2$ are emerging from the flat MDF at $t = 0$ as in the case without disorder, and the hardcore boson cloud shows two outer fronts expanding ballistically in opposite directions. Nonetheless this initially coherent expansion is rapidly suppressed due to localization, which leads to a decrease and broadening of the momentum peaks at larger times up to a final steady-state MDF in which two broad peaks survive, and which corresponds to a localized state in real space as seen in the previous subsection.

A deeper analysis of condensation effects relies on the NOs and their occupations. Figs. 2.15 show the time evolution of the largest eigenvalue λ_0 for different disorder strengths and different particle numbers. Initially λ_0 is two-fold degenerate, corresponding to reflection symmetry at the center of the system, and it increases following a universal power law independent of the particle number, similarly to what is observed in absence of disorder but with a different disorder-dependent exponent. As in the case $W = 0$, at a characteristic time τ_c the two degenerate natural

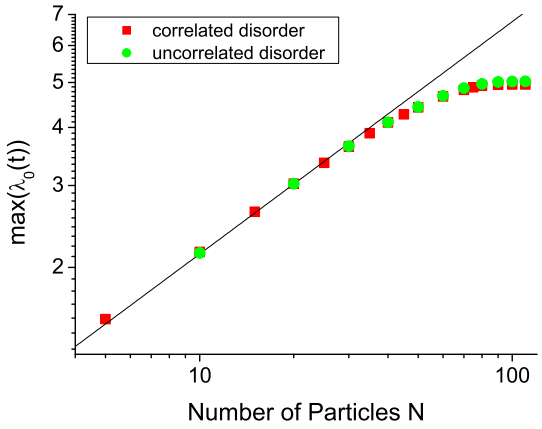

Figure 2.16: Scaling of the maximal value of λ_0 during time evolution of N hardcore bosons, initially in a Mott insulator. All parameters as in Fig. 2.15b. The line corresponds to a fit to $\lambda_0 \sim \sqrt{N}$ of the first four data points.

orbitals start to move into opposite directions, and correspondingly the time evolution of λ_0 turns into a decreasing behavior; τ_c strongly depends on the disorder strength (Fig. 2.15a), while its dependence on the particle number N becomes weaker for large N, where τ_c is seen to approach an asymptotic value (Fig. 2.15b). Unlike the case $W = 0$, at a later stage the expansion of the system is stopped by disorder, and the degeneracy in the lowest NOs is removed, going from two propagating ones to a single NO localized in the system center.

Hence the expanding system of hardcore bosons from a pure Mott state shows a crossover from an incipient quasi-condensation regime at finite momenta to a localization regime. It is natural to ask whether the system displays true quasi-condensation at any intermediate point in time. To address this issue, we perform a scaling analysis of λ_0 at the maximum-coherence time $t = \tau_c$. The results of this analysis are shown in Fig. 2.16, where λ_0 exhibits a clear saturation for large particle numbers, and hence a crossover from quasi-condensation to fragmentation. Repeating the same analysis for uncorrelated random disorder we find a scaling of λ_0 which is in qualitative agreement with the case of disorder generated by frozen particles (the apparent quantitative agreement is accidental).

2.4 Dynamical Doping

In this section, we theoretically explore a different scheme leading to localization in atomic mixtures, based on "dynamical doping" of frozen b-atoms into a cloud of mobile a-atoms. a and b-atoms represent two internal states of the same atomic species [HDR10].

Like in Sec 2.3, we use a state-dependent optical lattice to freeze one species and keep the other mobile. All N atoms are initially prepared in state $|a\rangle$, and occupy the motional ground state. Subsequently, a short radio-frequency Rabi pulse is applied, creating an internal-state superposition $\cos(\alpha/2)|a\rangle + \sin(\alpha/2)|b\rangle$, where α is the pulse area. We show that the frozen b component creates a quantum superposition of disorder potentials (see Fig. 2.17). The wavefunction of weakly interacting a-atoms in a two-dimensional lattice is studied numerically and evolves into a quasi-stationary profile with exponential tails. While we concentrate our discussion on bosons, our scheme should work equally well for fermions. The idea of dynamical doping can also generate new perspectives for other disordered systems.

The analysis of our scheme is interesting for several reasons:

1. The fact that dynamical doping results in localization is not obvious, because the Rabi pulse transfers a fraction $\sin^2(\alpha/2)$ of the population at each site into the frozen state $|b\rangle$. Without measuring the frozen atoms, no quantum projection noise is introduced and it is not *a priori* evident why the frozen atoms should generate disorder.

2. We show that the resulting disorder potential has negligible spatial correlations, unlike the most recent realizations in cold atom experiments [FLG$^+$06, WPM$^+$09, PMW$^+$10, BJZ$^+$08, RDF$^+$08, DZR$^+$10].

3. The experimental implementation of this scheme should be significantly simpler than the previously proposed schemes for disorder in atomic mixtures [PVC05, RC07, HCR07], e.g. the one discussed in Sec. 2.3. These schemes involve either the diabatic preparation of quantum emulsion states, whose statistics is controlled by the initial state and preparation scheme [RC07]; or the individual preparation of each species on disjoint optical lattices, and the subsequent relative motion of the two lattices to achieve coupling of the mobile particles to the disorder potential [PVC05, HCR07].

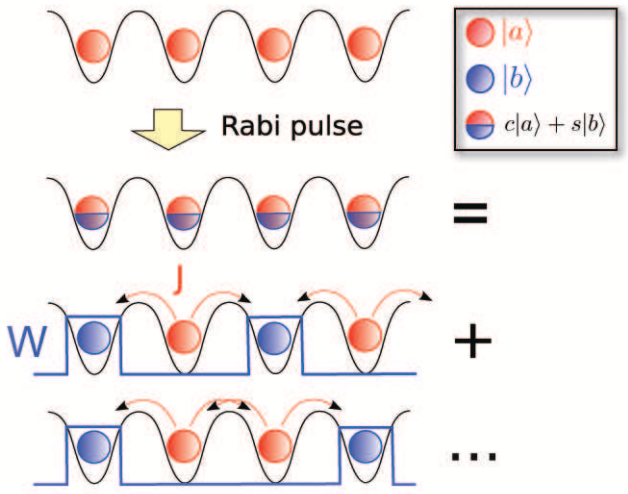

Figure 2.17: Sketch of atom localization in state-dependent optical lattices. The mobile a-atoms, initially prepared in the ground state of the lattice, are converted to a quantum superposition $\cos(\alpha/2)|a\rangle + \sin(\alpha/2)|b\rangle$ by a Rabi pulse, where the b-atoms are frozen by the lattice. The state of the system can be viewed as mobile a-atoms (red) moving in a quantum superposition of random potentials created by the frozen b-atoms (blue).

4. Due to the quantum parallelism, single-shot experiments with large atom numbers directly provide disorder averages.

The structure of this section is as follows. In Sec. 2.4.1 we introduce our description for an optical lattice with two species of bosons, discuss the preparation scheme, analyze the generated disorder potential, and explain our numerical procedure. We present and discuss the signatures for Anderson localization appearing in this system after the dynamical doping of frozen bosons in Sec. 2.4.2.

2.4.1 System and Method

In this section we first give a Hamiltonian description for the dynamics of two bosonic species in an optical lattice and the process of dynamical doping. Then we specialize on the case of weakly interacting bosons and examine the nature of the correlations in the disorder potential created by the frozen species. Finally, we give details on our numerical calculations.

Hamiltonian Dynamics

Our system consists of mobile a and frozen b-bosons trapped in the lowest band of an optical lattice, described by the Hamiltonian $\mathcal{H}$ from Eqs. (2.2)-(2.5). Here we consider both species to be confined by the same harmonic trap $V = V^{\mathrm{f}}$.

The system initially contains only the mobile bosons in the ground state of the Hamiltonian $\mathcal{H}_0$, which can be expanded in the basis of lattice Fock states

$$|\Psi\rangle_{t=0-} = \sum_{\{n_i\}} C(\{n_i\}) \left(\prod_i \frac{1}{\sqrt{n_i!}} (a_i^\dagger)^{n_i} \right) |0\rangle \tag{2.31}$$

subject to the constraint $\sum_i n_i = N$.

Under the assumption that the Rabi pulse is fast compared to the Hamiltonian dynamics, the application of a pulse instantaneously rotates the bosonic operators on all sites

$$a_i^\dagger \to \cos(\alpha/2) a_i^\dagger + \sin(\alpha/2) a_i^{\mathrm{f}\dagger}. \tag{2.32}$$

The resulting state can be expanded as a quantum superposition of many partitions of the N atoms over the mobile and the frozen species

$$|\Psi\rangle_{t=0+} = \sum_{\{n_i\},\{n_i^{\mathrm{f}}\}} \tilde{C}\left(\{n_i\},\{n_i^{\mathrm{f}}\}\right) |\{n_i^{\mathrm{f}}\}\rangle \otimes |\{n_i\}\rangle \tag{2.33}$$

under the constraint $\sum_i \left(n_i + n_i^{\mathrm{f}}\right) = N$. This state can be rewritten as

$$|\Psi\rangle_{t=0+} = \sum_{\{n_i^{\mathrm{f}}\},\sum_i n_i^{\mathrm{f}} \leq N} c(\{n_i^{\mathrm{f}}\}) |\{n_i^{\mathrm{f}}\}\rangle \otimes |\Phi(\{n_i^{\mathrm{f}}\})\rangle_{t=0}, \tag{2.34}$$

where

$$|\Phi(\{n_i^{\mathrm{f}}\})\rangle_{t=0} = c(\{n_i^{\mathrm{f}}\})^{-1} \sum_{\{n_i\}} \tilde{C}\left(\{n_i\},\{n_i^{\mathrm{f}}\}\right) |\{n_i\}\rangle \tag{2.35}$$

is the normalized state of the mobile bosons subject to the constraint of having a Fock state $|\{n_i^{\mathrm{f}}\}\rangle$ of the frozen bosons. $c(\{n_i^{\mathrm{f}}\})$ is a normalization constant and can be chosen to be real.

The subsequent time evolution of the system is governed by the full Hamiltonian $\mathcal{H}$. The evolved state at time t, $|\Psi\rangle_t$, can again be expanded in the form of Eq. (2.33). We now assume that tunneling of the (frozen)

b-bosons is negligible, $J^{\mathrm{f}} = 0$, so that they are frozen in the Fock states $|\{n_i^{\mathrm{f}}\}\rangle$. Hence, the mobile boson components in Eq. (2.35) evolve decoupled from each other as

$$|\Phi(\{n_i^{\mathrm{f}}\})\rangle_t = \exp[-i\mathcal{H}(\{n_i^{\mathrm{f}}\})t/\hbar]|\Phi_a(\{n_i^{\mathrm{f}}\})\rangle_{t=0}. \tag{2.36}$$

We will argue in this subsection that the Hamiltonian of the frozen bosons $\mathcal{H}_{\mathrm{f}}$ does not contribute to the interesting dynamics such that this equation again assumes the form of Eq. (2.11). At time t, observables A, referring to mobile bosons only, take the expectation value [PVC05]

$$\langle A\rangle_t = \sum_{\{n_i^{\mathrm{f}}\}} \left|c\left(\{n_i^{\mathrm{f}}\}\right)\right|^2{}_t\langle\Phi(\{n_i^{\mathrm{f}}\})|A|\Phi(\{n_i^{\mathrm{f}}\})\rangle_t, \tag{2.37}$$

which describes the average over parallel quantum evolutions of the mobile bosons in all possible realizations of the static potential $V_i = Wn_i^{\mathrm{f}}$ generated by the frozen bosons. These realizations follow the statistics dictated by the $|c(\{n_i^{\mathrm{f}}\})|^2$ coefficients, which are completely controlled by the choice of the initial state of the bosons. In particular, if this state is homogeneously spread over a given region of space, the distribution of the resulting effective potential will be dominated by configurations in which a number $\sim N\sin^2(\alpha/2)$ of frozen bosons is randomly scattered over this region, hence giving rise to an effective disorder potential. Note that in contrast to the proposal in Sec. 2.3 the number of frozen bosons N^{f} is not fixed here.

With $J^{\mathrm{f}} = 0$, the Hamiltonian $\mathcal{H}_{\mathrm{f}}$ obviously contributes only a phase factor to the time evolution of each $|\Phi(\{n_i^{\mathrm{f}}\})\rangle_t$. This has no effect in Eq. (2.37). Hence, $\mathcal{H}_{\mathrm{f}}$ can be omitted in our numerical calculations below. Furthermore, if there is spin decoherence, i.e., if the relative phase of states a and b fluctuates due to experimental imperfections, this will cause fluctuations in the phases of all the $|\Phi(\{n_i^{\mathrm{f}}\})\rangle_t$ in Eq. (2.34). This also has no effect in Eq. (2.37). This insensitivity to spin decoherence is a strength of our scheme.

Weakly interacting bosons and disorder statistics

In the following, we consider weakly interacting ($U \lesssim J$) Bose gases. To analyze the statistical properties of the disorder, we describe the state before the Rabi pulse with a condensate wavefunction on a lattice [BDZ08]

$$|\Psi\rangle_{t=0} = \frac{1}{\sqrt{N!}}\left(\sum_i \psi_i a_i^\dagger\right)^N |0\rangle =: |\{\psi_i\}\rangle^{\otimes N}, \tag{2.38}$$

which is a good approximation far from the superfluid-to-Mott-insulator transition (occurring for $U/J \sim 16$ with $n = 1$). Here, $\psi_i = \Psi_i/\sqrt{N}$ is the effective single-particle state. After the Rabi pulse, Eq. (2.32), the state can be written in the form of Eq. (2.34) with $\left|\Phi(\{n_i^{\mathrm{f}}\})\right\rangle_{t=0} = |\{\psi_i\}\rangle^{\otimes(N-N^{\mathrm{f}})}$ and

$$\begin{aligned}\left|c\left(\{n_i^{\mathrm{f}}\}\right)\right|^2 &= \left(\sin^2\alpha/2\right)^{N^{\mathrm{f}}}\left(\cos^2\alpha/2\right)^{N-N^{\mathrm{f}}} \\ &\quad\times\frac{N!}{(N-N^{\mathrm{f}})!}\prod_i\frac{|\psi_i|^{2n_i^{\mathrm{f}}}}{n_i^{\mathrm{f}}!}.\end{aligned} \tag{2.39}$$

The $|c|^2$ coefficients describe the statistics of a random potential with an average number of frozen bosons per site $\langle n_i^{\mathrm{f}}\rangle = \langle N^{\mathrm{f}}\rangle\,|\psi_i|^2$ and an average total number of frozen bosons $\left\langle N^{\mathrm{f}}\right\rangle = N\sin^2(\alpha/2)$. The correlations in the disorder potential can be described by the density-density correlation function $g_{ij}^{(2)}$, taking the expression

$$g_{ij}^{(2)} = \frac{\langle b_i^\dagger b_j^\dagger b_i b_j\rangle}{\langle b_i^\dagger b_i\rangle\langle b_j^\dagger b_j\rangle} = 1 - \frac{1}{N}. \tag{2.40}$$

Therefore, for large N the magnitude of the disorder potential on different sites can be regarded as independent. Thus, in contrast to speckle potentials, our proposal does not suffer from problems with the autocorrelation in the disorder potential. The disorder distribution is, however, inhomogeneous because of the external trapping potential.

In our simulations, we take $N = 50$ bosons, a two-dimensional $L \times L$ lattice with $L = 60$ and $V = V^{\mathrm{f}} = \frac{m}{2}\omega^2 d^2 = 0.004J$ which yields a density $\langle n\rangle \leq 1$ throughout the trap ($\langle n\rangle \approx 1$ for the $U = 0$ case). Here, $d = \lambda/2$ is the lattice spacing. We determine $|\psi_i|^2$ by numerically minimizing the Gross-Pitaevskii (GP) energy functional [PS02]

$$E = -J\sum_{\langle ij\rangle}\left(\Psi_i\Psi_j^* + \text{c.c.}\right) + \sum_i\left(\frac{U}{2}|\Psi_i|^2 + V(i-i_0)^2\right)|\Psi_i|^2 \tag{2.41}$$

subject to the condition that the total number of particles be fixed to N. Next, we generate disorder realizations $\{n_i^{\mathrm{f}}\}$ according to the $|c|^2$ statistics of Eq. (2.39) via standard Monte Carlo Metropolis sampling (see Eq. (2.25)). We are sampling over approximately 100 independent disorder realizations. Finally, we numerically solve the time-dependent GP equation governed by the Hamiltonian $\mathcal{H}$ to calculate the time evolution after the pulse.

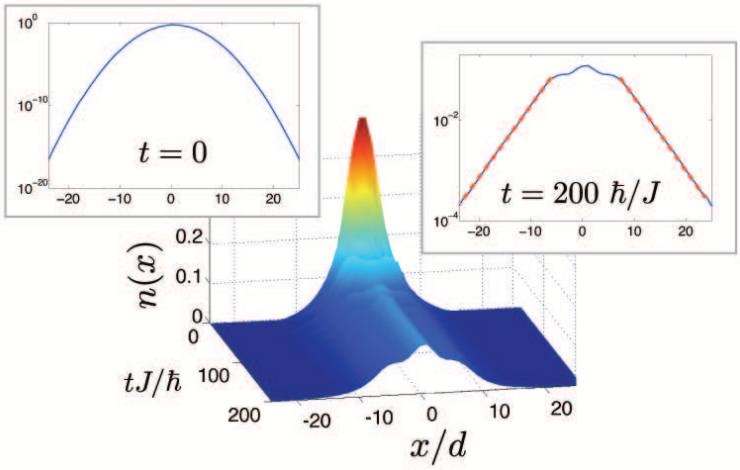

Figure 2.18: Time-evolution of the density profile $n(x) = \langle n_{x/d} \rangle$ for the non-interacting gas, $U = 0$, after a pulse of duration $\alpha = \pi/2$ and with interspecies interaction $W = 7J_a$.

2.4.2 Dynamical Localization

Now we can proceed with the discussion of the results of our numerical simulations. Fig. 2.18 shows the time evolution of the density profile of the mobile bosons for $U = 0$, $W = 7J$, $\alpha = \pi/2$. After the Rabi pulse at $t = 0$, the cloud of mobile bosons rapidly expands from its initially Gaussian state, due to the repulsion from the dynamically doped frozen bosons. The expanding cloud wings are then reflected by the trap. This generates breathing oscillations, which are quickly damped by the disorder. Remarkably the resulting, quasi-stationary density profile features a central peak with exponentially decaying tails, $\langle n_i \rangle \sim \exp(-|\boldsymbol{r}_i - \boldsymbol{r}_0|/\xi)$, clearly exhibiting Anderson localization. A similar behavior is observed for $U > 0$ and for different values of W and α. Yet, the dependence of the localization phenomenon on these parameters is nontrivial and differs significantly from what one expects at equilibrium.

The fast, diabatic Rabi pulse takes the system out of the initial ground state into an excited non-equilibrium state. According to Eq. 2.39, the remaining mobile bosons occupy a superposition of different condensate states with variable particle number $N - N^{\mathrm{f}}$; these condensate states are non-equilibrium ones because they are immersed in the disordered background of frozen bosons, and because, in presence of finite interactions

$U > 0$, the condensate wavefunction is no longer minimizing the interaction energy for a reduced particle number $N - N^{\mathrm{f}}$. To quantify the distance from equilibrium, we evaluate the energy transfer per mobile boson due to the Rabi pulse

$$\delta\varepsilon = \frac{\langle \mathcal{H}_0 + W \sum_i n_i n_i^{\mathrm{f}} \rangle_{\mathrm{after}}}{N \cos^2(\alpha/2)} - \frac{\langle \mathcal{H}_0 \rangle_{\mathrm{before}}}{N}, \tag{2.42}$$

where $\langle ... \rangle_{\mathrm{before(after)}}$ denotes the expectation value over the wavefunction before (after) the pulse. Fig. 2.19 clearly shows that the transferred energy $\delta\varepsilon$ increases for increasing disorder strength (namely for increasing α and W), while it decreases for increasing interactions U. This is partly due to the fact that, for a given initial distribution (controlled uniquely by the U/J ratio and by the trapping potential), the gain in on-site interaction for the mobile bosons is $\propto W - U/2$, namely it increases linearly with W. On the other hand, increasing U reduces the probability that many a-bosons occupy the same site before the Rabi pulse; this latter fact reduces the probability that, immediately after the pulse, a site will be occupied by both mobile and frozen bosons, and this reduces $\delta\varepsilon$.

So on the one hand, the equilibrium physics suggests that stronger localization should occur for stronger disorder W and for weaker interactions U, due to reduced screening [KM93, DZR$^+$10]. On the other hand, the non-equilibrium physics suggests the exact opposite, namely that stronger W and weaker U both increase $\delta\epsilon$, so that the mobile bosons expand more violently, making the wings of the quasi-stationary density profile fall off more slowly, and therefore increasing the localization length ξ. The evolution of ξ in Fig. 2.19 shows that the non-equilibrium aspects dominate in this competition. Note that, for larger ξ, the density profile exhibits exponential tails over a larger spatial range, which facilitates the experimental observation of the tails (The spatial support of the disorder distribution is finite, being the same as that of the condensate wavefunction before the pulse. Part of the mobile bosons can expand beyond this region, so that the extreme tails do not belong to the localized wavefunction, but to the wavefunction transmitted through the disorder.)

While the real-space localization exhibits counterintuitive, non-equilibrium properties, the coherence properties of the expanding cloud exhibit instead a more intuitive behavior. We consider the momentum distribution of the mobile bosons, $\langle n_k \rangle_t = \sum_{i,j} e^{-ik(i-j)} \langle a_i^\dagger a_j \rangle_t / L^2$ right after the pulse ($t = 0$) and after time evolution to a quasi-stationary state

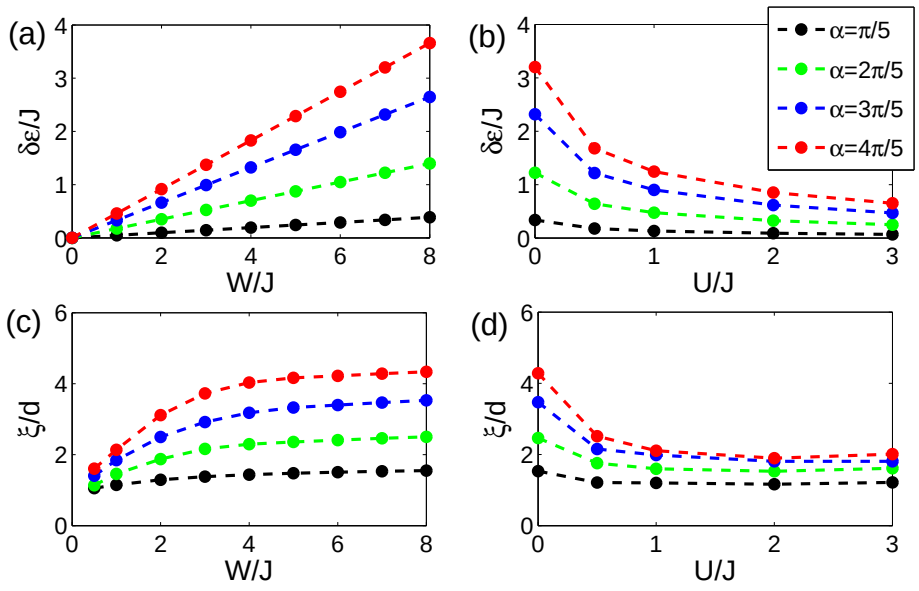

Figure 2.19: Lower panels: localization length (in units of the lattice spacing d) of the evolved cloud for a non-interacting gas of mobile bosons ($U = 0$, left), and for interacting mobile bosons with $W = 7J$ (right). Upper panels: corresponding transferred energy per mobile boson.

($t = t_{\max} = 200\hbar/J$), and we monitor the loss of coherence during evolution via the relative coherent fraction $R = \langle n_{k=0}\rangle_{t_{\max}}/\langle n_{k=0}\rangle_{t=0}$. Fig. 2.20 shows that the relative coherent fraction is suppressed for increased disorder strength (larger α), showing that, although the cloud displays exponential tails with a longer ξ, the internal phase coherence is spoiled by disorder more effectively. This effect is reduced upon increasing the repulsion strength U, showing that disorder screening is indeed observed in the cloud core, which is the part contributing more significantly to the overall coherence properties.

2.5 Experimental Realization

While our proposals are quite general, we wish to point out that an experimental implementation is feasible with existing technology in ultra-

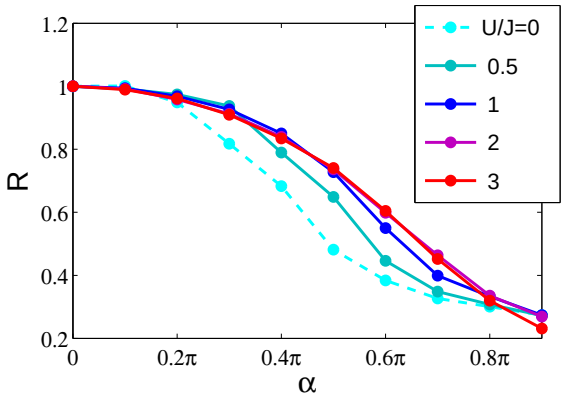

Figure 2.20: Relative coherent fraction R after time evolution (see text) for $W = 7J$.

cold gases. However it is more straightforward to implement the dynamical doping scheme (see Sec. 2.4). Thus we will begin with the description of its implementation, in a way that all relevant parameters can be adjusted independently. One could, e.g. choose ^{87}Rb atoms with hyperfine states $|a\rangle = |F = 1, m_F = 1\rangle$ and $|b\rangle = |F = 2, m_F = 2\rangle$. For circularly-polarized lattice light, there is a so-called magic wavelength near 787 nm where the mobile a-atoms see no lattice potential [JBC$^+$99, BCJ$^+$99, JZ04, MDW02]. The ratio of the tunneling amplitudes J/J^{f} can be adjusted over a wide range by tuning the wavelength λ near the magic wavelength. Hence, one can make J^{f} very small, thus freezing the b-bosons. A Feshbach resonance [CGJ$^+$10] for state $\big|a\rangle$ can be used to adjust the interaction strength U. Due to the state-selective character of Feshbach resonances, this leaves the interspecies interaction strength W unchanged. The intensity of the lattice light controls W/J. Finally, this choice of states $\big|a\rangle$ and $\big|b\rangle$ is stable against spin exchange and it is only subject to very slow dipolar relaxation [PS02].

For the case of an independent preparation of the two species (see Sec. 2.3) further techniques must be applied. As shown in [MGW$^+$03] it is possible to coherently control the phase between the two polarization components, i.e., between the two optical lattices. Hence, if the two polarization components are initially shifted by $\pi/2$ in space, the two species are non essentially interacting (see Fig. 2.2). The possibility of increasing drastically the intensity of one of the two polarization components would

allow for a sudden quench of the hopping of one of the two species, preparing in this way the quantum superposition of random potentials. The two species can be then brought into interaction at different strengths by shifting the spatial phase between the two polarization components of the lattice. An adiabatic shift would transfer the mobile species to the Bose-glass ground state in the random potential, as discussed in Sec. 2.3.2, whereas a sudden shift would give rise to an out-of-equilibrium Bose-glass state as steady state after a transient evolution, as discussed in Sec. 2.3.3. As demonstrated in [PWM$^+$04], the hardcore regime is achieved by using deep lattices for both polarization components and extremely dilute gases of both hyperfine states, so that a density of less than one atom per site is achieved in the lattice after loading.

As seen in Sec. 2.3.4, expansion experiments in the disorder potential require to confine the two components with strongly different trapping frequencies, and then to release one of the two traps independently of the other. Making use of the selective coupling of different hyperfine states to different polarization components of a magic-wavelength laser, it is possible to more strongly confine one of the two species through an optical dipole trap obtained by a tightly focused and polarized laser propagating transverse to the chain direction in the one-dimensional optical lattice.

Throughout this chapter we have seen that the onset of localization leaves very strong signatures on the momentum distribution, which is observed in standard time-of-flight experiments [GME02]. Moreover expansion experiments in the disorder potential lead to exponentially localized steady states, whose density profiles can be measured with a single-site resolution. Atom microscopes with this resolution have been demonstrated recently [SWE$^+$10, BGP$^+$09].

2.6 Conclusion

In this chapter we have shown that bosonic gases undergo genuine quantum localization effects when set into interaction with a secondary species of bosons frozen in a massive quantum superposition of Fock states. Each Fock state can be regarded as a realization of a random potential, and the unitary evolution of the mobile species of bosons follows all possible paths related to the various disorder realizations *in parallel*. A rich disorder statistics can be generated by state preparation of the system before the pulse [PVC05].

In Sec. 2.3 we propose to prepare the frozen bosons in the superfluid state of one-dimensional hardcore bosons, realizing a rapidly fluctuating disorder potential over the length scale of a few lattice spacings; despite its power-law decaying correlations, this disorder potential is found to lead to the same localization effects as those observed in a *fully uncorrelated* potential. The equilibrium state of the hardcore bosons in the random potential is found to be a homogeneous Bose-glass state with exponentially decaying correlations; a similar state can be realized also dynamically after a sudden on-turn of the interaction between the two species. When the hardcore bosons are initially confined in a tight trap and then set free to expand in the random potential, for any non-vanishing disorder strengths the expansion stops and the system reaches an exponentially localized state [HCR07]. For any setup discussed in this section we observe the absence of quasicondensation and quasi-long-range order due to the disorder potential.

Alternatively, we have proposed an experimentally simpler scheme in Sec. 2.4. By dynamically doping frozen weakly interacting bosons into the system via a Rabi pulse, novel, non-equilibrium disorder effects on the many-body state of bosons trapped in a spin-dependent optical lattice can be observed. After the the release from a tight trap, the weakly interacting bosons evolve into an exponentially localized steady state with reduced coherence. [HDR10].

Our predictions can be tested by state-selective time-of-flight measurements and *in-situ* imaging of the bosonic cloud (see Sec. 2.5). Hence disorder created by a species of frozen hardcore bosons represents a very robust way to experimentally implement strongly fluctuating random potentials in optical lattices, and to realize fundamental localization effects of many-body systems. Moreover, an experimental implementation of dynamical doping is particularly desirable, as it could access the regime of strongly interacting mobile atoms on the verge of the superfluid-to-Mott transition, which remains challenging for all current theoretical approaches.

Chapter 3

Decoherence Dynamics

3.1 Introduction

The control and manipulation of systems in the quantum regime has seen great progress in recent years [SVB+08]. Research goals include the quantum simulation of condensed matter systems [BN09] as well as the realization of quantum computers [ZBB+05]. In this field decoherence is traditionally regarded as the main obstacle, which has to be avoided or corrected for [Sho95]. An alternative view on decoherence has recently been proposed [VWC09, KBD+08]. One can make use of decoherence and engineer the interaction of a quantum system with a reservoir. This allows for the preparation of any desired state as the steady state of a dissipative evolution.

In systems of cold atoms the quantum simulation of strongly correlated states has so far been achieved by cooling to the ground state of nicely tunable Hamiltonians [BDZ08]. Recently it has been found how to prepare Bose-Einstein condensates [DMK+08], superconducting d-wave states [DYD+10], three-body interactions [DTD+09], and Pfaffian states [RRC10] by engineering local dissipation. Beyond the preparation of interesting states, the full non-equilibrium phase diagram has been mapped out in these systems [DTM+10]. The experimental realization of a dissipative quantum simulation has been achieved in a similar project [SBL+08, DGS+09, GDS+09] based on naturally present two-body losses. These losses dynamically enforce a hardcore constraint on the atoms generating the strongly-correlated Tonks-Girardeau phase. Another line of active research is the creation of entanglement for quantum information

processing. It has been proposed [MPC10] and experimentally verified [KMJ+10] that the engineering of a dissipative process allows for the generation and maintenance of entanglement in atomic systems. Also quantum memories can be protected by engineered dissipation [PCC11].

In this chapter we are studying the dependence of the decoherence dynamics on the physics of the system. We show that the asymptotic decoherence rate, i.e., the decoherence rate at late times, or the steady state reflect a phase transition of the system in the limit of weak system-bath couplings. The decoherence dynamics undergo a dissipative phase transition if the system shows a quantum phase transition. Assumping Markovian dynamics, i.e., memoryless baths, we can resort to the Lindblad master equation to describe the decoherent dynamics [Lin76]. In particular, we are studying the anisotropic quantum XY chain in a transverse magnetic field containing the prototype of a continuous phase transition [Sac99]. We point out that this dissipative quantum simulator can be experimentally realized in systems of cold ions with currently available techniques.

To this end we develop a mathematical framework that allows to exactly solve the dynamics of non-interacting, i.e., quadratic, fermionic systems for certain relevant Lindblad master equations. Note that our framework also applies to the systems studied in [Pro08, Pro10] where quadratic fermionic systems are coupled to a Markovian bath with Lindblad operators which are linear in the fermionic creation/annihilation operators. However, such systems require underlying Hamiltonians, which are linear in these fermionic operators and thus violate causality [Pop00].

This chapter is structured as follows. In Sec. 3.2 we are introducing the Lindblad master equation which allows to describe decoherence due to the weak interaction with a Markovian bath. We are presenting the covariance matrix formalism, allowing the exact treatment of quadratic fermionic systems, and extend it to decoherent systems. Then we perform the analytic calculation of the steady states and the asymptotic decoherence rates in this framework in Sec. 3.3. As an example we apply this general result to the anisotropic XY chain in a transverse magnetic field in Sec. 3.4.1, and compare the interesting results, namely the display of quantum phase transitions in the decoherence rates, with numerical examples for finite system sizes, finite time evolutions, and finite interactions between system and bath in Sec. 3.4.2. The comparison with an example system which cannot be solved exactly in Sec. 3.5 shows that phase transitions are displayed in the dissipative dynamics for a wide class of

systems. In Sec. 3.6 we propose a possible implementation of this quantum simulation with cold ions, before giving concluding remarks in Sec. 3.7.

3.2 System and Method

In this section we introduce the Lindblad master equation, the dynamical equation describing the interaction of a system with a Markovian bath (see Sec. 3.2.1). We further describe the fermionic covariance matrix formalism which is ideally suited for describing non-interacting and spinless fermionic systems, and extend this formalism to systems in contact with a bath (see Sec. 3.2.2). We discuss the representation for all translationally invariant fermionic systems in one dimension (see Sec. 3.2.3). Finally, we describe the Jordan Wigner transformation which allows to transform some exactly solvable one-dimensional spin systems, especially the anisotropic XY-chain in a transverse magnetic field, into non-interacting fermionic systems (see Sec. 3.2.4).

3.2.1 Lindblad Master Equation

In this chapter we treat the decoherence of a system in contact with a heat bath with the Lindblad master equation [Lin76]

$$\partial_t \rho = -\frac{i}{\hbar}\left[\mathbf{H}, \rho\right] + \sum_\alpha \left(\mathbf{L}^\alpha \rho \mathbf{L}^{\alpha\dagger} - \frac{1}{2}\left\{\mathbf{L}^{\alpha\dagger}\mathbf{L}^\alpha, \rho\right\}\right), \tag{3.1}$$

where ρ is the density matrix of the system, $\mathbf{H}$ is its Hamiltonian, and the Lindblad operators $\mathbf{L}^\alpha$ determine the interaction between the system and the bath. This dynamical equation for an open system can be derived from two different points of view [BP02]. First, it can be derived from the full dynamics of system and bath. Here three major approximation have to be used: The state of system and environment are initially uncorrelated, the coupling between system and bath is weak (Born approximation), and the environment equilibrates fast (Markov approximation). Second, this Lindblad equation describes the dynamics of a quantum dynamical semigroup. A quantum dynamical semigroup is a completely positive, trace preserving map, which is continuous and transitive in time.

Throughout most of this chapter we will restrict the discussion to the case of Hermitian Lindblad operators. Then we can rewrite the Lindblad

master equation (3.1)

$$\partial_t \rho = -\frac{i}{\hbar}\left[\mathbf{H}, \rho\right] - \frac{1}{2}\sum_{\alpha}\left[\mathbf{L}^{\alpha}, \left[\mathbf{L}^{\alpha}, \rho\right]\right]. \tag{3.2}$$

In terms of $\big|\rho\rangle$, the vector of components of ρ, this equation becomes

$$\partial_t \big|\rho\rangle = \mathcal{S}\big|\rho\rangle = \left(\mathcal{H} - \frac{1}{2}\sum_{\alpha}\big(\mathcal{L}^{\alpha}\big)^2\right)\big|\rho\rangle. \tag{3.3}$$

with the superoperators

$$\mathcal{H} = -\frac{i}{\hbar}\left(\mathbf{H}\otimes\mathbf{1} - \mathbf{1}\otimes\mathbf{H}^{\mathrm{T}}\right), \tag{3.4}$$

$$\mathcal{L}^{\alpha} = \mathbf{L}^{\alpha}\otimes\mathbf{1} - \mathbf{1}\otimes\mathbf{L}^{\alpha\mathrm{T}}. \tag{3.5}$$

We will later use that the superoperator $\mathcal{H}$ is anti-Hermitian and that the superoperators $\mathcal{L}^{\alpha}$ are Hermitian, so that the $\big(\mathcal{L}^{\alpha}\big)^2$ are Hermitian and non-negative.

3.2.2 Covariance Matrix Formalism

Now we will present a framework in which the dissipative dynamics of the Lindblad master equation (3.2) can be solved exactly. We are focusing on fermions with N creation and annihilation operators $a_i^{\dagger}$ and a_i (system size N). These operators obey the canonical anti-commutation relations

$$\{a_k, a_l\} = 0, \;\; \left\{a_k^{\dagger}, a_l\right\} = \delta_{kl}. \tag{3.6}$$

We introduce fermionic Majorana operators

$$c_{k,0} = a_k^{\dagger} + a_k, \;\; c_{k,1} = (-i)\big(a_k^{\dagger} - a_k\big), \tag{3.7}$$

which as generators of the Clifford algebra satisfy the anti-commutation relations

$$\{c_{k,m}, c_{l,n}\} = 2\delta_{kl}\delta_{mn}. \tag{3.8}$$

We are describing the state of the system with its real and antisymmetric covariance matrix

$$\Gamma_{kl,mn} = \mathrm{tr}\left(\rho\frac{i}{2}\left[c_{k,m}, c_{l,n}\right]\right). \tag{3.9}$$

The magnitudes of the imaginary eigenvalues of Γ are smaller than or equal to unity. Pure states $\rho = |\Psi\rangle\langle\Psi|$ satisfy $\Gamma^2 = -\mathbb{1}$. In our notation Γ_{kl} denotes a 2×2 matrix that describes the coherence between sites k and l.

Here we concentrate on Hamiltonians and Lindblad operators which are quadratic in the fermionic Majorana operators

$$\mathbf{H} = \frac{i}{4} \sum_{klmn} H_{kl,mn} c_{k,m} c_{l,n}, \tag{3.10}$$

$$\mathbf{L}^{\alpha} = \frac{i}{4} \sum_{klmn} L^{\alpha}_{kl,mn} c_{k,m} c_{l,n}. \tag{3.11}$$

The matrices H and L^{α} are real and anti-symmetric for Hermitian Hamilton and Lindblad operators. All eigenstates and thermal states of these quadratic Hamiltonians are Gaussian and remain Gaussian under the evolution with quadratic Hamiltonians. Gaussian states have density operators which are exponentials of quadratic forms in the Majorana operators. For such Gaussian states all correlation functions are related to the covariance matrix through Wick's theorem. Because of this significance of the covariance matrix we concentrate on studying the system dynamics through the covariance matrix. We use the anti-commutation relations (3.8) to determine the dynamical equation for the covariance matrix Γ from Eq. (3.2)

$$\partial_t \Gamma = \frac{1}{\hbar} [H, \Gamma] + \frac{1}{2} \sum_{\alpha} \left[L^{\alpha}, [L^{\alpha}, \Gamma] \right]. \tag{3.12}$$

This equation is the analog of the Lindblad master equation in the covariance matrix formalism. We reformulate this equation for the vector of components $|\Gamma\rangle$

$$\partial_t |\Gamma\rangle = S|\Gamma\rangle = \left(\mathcal{H} - \frac{1}{2} \sum_{\alpha} \left(\mathcal{L}^{\alpha}\right)^2 \right) |\Gamma\rangle, \tag{3.13}$$

where $\mathcal{H}$ is anti-symmetric and $\left(\mathcal{L}^{\alpha}\right)^2$ is symmetric and non-negative analogous to the case of the density matrix (3.3). $|\Gamma\rangle$ is treated as an element of the vector space $\mathbb{C}^{2L}$ for N lattice sites in this notation, while only real and anti-symmetric covariance matrices are physically meaningful. This must be considered during the analysis.

3.2.3 Translationally invariant Hamiltonians

The Hamiltonian matrix H defined in Eq. (3.10) takes a special form for a translationally invariant Hamiltonian. The 2×2 matrices H_{kl}, corresponding to the interaction between sites k and l, only depend on the distance between the sites, i.e., $H_{kl} = H_{k-l}$, where the difference $k - l$ is understood as $k - l$ modulo N, taking into account periodic boundary conditions.

Any real anti-symmetric matrix can be transformed into a real and anti-symmetric block-diagonal matrix by an orthogonal transformation O. For the Hamiltonian matrix H this means

$$H'_{kl,mn} = \left(OHO^T\right)_{kl,mn}, \; H_{kl} = \delta_{kl} \begin{pmatrix} 0 & \epsilon_k \\ -\epsilon_k & 0 \end{pmatrix}, \tag{3.14}$$

where the real number ϵ_n are the energies of the elementary excitations. We, however, transform the Hamiltonian matrix with the unitary Fourier transform

$$\widetilde{H}_{kl,mn} = \left(UHU^\dagger\right)_{kl,mn}, \;\; U_{kl,mn} = \frac{1}{\sqrt{N}} e^{\frac{2\pi i}{N} kl} \delta_{mn}. \tag{3.15}$$

The resultant matrix $\widetilde{H}$ is anti-Hermitian, but not real. Therefore, we include also non-physical Hamiltonians in our calculations. The matrix $\widetilde{H}$ is block-diagonal

$$\widetilde{H}_{kl} = \delta_{kl} \sum_{\delta=0}^{N-1} H_\delta e^{-\frac{2\pi i}{N} \delta k}. \tag{3.16}$$

The block-diagonal is parametrized according to

$$\widetilde{H}_{mn} = \delta_{mn} \begin{pmatrix} ik_n & h_n \\ -h_n^* & il_n \end{pmatrix}, \;\; k_n, l_n \in \mathbb{R}, \; h_n \in \mathbb{C}. \tag{3.17}$$

For later use we observe the properties

$$h_{-n} = h_n^*, \;\; k_{-n} = -k_n, \;\; l_{-n} = -l_n. \tag{3.18}$$

The spectrum of the Hamiltonian matrix determines the elementary excitation energies

$$\epsilon_n = \left| \frac{k_n + l_n}{2} \pm \sqrt{\left(\frac{k_n - l_n}{2}\right)^2 + |h_n|^2} \right|. \tag{3.19}$$

It will be necessary to transform the covariance matrix Γ accordingly

$$\widetilde{\Gamma} = U\Gamma U^{\dagger}. \tag{3.20}$$

By minimizing the energy expectation value

$$\langle E\rangle = \mathrm{Tr}\big(H^T\Gamma\big) = \mathrm{Tr}\big(\widetilde{H}^{\dagger}\widetilde{\Gamma}\big) \tag{3.21}$$

we find the covariance matrix for the ground state. In the case $k_n l_n < |h_n|^2$ it is

$$\widetilde{\Gamma}^0_{mn} = \delta_{mn}\Big(\big(\tfrac{k_n-l_n}{2}\big)^2+|h_n|^2\Big)^{-1/2}\begin{pmatrix} i\frac{k_m-l_m}{2} & -h_m \\ h_m^* & -i\frac{k_m-l_m}{2}\end{pmatrix} \tag{3.22}$$

and otherwise

$$\widetilde{\Gamma}^0_{mn} = \delta_{mn}\mathrm{sign}\,(k_n+l_n)\begin{pmatrix}-i & 0\\ 0 & -i\end{pmatrix}. \tag{3.23}$$

In the case of isotropic systems along the chain $k_n = -l_n$ holds, thus $k_n l_n < |h_n|^2$ is fullfilled in such systems. Since the XY chain is isotropic, we can concentrate on the case of Eq. (3.22).

3.2.4 Jordan-Wigner Transformation

As already indicated, we can treat spin systems in the formalism of non-interacting fermions. The Jordan-Wigner transformation maps Pauli spin operators onto fermionic operators via

$$c_{k,0} = \prod_{l=1}^{k-1}\sigma_z^l\sigma_x^k,\ c_{k,1} = \prod_{l=1}^{k-1}\sigma_z^l\sigma_y^k. \tag{3.24}$$

This transformation maps some spin chains onto spinless non-interacting fermionic systems which can be solved exactly. A prominent example is the anisotropic XY chain in a transverse magnetic field [Sac99] with the Hamiltonian

$$\mathbf{H} = -J\sum_{i=1}^{N}\big[(1+\gamma)\sigma_x^i\sigma_x^{i+1} + (1-\gamma)\sigma_y^i\sigma_y^{i+1}\big] + B\sum_{i=1}^{N}\sigma_z^i, \tag{3.25}$$

where B is the magnetic field, J the ferromagnetic coupling, and γ the anisotropy parameter. This translationally invariant Hamiltonian is rep-

resented by a Hamiltonian matrix with

$$H_0 = \begin{pmatrix} 0 & -2B \\ 2B & 0 \end{pmatrix} \tag{3.26}$$

$$H_1 = \begin{pmatrix} 0 & 2J\big(1-\gamma\big) \\ -2J\big(1+\gamma\big) & 0 \end{pmatrix} \tag{3.27}$$

$$H_{-1} = \begin{pmatrix} 0 & 2J\big(1+\gamma\big) \\ -2J\big(1-\gamma\big) & 0 \end{pmatrix}. \tag{3.28}$$

After Fourier transforming (see Eq. (3.15)) this Hamiltonian matrix assumes the form given in Eq. (3.17) with

$$h_n = -2B + 4J\cos\frac{2\pi}{N}n + 4J\gamma i\sin\frac{2\pi}{N}n, \tag{3.29}$$

$$k_n = l_n = 0. \tag{3.30}$$

The energies of the elementary excitations of this Hamiltonian are $\epsilon_n = |h_n|$. A phase transition occurs iff the ground state is degenerate, i.e., an $\epsilon_n = 0$ exists. For the XY chain in Eq. (3.29) the gap closes at $B = 2J$ in the thermodynamic limit. Thus the quantum XY chains exhibit a phase transition at this point. In fact, these models constitute the archetypal example of a continuous quantum phase transition [Sac99]. In this chapter we want to find properties of the dissipative dynamics signaling this phase transition.

3.3 Exactly solvable quadratic Systems

In this section we are studying the dynamical properties of the Lindblad master equation with Hermitian Lindblad operators. First in Sec. 3.3.1 we are describing the steady states of the Lindblad master equation (3.2). We find that in our case the steady states are not interesting. Therefore, we are calculating the asymptotic decoherence rate that determines the long-time dynamics of the decoherence process in Sec. 3.3.2. We find that phase transitions of the system are reflected in this rate. We further find an agreement between the asymptotic decoherence rate and the ground state variance (see Sec. 3.3.3).

3.3.1 Steady States

Let us first determine the steady state density matrices satisfying $\partial_t \big|\rho_0\rangle = 0$. We consider all complex valued vectors $\big|\rho\rangle$ instead of just the ones corresponding to positive density matrices with trace one. Therefore, we have to check after the calculation if our results correspond to physically meaningful states.

Following Eq. (3.3) the steady states satisfy

$$\langle\rho_0\big|\big(\mathcal{H} - \frac{1}{2}\sum_\alpha \big(\mathcal{L}^\alpha\big)^2\big)\big|\rho_0\rangle = 0. \tag{3.31}$$

As found above, for Hermitian Lindblad operators $\mathbf{L}^\alpha$, $\mathcal{H}$ is anti-Hermitian and all $\big(\mathcal{L}^\alpha\big)^2$ are Hermitian. Applying these properties we can conclude from Eq. (3.31) that

$$\langle\rho_0\big|\sum_\alpha \big(\mathcal{L}^\alpha\big)^2\big|\rho_0\rangle = \langle\rho_0\big|\mathcal{H}\big|\rho_0\rangle = 0 \tag{3.32}$$

holds. It follows from the non-negativity of $\big(\mathcal{L}^\alpha\big)^2$ that

$$\big(\mathcal{L}^\alpha\big)^2\big|\rho_0\rangle = 0 \ \ \forall\alpha. \tag{3.33}$$

Because the $\mathcal{L}^\alpha$ can be diagonalized this implies $\mathcal{L}^\alpha\big|\rho_0\rangle = 0$. It follows that $\mathcal{H}\big|\rho_0\rangle$ vanishes identical. In terms of matrices ρ_0, we can summarize these conditions for steady states

$$[\mathbf{H}, \rho_0] = [\mathbf{L}^\alpha, \rho_0] = 0 \ \ \forall\alpha. \tag{3.34}$$

It can be verified with Eq. (3.2) that this condition for steady states is not only necessary but also sufficient.

We can derive the analogous condition for the steady state covariance matrix Γ_0 from Eq. (3.12)

$$[H, \Gamma_0] = [L^\alpha, \Gamma_0] = 0 \ \ \forall\alpha. \tag{3.35}$$

To summarize, steady states for Hermitian Lindblad operators correspond to density matrices commuting with the Hamiltonian and all Lindblad operators. Therefore, they are the identity up to symmetries shared by the Hamiltonian and the Lindblad operators. We are giving examples in Sec. 3.4.

Another class of density matrices are non-decaying, but oscillating density matrices $\partial_t \big|\rho_1\rangle = i\lambda \big|\rho_1\rangle$ with a real $\lambda \neq 0$. We can exclude them under the condition that the Hermitian Lindblad operators form a set of stabilizer operators, i.e. a set of commuting observables $\left[\mathbf{L}^\alpha, \mathbf{L}^\beta\right] = 0 \, \forall \alpha, \beta$, where the eigenvalues of the $\mathbf{L}^\alpha$ can distinguish between all states in the Hilbert space. We will show this in the following. Analogous to the steady states, non-decaying, but oscillating density matrices ρ_1 must satisfy

$$[\mathbf{H}, \rho_1] = \lambda \rho_1, \;\; [\mathbf{L}^\alpha, \rho_1] = 0 \;\; \forall \alpha. \tag{3.36}$$

Since ρ_1 commutes with the set of stabilizer operators $\mathbf{L}^\alpha$, ρ_1 can be diagonalized. Thus $[\rho_1, \rho_1^\dagger] = 0$ holds, in contradiction with the first condition of Eq. (3.36) for $\rho_1 \neq 0$:

$$0 = \mathrm{Tr}\left(\mathbf{H}\left[\rho_1, \rho_1^\dagger\right]\right) = \mathrm{Tr}\left(\rho_1^\dagger \left[\mathbf{H}, \rho_1\right]\right) = \lambda \mathrm{Tr}\left(\rho_1 \rho_1^\dagger\right) \neq 0. \tag{3.37}$$

Therefore, $\lambda = 0$ must be fulfilled and all non-decaying states are steady states.

3.3.2 Asymptotic Decoherence Rate

In the previous section we found that steady states are trivial for Hermitian Lindblad operators. Thus, we concentrate on the asymptotics of the decoherence process in the following. It is studied through the eigenvalues λ_i of the superoperator S (see Eq. (3.13))

$$S\big|\Gamma\rangle = \lambda_i \big|\Gamma\rangle. \tag{3.38}$$

Those eigenvalues whose real parts are closest to zero $\Re\big(\lambda_i\big) \sim 0$ determine the asymptotics of the decoherence dynamics. The real parts of λ_i are non-positive. The eigenvalue with the smallest absolute nonzero real part, denoted μ, determines the asymptotic dynamics

$$\Gamma\left(t\right) = e^{St}\Gamma\left(t\right) \xrightarrow{t\to\infty} \Gamma(\infty) + e^{\mu t}\Gamma_\mu. \tag{3.39}$$

Now we are calculating the asymptotic decoherence rate μ in the limit of small couplings to the environment. We focus on the N Lindblad operators

$$\mathbf{L}^\alpha = l \cdot \sigma_z^\alpha = l \cdot \frac{i}{2}\left[c_{\alpha,1}, c_{\alpha,0}\right] \tag{3.40}$$

in the limit $l \to 0$. In this case the Lindblad equation (3.12) becomes

$$\partial_t \Gamma_{kl,mn} = \frac{1}{\hbar} [H, \Gamma]_{kl,mn} - 4l^2 \Gamma_{kl,mn} (1 - \delta_{kl}), \tag{3.41}$$

where we have exploited the anti-symmetry of the the covariance matrix. For translationally invariant (see Sec. 3.2.3) systems we can write this equation in Fourier space for $\widetilde{\Gamma}$

$$\partial_t \widetilde{\Gamma}_{kl} = \frac{1}{\hbar} \big[\widetilde{H}, \widetilde{\Gamma}\big]_{kl} - 4l^2 \left(\widetilde{\Gamma}_{kl} - \frac{1}{N} \sum_{r,s=1}^{N} \widetilde{\Gamma}_{rs} \delta_{r-s,k-l} \right), \tag{3.42}$$

This corresponds to the unitary transformation of the superoperator $\mathcal{S}$

$$\widetilde{\mathcal{S}} = \big(U \otimes U\big) \mathcal{S} \big(U \otimes U\big)^\dagger \tag{3.43}$$

with U from Eq. (3.15) and does not change its eigenvalues. For weak couplings between system and bath $l \to 0$, the eigenvalues of S can be determined by first order perturbation expansion. To this end we first diagonalize the unperturbed unitary part of S

$$\big[\widetilde{H}, \widetilde{\Gamma}\big]_{kl} = \widetilde{H}_{kk} \widetilde{\Gamma}_{kl} - \widetilde{\Gamma}_{kl} \widetilde{H}_{ll} = \lambda \widetilde{\Gamma}_{kl}, \tag{3.44}$$

where we will use the notation introduced in Eq. 3.16 for the Hamiltonian $\widetilde{H}$. The $4N^2$ eigenvalues λ^{mnk} $(m, n = 1, \ldots, N,\ k = 1, \ldots, 4)$ are

$$\lambda^{mn1} = i\,(\alpha_m - \alpha_n + \beta_m - \beta_n) \tag{3.45}$$
$$\lambda^{mn2} = i\,(\alpha_m - \alpha_n - \beta_m + \beta_n) \tag{3.46}$$
$$\lambda^{mn3} = i\,(\alpha_m - \alpha_n + \beta_m + \beta_n) \tag{3.47}$$
$$\lambda^{mn4} = i\,(\alpha_m - \alpha_n - \beta_m - \beta_n) \tag{3.48}$$

with

$$\alpha_m = |k_m + l_m|/2, \tag{3.49}$$
$$\beta_m = \sqrt{|h_m|^2 + (k_m - l_m)^2/4}. \tag{3.50}$$

The corresponding eigenmatrices are denoted as $\widetilde{\Lambda}^{mni}$ with nonzero elements $\widetilde{\Lambda}^{mni}_{kl}$ only for $m = k$ and $n = l$, i.e., $\widetilde{\Lambda}^{mni}_{kl} = \delta_{mk}\delta_{nl}\widetilde{\Lambda}^{mni}_{mn}$. Perturbation theory demands to calculate the matrix elements of the perturbative

part of S, $-4l^2(\delta_{mk}\delta_{nl}\delta_{ij} - P^{mni}_{klj}/N)$ (see Eq. (3.42)), with

$$\begin{aligned} P^{mni}_{klj} &= \frac{N}{4l^2}\langle\widetilde{\Lambda}^{mni}\big|\frac{1}{2}\sum_{\alpha}\big(\mathcal{L}^{\alpha}\big)^2\big|\widetilde{\Lambda}^{klj}\rangle + N\delta_{mk}\delta_{nl}\delta_{ij} \\ &= \sum_{r,s,t,u=1}^{N}\delta_{r-s,t-u}\mathrm{Tr}\left(\big(\widetilde{\Lambda}^{mni}_{tu}\big)^{\dagger}\widetilde{\Lambda}^{klj}_{rs}\right) \\ &= \delta_{m-n,k-l}\mathrm{Tr}\left(\big(\widetilde{\Lambda}^{mni}_{mn}\big)^{\dagger}\widetilde{\Lambda}^{klj}_{kl}\right). \end{aligned} \tag{3.51}$$

The largest eigenvalue with $\mu < N$ of the Hermitian matrix P restricted to the spaces of degenerate eigenvalues λ_{mni}, called μ_P, determines the asymptotic decoherence rate $\mu = -4l^2\big(1 - \frac{\mu_p}{N}\big)$. Because $|\mu|$ should be as small as possible, we must find eigenvalues μ_P of the order of the system size N. The matrix elements of P fulfill $\big|P^{mni}_{klj}\big| \leq 1$. Thus an N-fold degeneracy of λ^{mni} is required, which is in general possible only for $\lambda^{mni} = 0$, i.e., $m = n$ and $i = 1, 2$. The corresponding eigenmatrices are

$$\widetilde{\Lambda}^{mm1}_{kl} = \delta_{mk}\delta_{ml}\frac{1}{\sqrt{2}\beta_n}\begin{pmatrix} i\frac{k_m - l_m}{2} & -h_m \\ h^*_m & -i\frac{k_m - l_m}{2}\end{pmatrix}, \tag{3.52}$$

$$\widetilde{\Lambda}^{mm2}_{kl} = \delta_{mk}\delta_{ml}\frac{1}{\sqrt{2}}\begin{pmatrix} 1 & 0 \\ 0 & 1\end{pmatrix}. \tag{3.53}$$

As the eigenmatrices $\widetilde{\Lambda}^{mm2}$ give eigenvalues equal to N and 0 only and $P^{mn2}_{kl1} = 0$, we focus on the matrices $\widetilde{\Lambda}^{mm1}$. The corresponding part of the perturbation matrix is

$$P_{mn} = P^{mm1}_{nn1} = \frac{2h_m h^*_n + 2h^*_m h_n - \big(k_m - l_m\big)\big(k_n - l_n\big)}{4\beta_m\beta_n}. \tag{3.54}$$

We diagonalize this matrix by introducing the three vectors $\big|a\rangle, \big|b\rangle, \big|c\rangle$ with the components

$$a_m = \frac{k_m - l_m}{2\beta_m},\ b_m = \frac{\Im\big(h_m\big)}{\beta_m},\ c_m = \frac{\Re\big(h_m\big)}{\beta_m} \tag{3.55}$$

and writing P_{mn} in terms of these unnormalized vectors

$$P = \big|c\rangle\langle c\big| + \big|b\rangle\langle b\big| - \big|a\rangle\langle a\big|. \tag{3.56}$$

We now exploit the symmetries of h_n, k_n, and l_n stated in Eq. (3.18). First we observe that $\big|c\rangle$ is orthogonal to $\big|a\rangle$ and $\big|b\rangle$. We have chosen the

covariance matrices corresponding to the three vectors (3.55) to be anti-Hermitian. After transforming back into real space the ones corresponding to $\big|a\rangle$ and $\big|b\rangle$ are purely imaginary so that they have no overlap with any physically meaningful real and anti-symmetric covariance matrix. Only the matrix corresponding to $\big|c\rangle$ is real and anti-symmetric

$$\Gamma_\mu = \left(\sum_{m=1}^{N} \frac{|h_m|^2}{2\beta_m^2}\right)^{-1} \sum_n \frac{\Re\big(h_n\big)}{\beta_n} U^\dagger \Lambda^{nn1} U. \tag{3.57}$$

Therefore, it determines the asymptotic decoherence rate. We get

$$\mu_P = \sum_{m=1}^{N} \frac{\Re\big(h_m\big)^2}{\beta_m^2} = \sum_{m=1}^{N} \frac{\Re\big(h_m\big)^2}{|h_m|^2 + (k_m - l_m)^2/4} \tag{3.58}$$

or

$$\mu = -\frac{4l^2}{N} \sum_{m=1}^{N} \frac{4\Im\big(h_m\big)^2 + (k_m - l_m)^2}{4|h_m|^2 + (k_m - l_m)^2}. \tag{3.59}$$

as the general from of the asymptotic decoherence rate.

Based on this result we can now argue why μ is likely to undergo a phase transition at critical points of the system in the special case of an isotropic system $k_n + l_n = 0$ (see Eq. (3.23)). In the thermodynamic limit, the sum in Eq. (3.59) can be replaced by a loop integral around the origin of the complex plane with radius one, where the integration variable is $z = \exp\big(\frac{2\pi i}{N} n\big)$. This is possible because h_n, k_n, and l_n are results of a Fourier series. For local interactions, the denominator of the integrand is a polynomial in z and thus has a finite number of distinct roots. Applying the residue theorem, a non-continuity in μ is possible iff a residue of the integrand, i.e., a root of its denominator, moves through the integral contour in the complex plane as a function of some external parameters. This happens if $\epsilon_n^2 = |h_n|^2 + (k_n - l_n)^2/4 = 0$ (see Eq. (3.19)) for some real $n \in [0, N)$. Since a vanishing energy gap $\epsilon_n = 0$ is a signature of a quantum phase transition, we expect to observe a non-analytic behavior in the decoherence rate μ if the system is tuned through a quantum phase transition.

3.3.3 Ground State Variance

In this section we show that the asymptotic decoherence rate μ is related to the variance of the Lindblad operator in the ground state of the system.

We focus on the special case $k_n l_n < |h_n|^2 \ \forall n$, which includes the isotropic case $k_n + l_n = 0$. The system ground state is given in Eq. (3.22). The variance of the Lindblad operators $\mathbf{L}^\alpha = l\sigma_z^\alpha$ is defined as

$$\frac{\text{var}}{l^2} = \frac{\langle \big(\sum_{\alpha=1}^N \sigma_z^\alpha \big)^2 \rangle - \langle \sum_{\alpha=1}^N \sigma_z^\alpha \rangle^2}{N} \tag{3.60}$$

$$= \sum_{r=0}^{N-1} \langle \sigma_z^0 \sigma_z^r \rangle - N \langle \sigma_z^0 \rangle^2, \tag{3.61}$$

where the second equality holds for translationally invariant states. The quantity $\langle \sigma_z^0 \rangle$ is contained in the covariance matrix, the higher order correlations are evaluated with Wick's theorem [Wic50]

$$\langle \sigma_z^0 \sigma_z^r \rangle = -\langle c_{0,1} c_{0,0} c_{r,1} c_{r,0} \rangle \tag{3.62}$$

$$= \begin{cases} 1 & r = 0 \\ \text{Pf}\left(\Gamma^0 |_{(0,1),(0,0),(r,1),(r,0)} \right) & r \geq 1. \end{cases} \tag{3.63}$$

In this case the Pfaffian is given by

$$\text{Pf}\left(\Gamma^0 |_{(0,1),(0,0),(r,1),(r,0)} \right) = \Gamma^0_{00,10}\Gamma^0_{rr,10} - \Gamma^0_{0r,11}\Gamma^0_{0r,00} + \Gamma^0_{0r,10}\Gamma^0_{0r,01}. \tag{3.64}$$

The variance assumes the form

$$\text{var} = -\frac{\mu}{2} = \frac{2l^2}{N} \sum_{m=1}^N \frac{4\Im\big(h_m\big)^2 + (k_m - l_m)^2}{4|h_m|^2 + (k_m - l_m)^2} \tag{3.65}$$

and equals the negative asymptotic decoherence rate μ (see Eq. (3.59)) up to the factor 2.

This equality between the variance of the Lindblad operator in the system ground state and the asymptotic decoherence rate can be made plausible by viewing the dissipation due to the Lindblad master equation as a constant measurement of the system in the Lindblad operator basis. If the system prefers states with a small variance of the Lindblad operators, these measurements do not affect the system and the decoherence rate is small. If this variance is large, however, a measurement in the Lindblad operator basis changes the state of the system significantly and the decoherence rate is large.

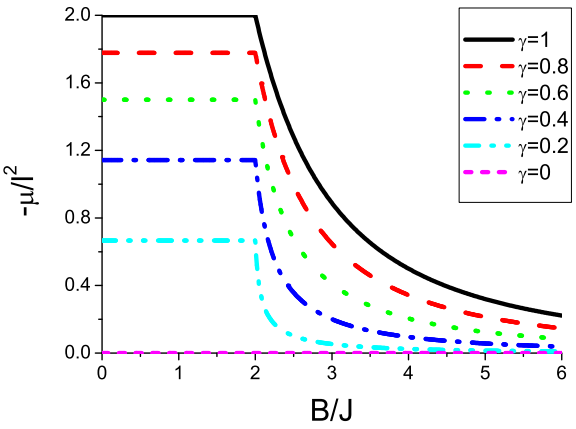

Figure 3.1: Asymptotic decoherence rate μ (see Eq. (3.59) of the XY chain (3.25) for different anisotropy parameters γ as a function of the magnetic field in the limits $N \to \infty$ and $l \to 0$. A phase transition in μ is visible at $B = 2J$ for $\gamma \neq 0$.

3.4 Quantum XY Chain

We will now apply the results of the previous Sec. 3.3 to the example of the anisotropic XY chain in a transverse magnetic field. After a brief discussion of the steady states and a derivation of the asymptotic decoherence rate in the thermodynamic limit ($N \to \infty$) and in the limit of weak system bath couplings $l \to 0$ (see Sec. 3.4.1), we will present numerical results of the system dynamics for finite N and l and compare them with our analytic predictions (see Sec. 3.4.2).

3.4.1 Analytical Results

The anisotropic XY chain in a transverse magnetic field given by the Hamiltonian (3.25) is introduced in Sec. 3.2.4. These models are translationally invariant and isotropic, i.e., described with $k_n = -l_n$ (see Eq. (3.17)). We focus on the Lindblad operators $\mathbf{L}^\alpha = l\sigma_z^\alpha$ and can apply all results from Sec. 3.3 to this example.

First, we discuss the steady states of these systems (see Sec. 3.3.1). From Eq. (3.34) we have concluded that the steady state density matrix is the identity up to symmetries shared by the Lindblad operators and the

Hamiltonian. A rigorous derivation of the steady states for this example could start from the Ansatz that the steady state density matrix is diagonal in the Fock basis, following from $\left[\sigma_z^\alpha, \rho\right] = 0$. Then the commutator $\left[\mathbf{H}, \rho\right] = 0$ must be exploited to get the steady state.

As the Lindblad operators correspond to local particle number operators, the important compatible symmetries for the XY chains are the parity $\mathcal{P} = \sigma_z^1 \dots \sigma_z^N$, discriminating between an odd and an even number of particles, and the total particle number $\mathcal{N} = \left(\mathbf{1} + \sum \sigma_z^i\right)/2$. For truly asymmetric XY chains $\gamma \neq 0.5$ the parity is the highest symmetry compatible with the Lindblad operators. In these cases the steady state density matrix is given by the identity in the two sectors of even and odd parity, the relative weight of these sectors is determined by the initial state. For the symmetric chain $\gamma = 0.5$, the steady state density matrix is the identity only in the sectors with a constant total number of particles. Thus for $\gamma \neq 0.5$ the steady state magnetization is $\langle \sigma_z^i \rangle = 0$ regardless of the initial state, whereas the magnetization of the initial state is conserved for $\gamma = 0.5$.

Second, we calculate the asymptotic decoherence rate (3.59) for the XY chains with Eq. (3.29). For $\gamma = 0$ we get $\mu = 0$ easily. For $\gamma \neq 0$ we will reformulate the sum in (3.59), and evaluate it in the thermodynamic limit by transforming it into a contour integral and applying the residue theorem. We reformulate Eq. (3.59)

$$\mu = -\frac{4l^2}{N} \sum_{m=1}^{N} \frac{\Im\left(h_m\right)^2}{|h_m|^2} = -2l^2\left(1 - \frac{1}{N} \sum_{m=1}^{N} \frac{h_m}{h_m^*}\right) \tag{3.66}$$

and evaluate the sum $1/N \cdot \sum_{m=1}^{N} h_m/h_m^*$ in the thermodynamic limit by introducing the complex variable $z = \exp\left(2\pi i m/N\right)$

$$\lim_{N\to\infty} \frac{1}{N} \sum_{m=1}^{N} \frac{h_m}{h_m^*} = \frac{1}{2\pi i} \oint_{|z|=1} \frac{dz}{z} \frac{2J\left(1-\gamma\right)z^2 - 2Bz + 2J\left(1+\gamma\right)}{2J\left(1+\gamma\right)z^2 - 2Bz + 2J\left(1-\gamma\right)} \tag{3.67}$$

where the integration contour is a circle of radius $|z| = 1$ around $z = 0$ in the complex plane. The complex integrand is analytic except for three distinct poles at

$$\begin{aligned} z^0 &= 0, \\ z^\pm &= \frac{1}{2J\left(1+\gamma\right)} \left(B \pm \sqrt{B^2 - 4J^2\left(1-\gamma^2\right)}\right). \end{aligned} \tag{3.68}$$

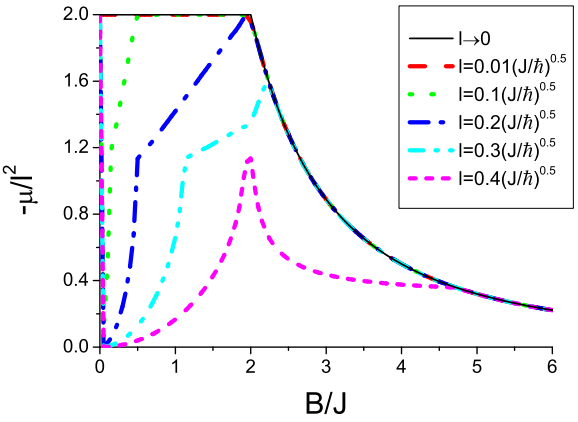

Figure 3.2: Asymptotic decoherence rate μ (see Eq. (3.59)) of the XY chain (3.25) for different coupling strengths l, $\gamma = 1$, and $N = 100$ as a function of the magnetic field B. For $l \leq 0.1\,(J/\hbar)^{0.5}$ the results agree with the limit of weak coupling $l \to 0$ (see Eq. (3.69))

.

The contour integral is determined by the sum over the residues at those poles which are inside the contour ($|z| < 1$). z^0 is always inside this contour. In the case $\gamma > 0$, z^+ is inside the contour for $B < 2J$ and outside for $B > 2J$, while z^- is always inside the contour. In the case $\gamma < 0$, z^- is inside the contour for $B > 2J$ and outside for $B < 2J$, while z^+ is always outside the contour. So residues cross the contour at the quantum phase transition $B = 2J$ (because then $h_n = 0$ for some n), leading to a non analytical behavior in the asymptotic decoherence rate.

After applying the residue theorem we get the asymptotic decoherence rate

$$\mu = -4l^2 \cdot \begin{cases} \frac{|\gamma|}{1+|\gamma|} & B \leq 2J \\ \frac{\gamma^2}{1-\gamma^2}\left(\frac{1}{\sqrt{1-\left(\frac{2J}{B}\right)^2(1-\gamma^2)}} - 1\right) & B \geq 2J \end{cases} \tag{3.69}$$

for all γ. It does not depend on the sign of γ and is shown in Fig. 3.1 for several values of $\gamma \in [0, 1]$. For $B < 2J$ the asymptotic decoherence rate does not vary with the magnetic field, while its magnitude decays to zero for large magnetic fields like $\sim \left(J/B\right)^2$. The same behavior was found for the variance of the particle number in these models in a previous work [BSS+08]. To summarize, the asymptotic decoherence rate undergoes a

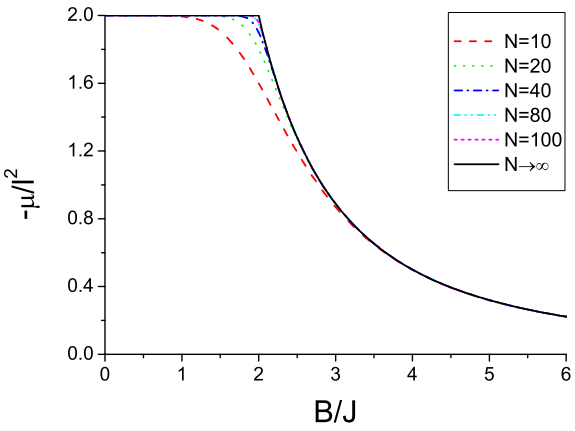

Figure 3.3: Asymptotic decoherence rate μ (see Eq. (3.59)) of the XY chain (3.25) for different system sizes N and $\gamma = 1$, $l = 0.01\,(J/\hbar)^{0.5}$ as a function of the magnetic field B. For $N \geq 50$ the thermodynamic limit is reached except for small variations at the phase transition $B = 2J$.

dissipative phase transition at $B = 2J$ signaling the phase transition in the system.

3.4.2 Numerical Simulations

The final result for the asymptotic decoherence rate (3.69) is valid in the limits $N \to \infty$ and $l \to 0$. In this section we perform a numerical diagonalization of the Lindblad master equation superoperators S to compare the analytic result with the values for finite N and l. Furthermore, we extract the asymptotic decoherence rate from a simulation of the system dynamics and compare it with our prediction.

In Fig. 3.2 we present the asymptotic decoherence rate for finite coupling strengths l. For $l^2 \leq 0.01 J/\hbar$ the result of perturbation theory is in excellent agreement with the numerical diagonalization of the Lindblad master equation superoperator. Deviations are strongest at small magnetic fields. We show the asymptotic decoherence rate μ for different finite system sizes in Fig. 3.3. Even in small systems with $N = 10$ spins the same qualitative behavior is found as in thermodynamic limit, i.e., the asymptotic decoherence rate signals the quantum phase transition in the system at $B = 2J$. However, finite values of l and N lead to a smearing

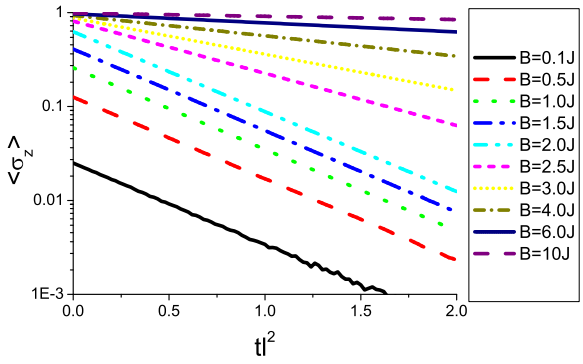

Figure 3.4: Evolution of the magnetization $\langle \sigma_z^i \rangle$ in time starting from the system ground state of the XY chain (3.25), for different magnetic fields B, $l = 0.01\,(J/\hbar)^{0.5}$, and $\gamma = 1$. The magnetization decreases exponentially in time.

out of the phase transition.

We have defined the asymptotic decoherence rate through a diagonalization of the master equation, trying to describe the long-time dynamics of the system. To demonstrate the deep relation between μ and the dissipative dynamics, we extract the decoherence rate from a dynamical calculation (see Fig. 3.4). Here we start from the ground state of the system and study the decay of the magnetization in time after the system is brought into contact with a Markovian bath. In this example the exponential decay expected after long evolution times is nicely visible. In Fig. 3.5 we compare the extracted decay rates for different magnetic fields with the result of the diagonalization. We find an exact agreement with the asymptotic decay rate numerically calculated with the same finite parameters.

3.5 Non-exactly solvable System

For general Lindblad operators the dynamics determined by the Lindblad master equation (3.1) cannot be solved exactly. In this section we are studying, as an example for such a case, the dynamics of the Ising chain (see Eq. (3.25) with $\gamma = 1$) coupled to a Markovian bath with the non-Hermitian Lindblad operators $\mathbf{L}^\alpha = l\sigma_+^\alpha$ in the limit of small couplings to

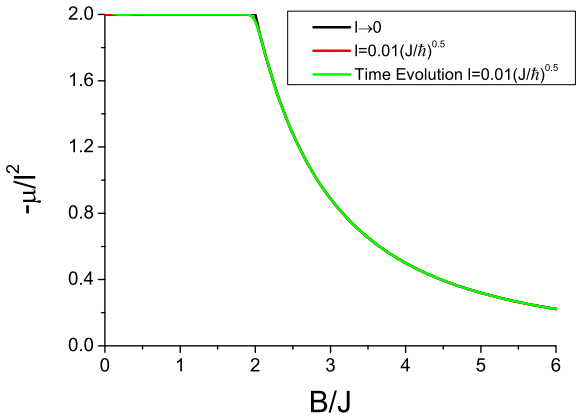

Figure 3.5: The asymptotic decoherence rates μ (see Eq. (3.59)) of the XY chain (3.25) for $\gamma = 1$ for $l = 0.01\,(J/\hbar)^{0.5}$ and $l \to 0$ (result of perturbation theory) as a function of the magnetic field B are compared with the late-time decoherence rates extracted from Fig. 3.4. The agreement between the asymptotic decoherence rate and the late-time decoherence rate shows the validity of our calculations for finite times.

the environment $l \to 0$. We try to show that also in this case the quantum phase transition in the Ising chain is reflected in the decoherence dynamics. Since the asymptotic decoherence rate is found to be constant, we analyze the steady states of the decoherent dynamics.

In this case we have to resort to exact numerical methods. Matrix Product States (MPS) are ideally suited for the study of one-dimensional spin systems. Their extension to Matrix product operators (MPO) allows to solve for the decoherence dynamics of a system [VGC04]. In recent works MPOs have been used to solve the Lindblad master equation for quadratic spin systems with linear Lindblad operators in the Heisenberg picture [PZ05, CPH+10]. Here we calculate the steady state of the dynamics of the open Ising chain in the Schrödinger picture in two steps. First we perform a real time evolution starting from the Hamiltonian ground state, second we find the kernel of the time evolution superoperator $\mathcal{S}$ (see Eq. (3.3)) through a minimization of the functional

$$E(\rho) = \frac{\langle\rho|\mathcal{S}^\dagger\mathcal{S}|\rho\rangle}{\langle\rho|\rho\rangle}. \tag{3.70}$$

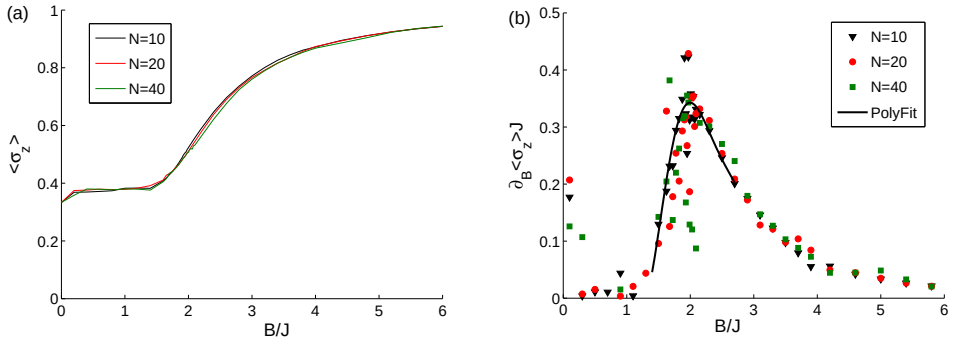

Figure 3.6: (a) Magnetization $\langle\sigma_z^i\rangle$ and (b) its derivative $\partial_B\langle\sigma_z^i\rangle$ of the steady state of the XY chain (3.25) for $\gamma = 1$ coupled to a Markovian bath with Lindblad operators $\mathbf{L}^\alpha = l\sigma_+^\alpha$ and $l^2 = 0.01J/\hbar$ as a function of the magnetic field B for different system sizes N (result of MPO simulation). The curve in (b) is a polynomial fit to the simulation results for $N = 10$ around $B = 2J$. The peak in $\partial_B\langle\sigma_z^i\rangle$ at the quantum phase transition at $B = 2J$ signals the presence of a dissipative phase transition.

In order to detect the continuous dissipative phase transition we calculate the derivative of the magnetization $\partial_B\langle\sigma_z^i\rangle$ with respect to the magnetic field B. The accuracy of our numerical simulation close to the phase transition is limited, especially the numerical derivative is inaccurate. We have checked the validity of our approach by comparing with exact calculations for small chains $N \leq 10$.

The result of this simulation is depicted in Fig. 3.6. A peak in $\partial_B\langle\sigma_z^i\rangle$ seems to signal the dissipative quantum phase transition we expect. Nevertheless, further numerical studies seem necessary to confirm this statement [HC11].

3.6 Experimental Realization

We now discuss an experiment suited for the measurement of the asymptotic decoherence rate in spin systems. The quantum simulation of spin systems with trapped ions was proposed in [PC04], where the spin degree of freedom is represented by two hyperfine levels. The magnetic field can be simulated either by directly driving Rabi oscillations of the hyperfine transition or with space-independent Raman transitions induced by suitably aligned lasers. The spin-spin interaction is mediated via motional

degrees of freedoms. State-dependent optical dipole forces (compare with state-dependent optical lattices) are generated by coupling the two hyperfine levels to electronically excited states with off-resonant laser beams. These dipole forces change the distance and consequently the Coulomb repulsion between two ions dependent on their internal states. This state-dependent Coulomb repulsion can be designed to give the required spin-spin interaction. The spin state can be measured by fluorescence imaging of the ions.

In this way the quantum Ising chain [FSG$^+$08, SFS$^+$09] and frustrated Ising models [KCK$^+$10] have been realized in recent experiments. In these experiments the ions were first cooled to their zero-point motional ground state and optically pumped into a certain spin configuration. The initial state represents the ground state of the system without spin-spin interactions. Then the spin-spin interactions are adiabatically increased such that the system undergoes a phase transition. Finally, it is checked that the final states represents the ground state of the simulated Hamiltonian.

We propose to extend this quantum simulation by adding an incoherent evolution. The Lindblad master equation (3.1) with Hermitian Lindblad operators $\mathbf{L}^\alpha = l\sigma_z^\alpha$ (see Sec. 3.3) can be realized by introducing fluctuations of the simulated magnetic field $B^\alpha(t) = B^\alpha + \delta B^\alpha(t)$ [MP08] as shown in the following. The local magnetic fields $\delta B^\alpha(t)$ should be uncorrelated between different sites $\overline{\delta B^\alpha(t_1)\delta B^\beta(t_2)} = \delta_{\alpha\beta}\overline{\delta B^\alpha(t_1)\delta B^\alpha(t_2)}$. We restrict our derivation to a single Lindblad operator without loss of generality. Let, for example, $\delta B(t)$ constitute a Gaussian stochastic process of zero mean $\overline{\delta B(t)} = 0$ with the time-correlations

$$\overline{\delta B(t_1)\delta B(t_2)} = \begin{cases} \overline{\delta B^2} & \text{for } |t_1 - t_2| \leq T \\ 0 & \text{for } |t_1 - t_2| > T. \end{cases} \tag{3.71}$$

The correlation time T has to be much shorter than every process in the system (Markovian limit), i.e., $|\mathcal{H}|T < \omega T \ll 1$, with the spectral width ω and the superoperator $\mathcal{H}$ from Eq. (3.4). The averaged density matrix evolves like $\big|\rho(t)\rangle\rangle = \overline{\mathcal{U}(t)}\big|\rho(0)\rangle\rangle$, where the bar denotes the statistical average over the fluctuating magnetic field. The time evolution operator $\overline{\mathcal{U}(t)}$ consists of contributions from $\mathcal{H}$ and

$$\mathcal{V}(t) = i\frac{\delta B(t)}{\hbar}\mathcal{V} = -\frac{i}{\hbar}\left(\mathbf{V}(t)\otimes\mathbf{1} - 1\otimes\mathbf{V}^{\mathrm{T}}(t)\right). \tag{3.72}$$

with $\mathbf{V} = \sigma_z$. We can evaluate the statistical average of the time evolution

operator in the interaction picture for the superoperators

$$\begin{aligned}
\overline{\mathcal{U}(t)} &= e^{\mathcal{H}t}\overline{\mathcal{T}\exp\left(\int_0^t d\tau e^{-\mathcal{H}\tau}\mathcal{V}(\tau)e^{\mathcal{H}\tau}\right)} \\
&= e^{\mathcal{H}t}\sum_{n=0}^{\infty}\overline{\int_{t\geq t_1\geq\cdots\geq t_n\geq 0} dt_1\ldots dt_n e^{-\mathcal{H}t_1}\mathcal{V}(t_1)e^{\mathcal{H}t_1}\cdots e^{-\mathcal{H}t_n}\mathcal{V}(t_n)e^{\mathcal{H}t_n}} \\
&= e^{\mathcal{H}t}\sum_{m=0}^{\infty}\left(-\frac{\overline{\delta B^2}}{\hbar^2}\cdot\frac{T}{2}\right)^m\cdot \\
&\qquad\qquad \int_{t\geq t_1\geq\cdots\geq t_m\geq 0} dt_1\ldots dt_m e^{-\mathcal{H}t_1}\mathcal{V}^2 e^{\mathcal{H}t_1}\cdots e^{-\mathcal{H}t_m}\mathcal{V}^2 e^{\mathcal{H}t_m} \\
\overline{\mathcal{U}(t)} &= \exp\left(\mathcal{H}t - \frac{1}{2}\frac{\overline{\delta B^2}T}{\hbar^2}\mathcal{V}^2 t\right)
\end{aligned} \tag{3.73}$$

with the time ordering operator $\mathcal{T}$. Between the second and the third line, we keep only even summation indices $m = 2n$ (zero mean Gaussian process), evaluate the statistical average at adjacent times $t_{2n-1} - t_{2n} \leq T$ (correlation time T), and neglect the terms $\exp(\mathcal{H}(t_{2n-1} - t_{2n})) \ll 1$ (Markovian limit). In summary, we have shown that the described fluctuations of the magnetic field generate Markovian dynamics (see Eq. (3.3)) with Lindblad operators $\mathbf{L}^\alpha = l\sigma_z^\alpha = l\mathbf{V}$ and decoherence strength

$$l^2 = \frac{\overline{\delta B^2}T}{\hbar^2}. \tag{3.74}$$

In the case of the anisotropic XY chain (see Eq. (3.25)), the correlation time T is bounded by the width of the single particle excitation spectrum $T^{-1} \gg \max(4B/\hbar, 8J/\hbar)$. In the recent experiment [FSG+08] $2J/\hbar \approx B/\hbar = 2\pi\times 4.4kHz$ was used, but experimentally available laser intensities allow $2J/\hbar \approx B/\hbar \approx 2\pi \times 40kHz$. We propose to create fluctuations of the magnetic field with frequency $T^{-1} = 2\pi \times 1.6MHz$ and variance $\overline{\delta B^2}/\hbar^2 = (0.2B/\hbar)^2 \approx (2\pi\times 8kHz)^2$. This would result in the decoherence strength $l^2 \approx 2\cdot 10^{-3}J/\hbar$ and would require coherence times of order $2\pi/l^2 \approx 25ms$. These coherence times can in principle be achieved in systems of trapped ions [WMI+98].

3.7 Conclusion

To conclude, in this chapter we have analyzed the decoherence dynamics of a system exhibiting a quantum phase transition. We concentrated our analysis on spin system which can be transformed into non-interacting fermionic systems via the Jordan-Wigner transformation. An important example in this class of Hamiltonians is the anisotropic XY chain with a transverse magnetic field containing a continuous phase transition.

The covariance matrix formalism is known to give an exact solution for the unitary dynamics of such spin chains. We treat the decoherence in the framework of the Lindblad master equation valid for Markovian baths. Here we have extended this formalism to get an exact treatment of the Lindblad master equation (see Sec. 3.2).

This method allowed us to find that a quantum phase transition in a system in contact with a Markovian bath leads to a dissipative phase transition, i.e., a transition in the decoherence properties. We observe a dissipative phase transition in the asymptotic decoherence rate for quadratic Lindblad operators (see Sec. 3.3) and in the steady state for an example of non-quadratic Lindblad operators (see Sec. 3.5). Numerical calculations show that our results are approximately valid also for finite systems and finite decoherence strengths (see Sec. 3.4).

We have proposed an experimental realization of this quantum simulation with trapped ions (see Sec. 3.6). We expect the engineering of decoherence to be a valuable tool for future quantum simulators, quantum memories, quantum communicators, and quantum computers. With this work we suggest the possibility of detecting certain system properties through an observation of the decoherent dynamics.

Chapter 4

Hawking Radiation

4.1 Introduction

In 1974 Hawking showed that the theory of quantum fields (QFT) in curved spacetime predicts that, surprisingly, black holes emit thermal radiation [Haw74]. Unfortunately, the temperature of this radiation is too small to be detected for typical astrophysical black holes. Furthermore, the original theoretical derivation suffers from the problem that the wave equation is assumed to be valid on all scales, whereas QFT in curved space is reliable just up to the Planck energy. Unruh showed that the Hawking effect is also manifested in analogous hydrodynamical systems which have a region of supersonic flow and hence a sonic horizon [Unr81]. Such analogous systems offer great advantages, since the effect can potentially be accessible to experiments. Moreover, its robustness can be proven based on the well known microphysics of the hydrodynamical systems. This will contribute to deepen our understanding of the Hawking effect also in gravitational black holes.

In recent years many experimental tests of Hawking radiation have been proposed based on this hydrodynamical analogy [BLV05], e.g., phonons in Bose-Einstein condensates (BECs) [GAC$^+$00, GAC$^+$01, FF03, BFF$^+$08, CFR$^+$08, MP09a], ultracold Fermi gases [Gio05], superfluid Helium [JV98], slow light [LP00, Rez00, US03], and nonlinear electromagnetic waveguides [SU05]. Some analog spacetimes have been experimentally implemented, e.g., in BECs [LIB$^+$10], in optical fibres [PKR$^+$08], and on water surfaces [RMM$^+$08, WTP$^+$11]. Common to all these attempts is that they have not reported on the observation of the quantum

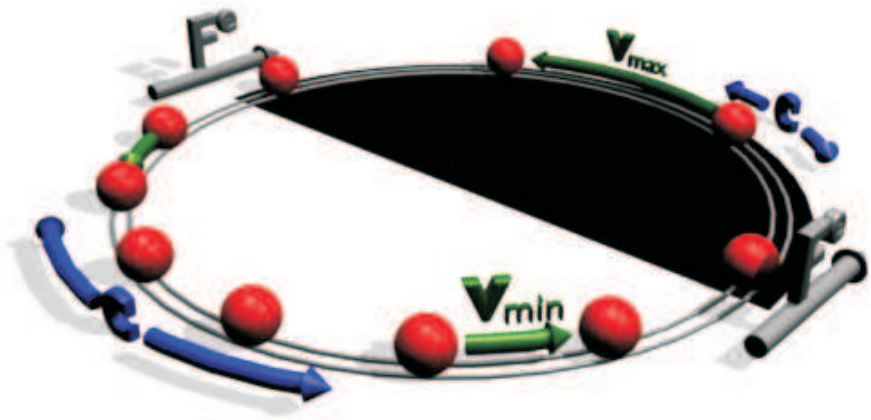

Figure 4.1: Schematic depiction of the ion rotation with velocity $v(\theta)$ and the phononic excitations with velocity $\pm c(\theta)$, that depend on the varying ion spacing. In the subsonic region the ion velocity is $v(\theta) = v_{\min}$, in the supersonic region it is $v(\theta) = v_{\max}$. The external force $F^{\mathrm{e}}(\theta)$ localized at the transition between the super- and subsonic region (de-) accelerates the ions. The black area represents the supersonic black hole region. (Online only) Clicking on the figure opens a movie displaying the equilibrium motion of the ions.

Hawking effect. The observation of the quantum Hawking effect has been claimed in [BCC$^+$10] for ultrashort laser pulses in nonlinear optical media. But pair emission of and entanglement between Hawking particles has not been observed in this setup.

In the present work we discuss a proposal how to build an analog model of a black hole in an experimentally realizable system of cold ions trapped on a ring by electrodynamic forces [HRF$^+$10, HSR$^+$11]. A special ingredient of our proposal is its discreteness, which naturally leads to a sublinear dispersion relation at high wavenumbers. This affects the trajectories of blue shifted waves close to the event horizon [Jac91]. The dispersion relation is, additionally, non-trivial at low wavenumbers because of the long range Coulomb force. However, as we will show, we still obtain Hawking radiation. Analytic derivations [Jac91, CJ98, JM99, US05, Cor98, BMP$^+$95, HT00, SS00, SU08] as well as numerical calculations show that the Hawking effect is robust against such short scale modifications, e.g., for a continuous field with a sublinear dispersion relation [Unr95] and a

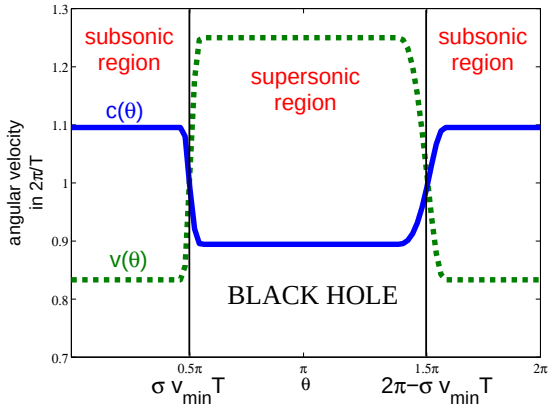

Figure 4.2: Typical profiles of the ion (v, green) and the sound velocity (c, blue) used in this chapter (see Appendix A.2). The profile shows a super- and a subsonic region. The ion velocity in the subsonic region is $v_{\min} = 2\pi \times 0.8\bar{3}/T$ and the black hole horizon is located at $\sigma v_{\min} T = 2\pi \times 0.25$. A white hole horizon is also present on the ring [HRF+10].

discretized field on a falling lattice [CJ98, JM99]. Our proposal uses a parameter regime which is accessible in experiments at temperatures currently achieved. Thus, it could lead to the experimental observation of Hawking radiation.

Let us now summarize the main idea of our proposal. We are constructing a discrete analog of an hydrodynamical system with super- and subsonic regions in a quadrupole ring trap [DP64, BKW92] as schematically depicted in Fig. 4.1. The ions are rotating on a ring with circumference L with an inhomogeneous velocity profile $v(\theta)$ (see Fig. 4.2). Since the velocity profile should be stationary in the lab frame, the ions must be inhomogeneously spaced. Additional electrodes exerting a force $F^{\mathrm{e}}(\theta)$ on the ions generate the necessary (de-)acceleration. The oscillating displacements of the ions around this equilibrium motion are phonons with velocities $c(\theta) \propto (v(\theta))^{-1/2}$. Regions with sufficiently large ion spacings and sufficiently low phonon velocities are supersonic; here phonons can only move in the direction of the ion flow and are trapped like light inside a black hole. We consider a system with a super- and a subsonic region. The border between these regions is analogous to a black hole horizon and will be shown to emit Hawking radiation.

The plan of this chapter is the following. First we will describe the system of ions on a ring and explain why it is expected to show the Hawking effect in Sec. 4.2. Then we briefly review previous works which are relevant for our analysis in Sec. 4.3. After this preparation of the reader we present our simulation results and discuss them in Sec. 4.4. We are analyzing the Hawking effect in our system in two distinct ways: First we prove that the Hawking effect has a thermal spectrum by scattering pulses on the black hole horizon, second we are analyzing the emission of Hawking radiation from a black hole after its formation. In the latter situation we analyze the entanglement between pairs of Hawking particles, one inside and one outside the black hole. In this context we observe a transition from the *quantum* to the *classical* Hawking effect. Most importantly, this is suitable for experimental verification. In Sec. 4.5 we will discuss experimental setups which allow for the measurement of the analyzed physics.

4.2 Ion Ring System

In this section we are presenting our theoretical description of ions on a ring. In Sec. 4.2.1 we start with the full Hamiltonian, explain our assumptions and approximations, and point to the equations underlying our simulations. We establish the connection with the general description of analog black holes in hydrodynamical system by considering the continuum limit of the system in Sec. 4.2.2.

4.2.1 Discrete Ion System

In the following we are explaining the detailed setup of our proposal. The dynamics of N ions with mass m and charge e are described by the Hamiltonian

$$\mathcal{H} = -\sum_{i=1}^{N} \frac{4\pi^2\hbar^2}{2mL^2}\frac{\partial^2}{\partial\theta_i^2} + \sum_{i=1}^{N} V^{\mathrm{e}}\left(\theta_i\right) + V^{\mathrm{c}}\left(\theta_1,\ldots,\theta_N\right) \tag{4.1}$$

with the Coulomb potential V^{c} between the ions and a local external potential $V^{\mathrm{e}}\left(\theta\right)$ from external electrodes. Instead of specifying V^{e} we will impose an angular velocity profile $v\left(\theta\right)$ by fixing the equilibrium positions. The required V^{e} is then determined through the difference between the ion

acceleration $\ddot{\theta}_i^0(t)$ and the Coulomb force $F_i^c(\theta_1^0, \ldots, \theta_N^0)$. The Coulomb force and the external force are given in Appendix A.1.

To this aim we impose the classical equilibrium positions

$$\theta_i^0(t) = g\left(\frac{i}{N} + \frac{t}{T}\right), \tag{4.2}$$

where g maps the normalized indices $i/N \in [0,1]$ monotonically increasing onto the angles $\theta \in [0, 2\pi]$ and is periodically continued. g must be sufficiently smooth, i.e., three times continuously differentiable. The stationary angular velocity profile is

$$v(\theta) = \frac{g'(g^{-1}(\theta))}{T}, \tag{4.3}$$

where T denotes the rotation time of the ions (see Fig. 4.2) and g' is the derivative with respect to the argument of the function g. In a part of this chapter we consider to dynamically create a black hole metric from a flat metric. To this aim, we decrease $v_{\min}$ from the value $v_{\min} = 2\pi/T$ for homogeneously spaced ions in a Gaussian way with time constant τ (see Appendix A.2).

We choose a stationary velocity profile as depicted in 4.2. It is composed of a subsonic region with the constant angular ion velocity $v(\theta) = v_{\min}$ in the angular range $0 < \theta < \sigma v_{\min} T$ and $2\pi - \sigma v_{\min} T < \theta < 2\pi$. In the supersonic region $\sigma v_{\min} T < \theta < 2\pi - \sigma v_{\min} T$ the constant angular ion velocity is

$$v(\theta) = v_{\max} = \frac{2\pi}{T} \frac{1 - \frac{2\sigma v_{\min} T}{2\pi}}{1 - 2\sigma}. \tag{4.4}$$

The two velocities $v_{\min}$ and $v_{\max}$ are naturally constrained by the rotation time of the ions $v_{\min} < 2\pi/T < v_{\max}$. The black hole horizon in our system is located close to $\theta_{\mathrm{H}} = \sigma v_{\min} T$. Due to the ring structure a second horizon, the white hole horizon exists at $\theta_{\mathrm{H}} = 2\pi - \sigma v_{\min} T$. The transitions at the horizons between the subsonic and the supersonic regions contain $2\gamma_1$ (black hole horizon) and $2\gamma_2$ ions (white hole horizon). The exact expression for the velocity profile is given in the Appendix in Eq. (A.8).

We choose $v_{\min} = 2\pi \times 0.8\overline{3}/T$ and that the small transition regions $2\gamma_1, 2\gamma_2$ contain $0.04N$ and $0.1N$ ions if not stated otherwise. If necessary, the black hole is dynamically created in the small time interval $\tau = 0.05T$ (see Eq. (A.9)).

In this chapter we do not work with the full Hamiltonian (4.1). Instead, we treat small perturbations around the equilibrium motion $\hat{\theta}_i(t) = \theta_i^0(t) + \delta\hat{\theta}_i(t)$ and expand the Hamiltonian to second order in $\delta\hat{\theta}_i$

$$\mathcal{H} = \frac{1}{2m}\sum_{i=1}^{N}\delta\hat{p}_i^2 + \frac{m}{2}\sum_{i\neq j} f_{ij}(t)\delta\hat{\theta}_i\delta\hat{\theta}_j \tag{4.5}$$

with the time dependent force matrix $\mathcal{F} = (f_{ij})$ (see Appendix A.1) and the canonical operators $\delta\hat{\theta}_i$ and $L\delta\hat{p}_i/(2\pi) = -i\hbar\partial_{\delta\theta_i}$ describing the phononic oscillations of the ions. This harmonic approximation is valid if the typical variation of the ion position is much smaller than the ion spacing

$$\sqrt{\langle\delta\hat{\theta}^2\rangle} \approx \frac{2\pi}{L}\sqrt{\frac{\hbar}{mN\omega_{\mathrm{rot}}}}\left(\langle\hat{n}\rangle + \frac{1}{2}\right) \approx \frac{2\pi}{7\cdot 10^5}\left(\langle\hat{n}\rangle + \frac{1}{2}\right) \ll \frac{2\pi}{N}. \tag{4.6}$$

Here we use the typical mode frequency $N\omega_{\mathrm{rot}}$ where $\omega_{\mathrm{rot}} = 2\pi/T$ is the rotation frequency of the ions. If we tune the ion velocity to lie in the same order of magnitude as the sound velocity, ω_{rot} gives the smallest mode frequency. We insert the experimental parameters considered in Sec. 4.5 with $N = 1000$ here. In this chapter we propose an experiment with Hawking temperature T_{H} and initial temperature T_0 being not much larger than $\hbar\omega_{\mathrm{rot}}/k_{\mathrm{B}}$, so we can assume $\langle\hat{n}\rangle \sim 1$. Then the above requirement is nicely fullfilled.

The quasi-free quantum dynamics of this harmonic system (4.5) are governed by the classical linear equations of motion for the first and second moments. Through Wick's theorem all higher order correlation functions are determined by these moments. The first moments are $\langle\hat{\xi}_i\rangle$ with the definition

$$\hat{\xi}_i = \begin{cases} \delta\hat{\theta}_i & i \in \{0,\ldots,N-1\} \\ -i\hbar\hat{\partial}_{\theta i} & i \in \{N,\ldots,2N-1\}. \end{cases} \tag{4.7}$$

The second moments are grouped in the covariance matrix

$$\Gamma_{ij} = \frac{1}{2\hbar}\langle\{\hat{\xi}_i\hat{\xi}_j\}_+\rangle, \tag{4.8}$$

where $\{\}_+$ denotes an anticommutator. The equations governing the dynamics and determining the equilibrium states of the first and second moments are given in Appendix A.3.

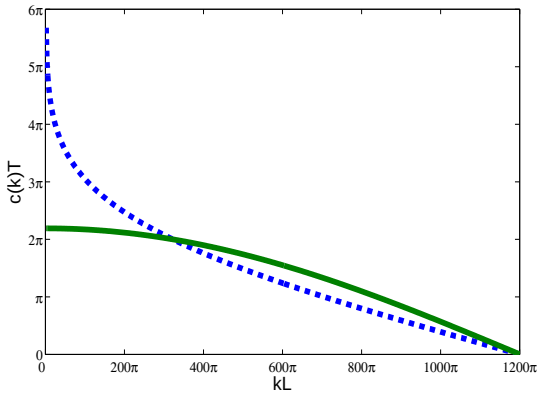

Figure 4.3: Phononic group velocity $c(k)$ in the flat subsonic region as a function of k for full Coulomb interactions (blue dashed line) and nearest-neighbor interactions only (green solid line). For nearest-neighbor interactions only the group velocity approaches a constant at small wavenumbers displaying the linear dispersion. For full Coulomb interactions a logarithmic divergence at small wavenumbers is observed for a finite system size. We use $\sigma v_{\min} T = 2\pi \cdot 0.375$, $N = 1000$, and $e^2/4\pi\epsilon_0 = 1.2591/(2N) \cdot mL^3T^{-2}$ (see Appendix A.2).

A stability analysis of this system is described in Appendix B. We find that exponential instabilities, though present in this system, are not important for the proposed experiment because it is performed during only one rotation period T.

4.2.2 Continuum Limit

In order to get some insight, we consider the limit of an infinite number of ions and formulate the analogy with the standard Hawking effect in this limit.

We will first study the behavior of the dispersion relation of the ions at small wavenumbers (see Fig. 4.3 for the finite chain). We use the approximation given in [PMD+08] for small wavenumbers in the open Coulomb chain taking into account the long range Coulomb interactions.

From

$$\omega(k) = ck\sqrt{1 - \frac{2}{3}\log\left(\frac{ka}{2}\right)} \tag{4.9}$$

with the ion spacing $a = L/N$ we get

$$\frac{d\omega(k)}{dk} = \frac{\omega}{k} - \frac{1}{3}\frac{c}{\sqrt{1 - \frac{2}{3}\log\left(\frac{ka}{2}\right)}} \tag{4.10}$$

and

$$\frac{d^2\omega(k)}{dk^2} = \frac{-c}{3k\sqrt{1 - \frac{2}{3}\log\left(\frac{ka}{2}\right)}}\left[1 + \frac{1}{3\left(1 - \frac{2}{3}\log\left(\frac{ka}{2}\right)\right)}\right] \tag{4.11}$$

For $k = 2\pi/L \cdot n$ with $1 \leq n \leq n_0 \ll N$ this can be summarized as

$$\frac{d\omega(k)}{dk} \approx \frac{\omega}{k}, \text{ and } \frac{d^2\omega(k)}{dk^2} \approx 0. \tag{4.12}$$

For a given k, the the phase and group velocity become identical in the continuum limit $N/L \to \infty$ as explicitly shown in Eq. (4.10). This is important for the definition of the Hawking temperature in the following, see Eq. (4.17). If group and phase velocity did not coincide, it would not be clear a priori how to determine the correct Hawking temperature. For example, in the scenario considered in [SU08], the product of group and phase velocity enters the formula for the Hawking temperature. Since both velocities are identical in the continuum limit for our proposal, for the finite system we can determine the Hawking temperature at a given k from the group velocity.

Now, we calculate the Lagrangian for the scalar field $\hat{\Phi}\left(\theta_i^0(t), t\right) = \delta\hat{\theta}_i(t)$ in the continuum limit. Here we can make an analogy with the standard Hawking effect as observed in [Unr81]. Because of the equilibrium motion of the ions the kinetic energy K transforms according to

$$\begin{aligned} K &= \frac{m}{2}\left(\frac{L}{2\pi}\right)^2 \sum_{i=1}^{N}\left(\frac{d\theta_i}{dt}\right)^2 \\ &\approx \int_0^{2\pi} d\theta \frac{\rho(\theta)}{2}\left(\frac{d}{dt}\Phi\left(\theta_i^0(t), t\right)\right)^2 \\ &= \int_0^{2\pi} d\theta \frac{\rho(\theta)}{2}\left(\partial_t\Phi + v(\theta)\,\partial_\theta\Phi\right)^2, \end{aligned} \tag{4.13}$$

where we introduced the conformal factor $\rho(\theta) = n(\theta) \cdot mL^2/(2\pi)^2$ with the density $n(\theta) = N/(v(\theta)T)$. For an homogeneous system the potential energy V transforms to

$$\begin{aligned} V &= \frac{m}{2}\sum_{i,j=1}^{N} f_{ij}\delta\theta_i\delta\theta_j = \sum_{k=0}^{N-1}\frac{m}{2}D(k)^2|\Phi_k'|^2 \\ &= \sum_{k=0}^{N-1}\sum_{\substack{n,m=1 \\ \theta_n=\frac{2\pi}{L}n}}^{N}\frac{L^2}{(2\pi)^2}\frac{m}{2N}D(k)^2 e^{-ik(\theta_n-\theta_m)}\Phi(\theta_n)\Phi(\theta_m) \\ &\approx \int_0^{2\pi} d\theta\frac{\rho(\theta)}{2}\left(iD(-i\partial_\theta)\Phi(\theta)\right)^2, \end{aligned} \tag{4.14}$$

where $D(\theta, k) = c(\theta)k + \mathcal{O}(k^3)$ is the dispersion relation of the Coulomb chain. Assuming a slowly varying $v(\theta)$, we can now formulate the Lagrangian for the ion system in the laboratory frame in the continuum limit

$$\mathcal{L} = \int d\theta\frac{\rho(\theta)}{2}\left[\left(\partial_t\hat{\Phi} + v(\theta)\partial_\theta\hat{\Phi}\right)^2 - \left(iD(\theta, -i\partial_\theta)\hat{\Phi}\right)^2\right]. \tag{4.15}$$

This scalar field satisfying a linear dispersion relation at low wavenumbers with sound velocity

$$(c(\theta))^2 = \frac{2\cdot n(\theta)}{m}\left(\frac{2\pi}{L}\right)^3\frac{e^2}{4\pi\epsilon_0} \tag{4.16}$$

for nearest-neighbor interactions, following from the actual form of the matrix f_{ij} given in Eq. (A.4), is analogous to a massless scalar field in a black hole spacetime as first shown in [Unr81]. Its quanta cannot escape a supersonic region with $v(\theta) > c(\theta)$ like photons trapped inside a black hole. The horizon of this analog model is located at $c(\theta_\mathrm{H}) = v(\theta_\mathrm{H})$ with $\theta_\mathrm{H} \approx \sigma v_\mathrm{min}T$. Following [Unr81], pairs of Hawking particles are emitted close to the black hole horizon with a black body distribution at the Hawking temperature

$$\frac{k_\mathrm{B}T_\mathrm{H}}{\hbar} = \frac{\kappa}{2\pi} = \frac{1}{4\pi v}\frac{d}{d\theta}\left(v^2 - c^2\right)|_\mathrm{H} = \frac{3}{4\pi T}\frac{g''(g^{-1}(\theta))}{g'(g^{-1}(\theta))}\Big|_{\theta=\theta_\mathrm{H}}. \tag{4.17}$$

The first equality defines the surface gravity κ (see [Haw74, Unr81]), in terms of the Hawking temperature. The second equality is derived in

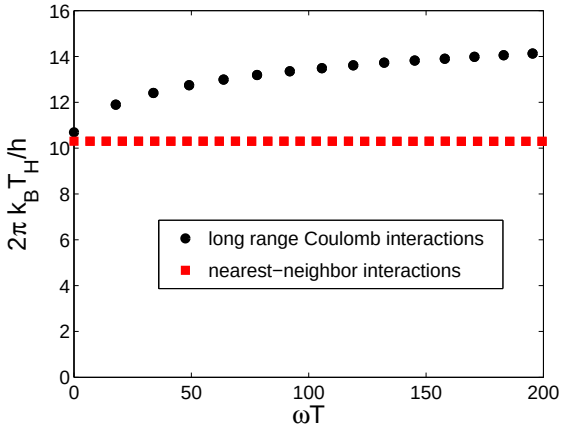

Figure 4.4: Dependence of the Hawking temperature T_{H} on the discrete mode frequencies $\omega(k)$ in the comoving frame. For nearest-neighbor interactions, the variation with the wavenumber is not visible, for long range Coulomb interactions variations are present. This is due to the nonlinear dispersion. Note that we use a single Hawking temperature for the full system. We use $\sigma v_{\mathrm{min}} T = 0.375$, $N = 1000$. (red) Nearest-neighbor interactions with $e^2/4\pi\epsilon_0 = \frac{1}{2N}\frac{mL^3}{T^2}$; (black) Full Coulomb interactions with $e^2/4\pi\epsilon_0 = \frac{1}{2N}\frac{mL^3}{T^2}$ (see Appendix A.2).

reference [Unr81], the third one results from the explicit forms for $v\,(\theta)$ and $c\,(\theta)$ for nearest-neighbor interactions.

In the case of long-range Coulomb interactions, the calculation of the Hawking temperature T_{H} (see Eq. (4.17)) is difficult because of the non-linear dispersion relation at low wavenumbers. In order to estimate the impact of this dispersion, let us introduce an effective wavenumber-dependent Hawking temperature. Because the ion spacings are inhomogeneous, we use a local density approximation. At each angle θ we calculate the local density $n(\theta)$ of the ions. We then extract a group velocity $c(\theta)$ from the analogous homogeneous system with constant density and $N_\theta = [n(\theta)]$ ions, where the square brackets denote rounding to the nearest integer. The group velocity is calculated from the dispersion relation at adjacent wavenumbers. With this method we calculate angle- and wavenumber-dependent group velocities $c(\theta, k)$. By comparing $c(\theta, k)$ with the ion velocities $v(\theta)$, we find for each wavenumber the black hole horizon θ_{H}. The derivative of c in Eq. (4.17) is performed with respect

to the ion number N_θ instead of the angle θ to get along with a single rounding procedure $N_\theta = [n(\theta)]$. Thus, Eq. (4.17) is transformed into

$$\begin{aligned}\frac{k_\mathrm{B} T_\mathrm{H}(k)}{\hbar} &= \frac{1}{2\pi T}\frac{g''\left(g^{-1}(\theta)\right)}{g'\left(g^{-1}(\theta)\right)}\bigg|_{\theta=\theta_\mathrm{H}} \cdot \\ &\qquad \left(1+\frac{N_{\theta_\mathrm{H}}}{g'\left(g^{-1}(\theta)\right)^2}\bigg|_{\theta=\theta_\mathrm{H}}\frac{\partial}{\partial N_\theta}c\left(N_\theta,k\right)\bigg|_{N_\theta=N_{\theta_\mathrm{H}}}\right) \\ &\approx \frac{1}{2\pi T}\frac{g''\left(g^{-1}(\theta)\right)}{g'\left(g^{-1}(\theta)\right)}\left(1+N_{\theta_\mathrm{H}}\frac{c\left(N_{\theta_\mathrm{H}}+1,k\right)-c\left(N_{\theta_\mathrm{H}},k\right)}{g'\left(g^{-1}(\theta)\right)^2}\right)\bigg|_{\theta=\theta_\mathrm{H}}.\end{aligned} \tag{4.18}$$

The dependence of the Hawking temperature on the wavenumber is depicted in Fig. 4.4 for the parameters used in the analysis in Sec. 4.4.1. For nearest-neighbor interactions, the variation with the wavenumber is not visible, for long range Coulomb interactions variations are present. This is due to the nonlinear dispersion relation. We make an arbitrary choice and use one of these temperatures at small wavenumbers to analyze the whole system at all wavenumbers. In Sec. 4.4.1 we will discuss how our results depend on this choice. Note that in the continuum limit the dispersion relation for full Coulomb interactions becomes linear which resolves the arbitrariness. Thus we find a single Hawking temperature for the full system based on the form of the velocity profile.

4.3 Review

In this section we will give a short summary of previous works related to our proposal (see [BFF+05b] for further details). In Sec. 4.3.1 we are describing a basic derivation of Hawking radiation with quantum field theory in curved spacetime for systems with a strictly linear dispersion relation. Secondly, we present a theoretical method that tests whether the expected radiation has a thermal spectrum [Unr95, CJ98, JM99] for systems with sublinear dispersion relations (see Sec. 4.3.2). Then we explain a proposal, originally aiming at Bose Einstein Condensates [BFF+08, CFR+08, MP09a], how to detect Hawking radiation in an experiment as quantum correlations emerging between a supersonic and a subsonic region, i.e., between the inside and the outside of a black hole (see Sec. 4.3.3).

4.3.1 Hawking radiation and Mode Conversion

In this section we will summarize the derivation of Hawking radiation for a massless scalar field with a linear dispersion relation $D(k) = ck$ in a black hole analog spacetime, defined by a velocity profile $v(\theta)$ (see Eq. (A.10) and Eq. (A.8)) and a density profile $\rho(\theta)$. This system is governed by the Lagrangian

$$\mathcal{L} = \int d\theta \frac{\rho(\theta)}{2} \left[\left(\partial_t \hat{\Phi} + v(\theta) \partial_\theta \hat{\Phi} \right)^2 - c^2 \partial_\theta \hat{\Phi}^2 \right]. \tag{4.19}$$

We will in the following assume $\rho(\theta)$ to be constant and work with the field $\Psi = \sqrt{\rho}\Phi$. The correspondend classical field equation is

$$\left[(\partial_t + \partial_\theta v(t,\theta)) (\partial_t + v(t,\theta) \partial_\theta) - c^2 \partial_\theta^2 \right] \Psi(t,\theta) = 0. \tag{4.20}$$

The solutions of this equation determine the notion of excitation modes in the system and are of the form

$$\Psi(t,\theta) = \sum_{\pm} \int_0^\infty d\omega \left(\Psi_\omega^{\pm}(t,\theta) + H.c. \right) \tag{4.21}$$

with $\Psi_\omega^{\pm}(t,\theta) = \exp(\pm i\omega t) \Psi_\omega(\theta)$ for a stationary spacetime. ω denotes the frequency in the lab frame, it is related by $\omega = (v \pm c)k \cdot L/(2\pi)$ to the frequency $\pm ck$ in the comoving frame. The solutions Ψ_ω are normalized with respect to the Klein-Gordon inner product

$$\langle \Psi_\omega \big| \Psi_{\omega'} \rangle = \frac{-i}{2} \int_0^{2\pi} d\theta \left[\Psi_\omega^* (\partial_t + v\partial_\theta) \Psi_{\omega'} - \Psi_{\omega'} (\partial_t + v\partial_\theta) \Psi_\omega^* \right]. \tag{4.22}$$

For each frequency ω we can find four independent modes $\Psi_\omega^{\pm}/\Psi_\omega^{\pm *}$. Complex conjugation relates modes with a positive/negative sign of the Klein-Gordon norm $\mathcal{N}_\omega = \langle \Psi_\omega \big| \Psi_\omega \rangle$, corresponding to positive/negative frequency modes or particles/anti-particles. Note that the frequency in the comoving frame $\pm ck$ determines the sign of $\mathcal{N}$. The index $\pm$ denotes modes which are left-/rightmoving (up-/downstream) in the comoving frame. Finally, the scalar field theory is quantized by expanding the field operator in the modes (we drop the summation index $\pm$ now)

$$\hat{\Psi} = \sum_\omega \left(\hat{a}_\omega \Psi_\omega + \hat{a}_\omega^\dagger \Psi_\omega^* \right) \tag{4.23}$$

and postulating canonical bosonic commutation relations for the mode operators $\hat{a}_\omega$

$$[\hat{a}_\omega, \hat{a}_{\omega'}] = 0, \ \ \left[\hat{a}^\dagger_\omega, \hat{a}_{\omega'}\right] = \delta_{\omega,\omega'}. \tag{4.24}$$

The vacuum of the system is defined to be annihilated by all $\hat{a}_\omega$

$$\hat{a}_\omega \big|0\rangle = 0, \ \ \forall\omega. \tag{4.25}$$

We want to study the following time dependent situation: At initial times, called *in*, the black hole is not present, the vacuum state is denoted $\big|\text{in}\rangle$ with corresponding modes $\hat{a}^{\text{in}}_\omega$. Then a black hole is created. At final times, called *out*, the vacuum state of the system is $\big|\text{out}\rangle$ with corresponding modes $\hat{a}^{\text{out}}_\omega$. We are here interested in the time evolution of the system from initial to final times starting from the vacuum state of the system $\big|\text{in}\rangle$. The result of this time evolution can be described by a Bogoliubov transformation on the classical modes or the quantum mode operators

$$\Psi^{\text{out}}_\omega = \sum_\omega \left(\alpha_{\omega\omega'}\Psi^{\text{in}}_{\omega'} + \beta_{\omega\omega'}\Psi^{in*}_{\omega'}\right), \tag{4.26}$$

$$\hat{a}^{\text{out}}_\omega = \sum_\omega \left(\alpha^*_{\omega\omega'}\hat{a}^{\text{in}}_{\omega'} - \beta^*_{\omega\omega'}\hat{a}^{in\dagger}_{\omega'}\right) \tag{4.27}$$

with the Bogoliubov coefficients $\alpha_{\omega\omega'}$ and $\beta_{\omega\omega'}$. For a static and continuous system the frequency ω is conserved and the Bogoliubov coefficients are diagonal, e.g., $\beta_{\omega\omega'} = \delta_{\omega,\omega'}\beta_\omega$. The coefficients are related through $|\alpha_\omega|^2 - |\beta_\omega|^2 = 1$. The particle content of the state $\big|\text{out}\rangle$ in terms of the state $\big|\text{in}\rangle$ is related to the Bogoliubov coefficients through

$$\langle\text{in}\big|\hat{N}^{\text{out}}_\omega\big|\text{in}\rangle = \sum_{\omega'}|\beta_{\omega\omega'}|^2 = |\beta_\omega|^2. \tag{4.28}$$

Therefore, it is nonvanishing if the time evolution from initial to final times mixes positive and negative frequency modes. In particular, the production of Hawking particles can be understood as the evolution of initial positive frequency modes into final negative frequency modes. The Bogoliubov coefficients of the inverse transformation have the same modulus as the ones of the forward transformation

$$\Psi^{\text{in}}_\omega = \sum_\omega \left(\alpha^*_{\omega\omega'}\Psi^{\text{out}}_{\omega'} - \beta_{\omega\omega'}\Psi^{\text{out}*}_{\omega'}\right), \tag{4.29}$$

$$\hat{a}^{\text{in}}_\omega = \sum_\omega \left(\alpha_{\omega\omega'}\hat{a}^{\text{out}}_{\omega'} - \beta^*_{\omega\omega'}\hat{a}^{\text{out}\dagger}_{\omega'}\right). \tag{4.30}$$

We will employ this relation to numerically determine the Bogoliubov coefficients for the discrete case of ions on a ring.

In the following we will briefly summarize the analytical calculation of the Bogoliubov coefficients for a continuous system with a strictly linear dispersion relation. One can decompose the field operator at late time into an upstream $\hat{\Psi}^-$ and a downstream $\hat{\Psi}^+$ part

$$\hat{\Psi} = \hat{\Psi}^+ + \hat{\Psi}^-. \tag{4.31}$$

The downstream part is not strongly affected by the black hole creation, hence the particle creation in this part is negligible $\beta^+_\omega = 0$. This assumes that the mixing between upstream and downstream parts is small – otherwise we would have to include a grey-body factor, cf. [Haw74]. So Hawking radiation is created by the upstream part only. It can further be decomposed into modes $\Psi^-_{\omega,\mathrm{super}}$ inside the supersonic and $\Psi^-_{\omega,\mathrm{sub}}$ inside the subsonic region. The decomposition of the field operators is finally

$$\hat{\Psi}^- = \hat{\Psi}^-_{\mathrm{super}} + \hat{\Psi}^-_{\mathrm{sub}}, \tag{4.32}$$

$$\hat{\Psi}^-_{\mathrm{super}} = \int_0^\infty d\omega \left(\hat{a}^-_{\omega,\mathrm{super}} \Psi^-_{\omega,\mathrm{super}} e^{-i\omega t} + H.c. \right), \tag{4.33}$$

$$\hat{\Psi}^-_{\mathrm{sub}} = \int_0^\infty d\omega \left(\hat{a}^{-\dagger}_{\omega,\mathrm{sub}} \Psi^{-*}_{\omega,\mathrm{sub}} e^{-i\omega t} + H.c. \right). \tag{4.34}$$

We have to find the regular in field after the horizon formation $\Psi^-_{\omega,\mathrm{in}}$, decompose it in terms of the out modes

$$\Psi^-_{\omega,\mathrm{in}}(\theta) = \alpha_\omega \Psi^-_{\omega,\mathrm{sub}}(\theta) + \beta_\omega \Psi^-_{\omega,\mathrm{super}}(\theta), \tag{4.35}$$

and read off the Bogoliubov coefficients α_ω and β_ω. So in summary, we calculated the time evolution of global upstream waves before the black hole creation into upstream waves after the black hole creation on both sides of the horizon. In the lab frame the resultant waves travel away from the horizon on both sides.

The interesting Bogoliubov coefficient β_ω is found to be

$$|\beta_\omega|^2 = \frac{1}{\exp\left(\frac{\hbar\omega}{k_\mathrm{B} T_\mathrm{H}}\right) - 1} \tag{4.36}$$

with the Hawking temperature T_H (see Eq. (4.17)). We summarize these findings by stating that Hawking radiation emitted after the creation of a

black hole has a thermal spectrum

$$\langle \text{in} \big| \hat{N}_\omega^{\text{out}} \big| \text{in} \rangle = \sum_\omega \frac{1}{\exp\left(\frac{\hbar\omega}{k_\text{B} T_\text{H}}\right) - 1}. \tag{4.37}$$

4.3.2 Scattering of Pulses

The derivation of Hawking radiation presented in the last Section 4.3.1 suggests calculating the Bogoliubov coefficients from the time evolution of classical pulses scattering at the black hole horizon. It is numerically advantageous to calculate the scattering process backwards in time. In the following we will focus on the situation of a sublinar dispersion relation in a continuum system as studied in [Unr95].

The calculation starts from a pulse with negative frequencies and small positive wavenumbers at late times. This pulse is moving upstream and is leftmoving in the comoving as well as in the lab frame. We then calculate its history in time: It approaches the horizon and is reflected by it. The reflected pulse mainly consists of two early-time upstream pulses, one positive and one negative frequency pulse, at high absolute wavenumbers. The positive/negative wavenumber pulse has negative/positive frequencies in the comoving frame, i.e., both are upstream pulses. But they have such a small group velocity - remember the sublinear dispersion relation (see 4.3) - that they are dragged along with the ion background. So they are rightmoving in the lab frame, while being leftmoving in the comoving frame. These pulses can be determined due to frequency conservation for a static system in the lab frame. Note that the sign of the frequency in the comoving frame determines the sign of the Klein-Gordon norm (see Eq. (4.22)) and thus the notion of particles versus anti-particles. Therefore, the relation between the late-time negative frequency and early-time positive frequency pulse is important for the particle producing Hawking effect.

Now, we will explain this mode conversion with the help of this frequency conservation and the dependence of the dispersion relation on the local ion velocity. The frequency in the lab frame is

$$\omega_\text{lab} = vk\frac{L}{2\pi} \pm D(k), \tag{4.38}$$

i.e., it is the Doppler shifted dispersion in the comoving frame $\omega_\text{com} = \pm D(k)$. In Fig. 4.5 we depict the pulses at different times during the

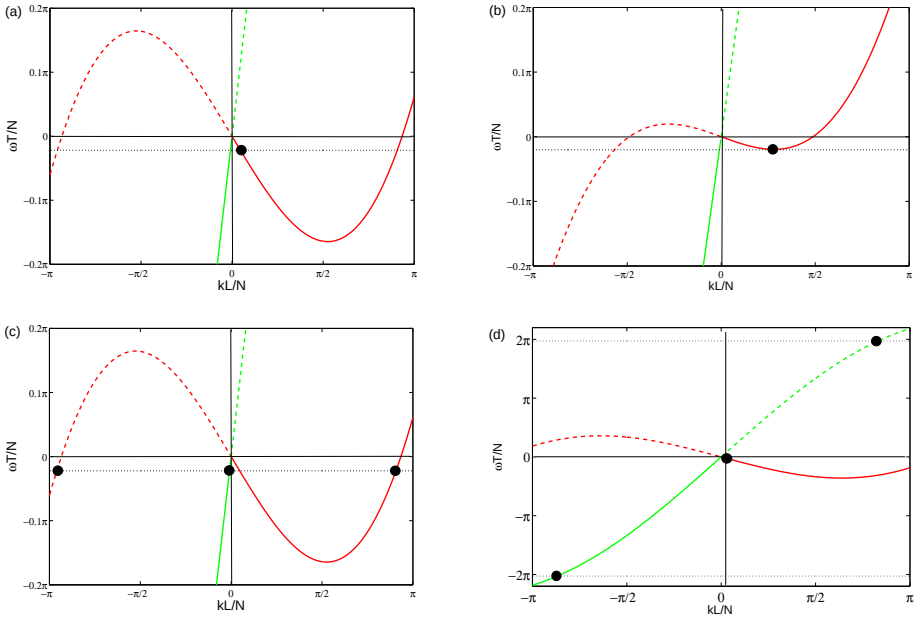

Figure 4.5: Schematical depiction of the dispersion relation for the scattering process of a final negative frequency pulse from the black hole horizon. Negative/positive frequency modes are depicted with solid/dashed lines. Upstream/downstream modes are depicted in red/green. The situation at late times is presented in (a), at intermediate times, when the pulse hits the horizon, in (b), and at early times in (c). Part (d) shows the situation outside of the black hole for small ion velocities, for which we observe the effect analogous to Bloch oscillations (see text).

simulation (a-c) on the dispersion relation in the stationary lab frame together with the initial pulse frequency ω_0. For comparison the interested reader can compare with Fig. 4.6 depicting the pulses in real space. We are starting our discussion at late times (see Fig. 4.5(a)) with a single pulse, upstream and with negative frequency. Its negative group velocity in the lab frame means that it is leftmoving in the lab frame. When the pulse is approaching the black hole horizon backwards in time the ion velocity at the pulse increases. In comparing Fig. 4.5(a) and Fig. 4.5(b) one can observe the blueshifting of the pulse. When the pulse reaches the horizon, it is approximately at the minimum of the dispersion relation (see Fig. 4.5(b)). Now the mode conversion occurs, which is restricted

by the frequency conservation in the stationary lab frame. Apart from the late-time pulse, three pulses are in agreement with frequency conservation. One pulse is moving downstream at low negative wavenumbers with negative frequencies. Thus, in the lab frame it is a fast rightmoving pulse. The two other solutions are at high absolute wavenumbers and are upstream, but slowly rightmoving in the lab frame. The positive/negative frequency contribution of the upstream pulse is located at positive/negative wavenumbers. Backwards in time all three pulses travel leftwards away from the horizon (see Fig 4.5(c)). Note that in [Unr95] the downstream pulse is not observed in the actual dynamics.

From a comparison between the Klein-Gordon norms of the late-time negative frequency pulse and the early-time positive frequency pulse the Bogoliubov coefficients $|\beta_\omega|^2$ can be extracted. In the literature a different approach is chosen, with the assumption that Hawking radiation is thermal, i.e., that the Bogoliubov coefficient is given by Eq. (4.36), the Klein-Gordon norm 4.22 of the early-time pulse is calculated from the late-time pulse. The Klein-Gordon norm of the early-time positive frequency pulse is

$$\mathcal{N}^+ = \int \mathcal{N}_k^+(t<0)dk. \tag{4.39}$$

It is compared with the prediction from the late-time pulse

$$\mathcal{N}^0 = \int \frac{\mathcal{N}_k^0(t=0)}{\exp\left(\frac{\hbar\omega}{kT_\mathrm{H}}\right)-1}dk. \tag{4.40}$$

Either the norms are compared in total or frequency-wise with the help of the expression $dk = \frac{dk}{d\omega}d\omega$, i.e., by division with the pulse velocities in the lab frame. One can compare the early-time positive frequency pulse

$$\widetilde{\mathcal{N}}_k^+ = \frac{\mathcal{N}_k(t<0)}{v_\mathrm{min}-c_k} \tag{4.41}$$

with the prediction from the late-time negative frequency pulse

$$\widetilde{\mathcal{N}}_k^0 = \frac{\mathcal{N}_k(t=0)}{v_\mathrm{min}-c_k}\frac{1}{\exp\left(\frac{\hbar\omega_k}{k_\mathrm{B}T}\right)-1}, \tag{4.42}$$

and the prediction from the early-time negative frequency pulse

$$\widetilde{\mathcal{N}}_k^- = \frac{\mathcal{N}_k(t<0)}{v_\mathrm{min}-c_k}\exp\left(-\frac{\hbar\omega_k}{k_\mathrm{B}T}\right). \tag{4.43}$$

In [Unr95] the thermal hypothesis is confirmed using both the integrated and the modewise comparison.

In [CJ98, JM99] a discretized hydrodynamic system is treated with the same method. On a lattice the dispersion relation is naturally sublinear. Since the lattice is moving, the frequency in the lab frame is not conserved anymore. It is shown numerically exact and with analytical approximations (WKB theory) that the mechanism of mode conversion described in [Unr95] persists in this scenario. Even the Bogoliubov coefficients extracted from the comparison of early-time and late-time modes agree with the predictions for a continuum system with strictly linear dispersion relation (see Eq. (4.36)). The existence of a downstream pulse is not reported in [CJ98, JM99], too.

For a discrete and finite system with N particles on a system of size L a finite number of wavenumbers exists

$$k \in \left\{ -\frac{(N'-2)\pi}{L}, -\frac{(N'-4)\pi}{L}, \ldots, \frac{N'\pi}{L} \right\} \tag{4.44}$$

with the renormalized ion number

$$N' = N\frac{(2\pi)/T}{v}. \tag{4.45}$$

N' appears because the local ion spacing is not L/N, but $a(\theta) = L/N' = L/N \cdot v(\theta)T/(2\pi)$ in the inhomogeneous system. This Brillouin zone is already visualized in Fig. 4.5. In this system a symmetry under combined translations in space and time survives,

$$i \to i + 1 \tag{4.46}$$

$$t \to t + T/N \tag{4.47}$$

(see Eq. (4.2)). In a homogeneous part of the system this symmetry implies that the state of the system is invariant under the combined transformation

$$k \to k + \frac{2\pi}{L}N'n, \tag{4.48}$$

$$\omega \to \omega + \frac{2\pi}{T}Nn \tag{4.49}$$

for any integer n.

We use this transformation to explain an effect described in [CJ98, JM99] analogous to Bloch oscillations. The two high wavenumber solutions of the frequency conservation condition can lie outside the Brillouin zone. Then we find the solutions by looking at the frequencies $\omega_0 \pm 2\pi N/T$, depicted in Fig. 4.5(d). Thus, the early-time pulses are instead located on the downstream branch of the frequency condition. The positive/negative frequency pulse is located at high positive/negative wavenumbers (see Fig. 4.5(d)).

4.3.3 Correlations

The Hawking effect produces pairs of particles propagating away from the horizon in opposite directions, one outside the black hole (the Hawking particle), and one inside the black hole (its infalling partner). Taking advantage of this, it has been proposed to detect Hawking radiation via correlation measurements (see [BFF+08]), which reveal the entanglement between the two Hawking partners. In [BFF+08, CFR+08, MP09a] the density-density cross-correlation of phonons on both sides of the horizon produced through the Hawking process in a sonic black hole built up with a Bose-Einstein condensate (BEC) is studied [GAC+00, GAC+01, FF03]. In a quasi one-dimensional weakly interacting BEC in the hydrodynamical approximation the sound propagation is described by

$$\mathcal{L} = \int d\theta \frac{\mathcal{K}}{2} \left[\left(\partial_t \Phi + v\left(\theta\right) \partial_\theta \Phi \right)^2 - c^2 \partial_\theta \Phi^2 \right] . \tag{4.50}$$

This is manifestly the same as Eq. (4.19) apart from the actual form of the conformal factor $\mathcal{K}$, which if constant does not affect the dynamics appart from a rescaling of the fields. So the propagation of phonons in a BEC, i.e., phase/density excitations, and the propagation of phonons in a ring of ions, i.e., displacements of ions from their equilibrium position, are described by the same physics, and therefore share similar behaviors. Thus, the analysis performed in [BFF+08] can be translated into the context of ion rings.

The general equal-time two-point correlator $\langle \hat{\Psi}(\theta) \hat{\Psi}(\theta') \rangle$ in 1+1 dimensional space-times is given by [BD82]

$$\langle \hat{\Psi}(\theta) \hat{\Psi}(\theta') \rangle = - \lim_{t' \to t} \frac{\hbar}{4\pi} \log \left[\left(U(\theta, t) - U(\theta', t') \right) \left(V(\theta, t) - V(\theta', t') \right) \right] . \tag{4.51}$$

This is the stationary correlator of a massless minimally coupled quantum scalar field in 1 spatial dimension. It exhibits a characteristic structure with the logarithmic distance between the two points as the difference between the null coordinates U and V [BD82]. The meaning of the null coordinates is the following: the mode solution can always be written in the form $\sim e^{-i\omega U}$ for upstream modes and $\sim e^{-i\omega V}$ for downstream modes. The modes propagating upstream (downstream) move along space-time trajectories that keep the V (U) coordinates constant. For example, if the system is at rest and homogeneous, the analog spacetime is the Minkowskii (flat) one, and the Kruskal coordinates reduces to the familiar $U = t+\theta/c$, $V = t - \theta/c$, that define the standard light- (sound-) cones. As already pointed out in [BFF$^+$08] using these as Kruskal coordinates, one is able to recover the correct behavior of the density-density correlator in one dimension for a homogeneous BEC scaling as the inverse squared of the distance between the two points. If the system is more complicated (i.e., non-homogeneous or moving), the mode propagation is different, and the associated null coordinates will display distortion.

Eq. (4.51) applies to all conformally invariant theories in 1+1 dimensional spacetimes (which are always conformally flat). In the present case, the theory we are dealing with is not conformally invariant for the presence of the conformal factor $\mathcal{K}$ in the action. Nevertheless, assuming that $\mathcal{K}$ varies smoothly over the system, the correlator can be approximated using Eq. (4.51) also in the present case by

$$\langle\hat{\Phi}(\theta)\hat{\Phi}(\theta')\rangle = -\lim_{t'\to t}\frac{\hbar}{4\pi}\frac{1}{\sqrt{\mathcal{K}(\theta)\mathcal{K}(\theta')}} \log\left[\left(U(\theta,t)-U(\theta',t')\right)\left(V(\theta,t)-V(\theta',t')\right)\right], \quad (4.52)$$

where the $1/\sqrt{\mathcal{K}(\theta)\mathcal{K}(\theta')}$ term follows from a rescaling of the field, and terms containing derivatives of $\mathcal{K}$ are neglected.

Let us move to the evaluation of this correlator in the presence of Hawking radiation. Since the modes responsible for the emission Hawking radiation are the upstream modes $\hat{\Psi}^-$, we will focus on the upstream sector of Eq. (4.51) only. The equal-time two-point correlator in the presence of a black hole horizon is given by [BD82]

$$\langle\hat{\Phi}^-(\theta)\hat{\Phi}^-(\theta')\rangle = -\lim_{t'\to t}\frac{\hbar}{4\pi}\frac{1}{\sqrt{\mathcal{K}(\theta)\mathcal{K}(\theta')}}\log\left(U(\theta,t)-U(\theta',t')\right). \quad (4.53)$$

The downstream part of the correlator remains unaffected even in the

presence of a horizon, i.e., V still reads $t - \theta/c$. The only modes which get distorted by the presence of the horizon are the upstream ones which become far away from the horizon [Unr81, BFF+05a, BFF05, BFF+05b]

$$U(\theta, t)_{in/out} = \pm e^{-\kappa(t + \frac{\theta}{c(\theta) - v(\theta)})} \tag{4.54}$$

for the interior (+) and the exterior (-) region of the black hole. They suffer the typical exponential distortion of the upstream modes due to the presence of a black hole horizon [BD82, Unr81] (discarding transients). The exponential distortion follows from the wave equation for a linearized velocity profile at the horizon. κ is the surface gravity on the sonic horizon which is proportional to the Hawking temperature (see Eq. (4.17)). It is worth emphasizing that the form of the modes (4.54) is universal for any black hole horizon formation, independent of the details of its formation. This is the origin for the universal behavior of Hawking radiation.

The momentum-momentum correlator

$$\langle \delta\hat{p}^-(\theta)\delta\hat{p}^-(\theta')\rangle \tag{4.55}$$

can be obtained from Eq. (4.53). The conformal factor $\mathcal{K}$ must be replaced with the conformal factor from the Lagrangian of ions on a ring (see Eq. (4.19)). With the relation

$$\delta\hat{p}^- = \frac{L}{2\pi} m(\partial_t + v\partial_\theta)\hat{\Phi}^- \tag{4.56}$$

one gets

$$\langle \delta\hat{p}^-(\theta)\delta\hat{p}^-(\theta')\rangle = \frac{\hbar m}{16\pi} \frac{1}{[c(\theta) - v(\theta)]\,[c(\theta') - v(\theta')]} \sqrt{\frac{c(\theta)c(\theta')}{n(\theta)n(\theta')}} \frac{\kappa^2}{\cosh^2\left[\frac{\kappa}{2}\left(\frac{\theta}{c(\theta)-v(\theta)} - \frac{\theta'}{c(\theta')-v(\theta')}\right)\right]}. \tag{4.57}$$

This correlator has the typical form associated to the Hawking effect. The correlations are scaling with the square of the Hawking temperature. For θ and θ' on opposite sides of the sonic horizon, $c(\theta) - v(\theta)$ and $c(\theta') - v(\theta')$ have opposite sign. Therefore, the momentum-momentum cross-correlations are negative. They exhibit a peculiar peak along a straight line for $\theta = \frac{c(\theta)-v(\theta)}{c(\theta')-v(\theta')}\theta' \propto \theta'$. These cross-correlations correspond to the two entangled Hawking particles propagating in opposite directions as they move apart from the horizon.

4.4 Simulations for Ion Rings

We are now returning to the discussion of the discrete ion chain. In this section we are presenting the results of our simulations and are comparing them with the predictions and expectations from Sec. 4.3. We are pursuing two routes of simulations: First we simulate the scattering of pulses on the black hole horizon in Sec. 4.4.1. From the result we can deduce the Bogoliubov coefficients and theoretically confirm the thermal hypothesis (see Sec. 4.3.2). A second series of simulations presented in Sec. 4.4.2 is analyzing the emergence of correlations between the inside and the outside of a black hole after its creation (see Sec. 4.3.3). These correlations demonstrate the pair creation mechanism of Hawking radiation and are closely related to the emergence of entanglement between the inside and the outside of a black hole. In contrast to the scattering analysis, these simulations also act as direct proposal for an experiment as further discussed in Sec. 4.5.

4.4.1 Scattering of Pulses

Our numerical results for the propagation of a final pulse backwards in time in the discrete system of phonons on an ion ring are presented in the following. We first introduce the quantities necessary for this analysis. If the phononic excitations are localized in the flat subsonic region with constant ion velocity $v_{\min}$, the excitations $\delta\theta_i(t)$ and $\delta\dot{\theta}_i(t)$ can be expressed as modes $\delta\theta_k(t)$ and $\delta\dot{\theta}_k(t)$ with wavenumber k, where the dot represents the time derivative in the comoving frame. Due to the finite system size only discrete wavenumbers appear (see Eqs. (4.44) and (4.45)) and thus the dispersion relation is also discrete. The positive and negative frequency part of these excitations are defined by

$$\delta\theta_k^{\pm}(t) = \frac{1}{2}\left(\delta\theta_k(t) \pm i\delta\dot{\theta}_k(t)/\omega_k\right), \tag{4.58}$$

$$\delta\dot{\theta}_k^{\pm}(t) = \frac{1}{2}\left(\delta\dot{\theta}_k(t) \mp i\omega_k\delta\theta_k(t)\right). \tag{4.59}$$

These relations follow from the spatial behavior $\delta\theta\,(\theta) \sim \exp\left(ik\frac{\theta}{2\pi}L\right)$ in regions of constant ion velocity $v\,(\theta) = v$ [Unr95]. The analysis of the particle production requires us to use the Klein-Gordon norm for these modes. In our special case the Klein-Gordon norm defined in Eq. (4.22)

becomes up to a constant

$$\mathcal{N} = \sum_{k,\pm} \mathcal{N}_k \tag{4.60}$$

with

$$\mathcal{N}_k^{\pm} = \delta\dot{\theta}_k^{\pm *}\delta\theta_k^{\pm} - \delta\theta_k^{\pm *}\delta\dot{\theta}_k^{\pm}. \tag{4.61}$$

We are now describing the numerical calculation of the Bogoliubov coefficients with the method presented in Sec. 4.3.2. In summary, we are calculating the history of a negative frequency pulse on the upstream branch of the dispersion relation that travels away from the horizon. Back in time it scatters off the horizon and originates from several pulses. The early-time positive frequency pulse and the late-time negative frequency pulse are related through the Bogoliubov coefficients.

We start from the final pulses

$$\delta\theta_k^s(0) = k \cdot e^{-\left(\frac{k-2\pi s}{40\pi}\right)^2}, \quad s = 1, \ldots, 20, \tag{4.62}$$

centered at different wavenumbers k to test different frequency ranges. We calculate its history with Newton's equations of motion given in Appendix A.3 (see Eq. (A.11)) by using an iterative differential equation solver. From frequency conservation in the lab frame we expect three pulses on the upstream branch of the dispersion relation [Unr95, CJ98, JM99] (see Sec. 4.3.2).

Before coming to the simulation results, we will discuss the parameter regime used in this section. The ratio between the typical pulse frequency ω in the comoving frame and the Hawking temperature is of order $\hbar\omega/k_B T_H \sim 10$ (see also Fig. 4.4). In [MP09b] the deviations from thermality have been examined based on the quantity

$$\omega_{\max} = \max_{k>0} \left(D(k) - vkL/2\pi\right). \tag{4.63}$$

Here $\omega_{\max}$ takes the following values: $\omega_{max} = 290/T$ for nearest-neighbor interactions only (Fig. 4.8a), $\omega_{max} = 610/T$ for full Coulomb interactions (Fig. 4.8b). The surface gravity for the former case is $\kappa = 65/T$, for the latter $\kappa = 82/T$ (see Fig. 4.4), thus the ratios are $\omega_{max}/\kappa = 4.5$ and $\omega_{max}/\kappa = 7.4$. This regime is identified as the regime of small deviations from thermality in [MP09b]. This prediction applies to systems with nearest-neighbor interactions only. One of the main results of our paper is to consider also the long range Coulomb interactions for which

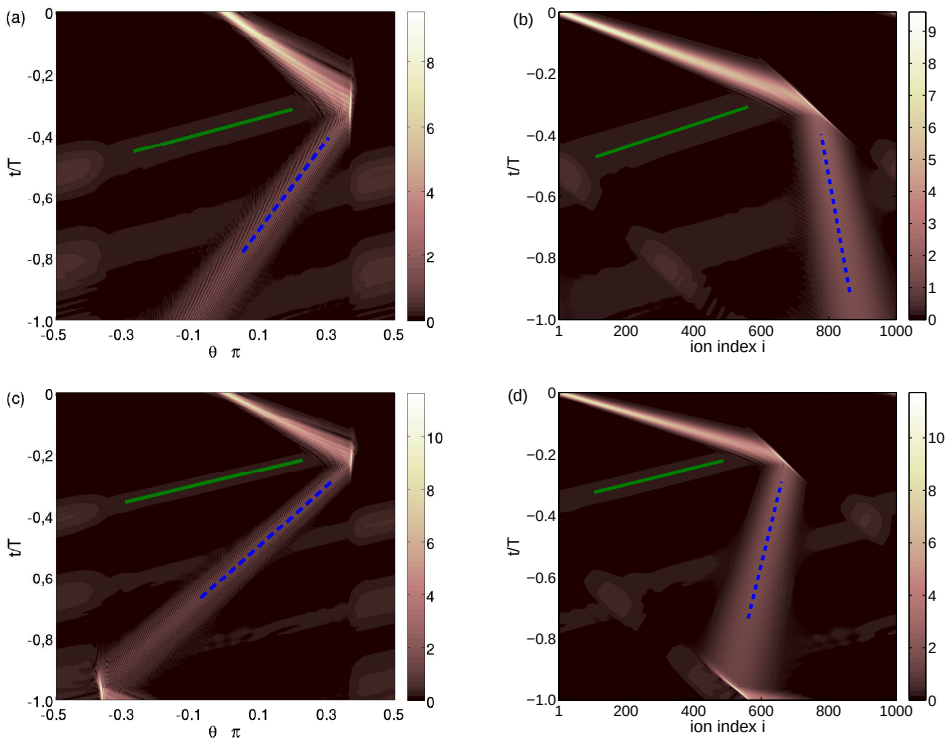

Figure 4.6: Ion displacement $|\delta\theta_i(t)/(2\pi)|$ during propagation backwards in time starting from the final wavefunction in Eq. (4.62) with $s = 5$. One late-time pulse and three (two of which overlapp) early-time pulses are present (see text). Two early-time pulses have large absolute momenta (blue dashed lines), one early-time pulse has small momentum (green straight lines). We use $\sigma v_{\min} T = 0.375$ and $N = 1000$. For (a) and (b) $e^2/4\pi\epsilon_0 = \frac{1.2591}{2N}\frac{mL^3}{T^2}$, for (c) and (d) $e^2/4\pi\epsilon_0 = \frac{2.0004}{2N}\frac{mL^3}{T^2}$ (see Appendix A.2). (a) and (c) use lab frame angles θ, (b) and (d) use ion indices i (see text for description of scattering process).

the deviations from a linear dispersion relation at small wavenumbers are significant in a finite system.

Our results agree mainly with those of references [Unr95, CJ98, JM99] as shown in Fig. 4.7. First, we observe quantitative devisions, whose order of magnitude agrees with the uncertainties in calculating the Hawking temperature. Second, we find a previously undescribed downstream pulse at small negative frequencies. But before discussing the detailed analysis

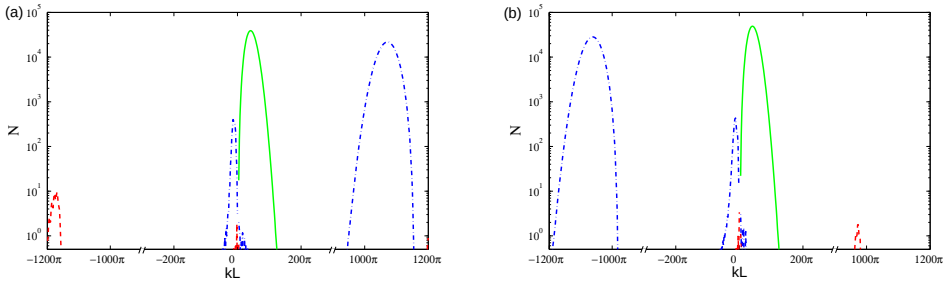

Figure 4.7: Klein-Gordon norm $\mathcal{N}_k$ of the phonon pulses for propagation backwards in time starting from the final wavefunction in Eq. (4.62) with $s = 5$. With a comparison of these pulses we test the thermal hypothesis. We use $\sigma v_{\min} T = 2\pi \cdot 0.375$, and $N = 1000$ (see Appendix A.2). The final negative frequency pulses are depicted in green, the initial negative frequency pulses in blue (dash-dotted line), and the initial positive frequency pulses in red (dashed line). We depict the discrete norm distributions/dispersion relation as a continuous curve here. (a) Final ($t = 0$) and initial ($t = -0.67T$) norm distribution of $\delta\theta_k(t)$; $e^2/4\pi\epsilon_0 = 1.2591/(2N) \cdot mL^3T^{-2}$. (b) Final ($t = 0$) and initial ($t = -0.51T$) norm distribution of $\delta\theta_k(t)$ showing Bloch oscillation; $e^2/4\pi\epsilon_0 = 2.0004/(2N) \cdot mL^3T^{-2}$ [HRF+10].

of the scattering process, we will repeat the description of the mode conversion from Sec. 4.3.2, but this time illustrated in real space with the simulation results from the special case of the ion ring (see Fig. 4.6).

We begin with the normal scenario of sufficiently large ion velocities (see Figs. 4.6(a)-(b) and 4.7(a)). We observe all three early-time pulses which are in agreement with frequency conservation. Two pulses are located on the upstream branch at high absolute wavenumbers (red and blue lines in Fig. 4.7(a)). But at these wavenumbers they have such a small group velocity in the comoving frame that they are moving rightwards in the lab frame (blue dashed lines in Figs. 4.6(a)-(b)). A third pulse is located on the downstream branch of the dispersion relation at small negative wavenumbers (blue line in Fig. 4.7(a)). Its group velocity is large both in the comoving frame and in the lab frame. This time evolution is depicted in Fig. 4.6(a) in the lab frame and in Fig. 4.6(b) in the comoving frame. The two upstream and the one downstream pulse can clearly be identified in the comoving frame. In the lab frame the downstream pulse

is quickly moving rightwards, the two upstream pulses are slowly moving rightwards.

A different situation arises for sufficiently small ion velocities (see Figs. 4.6(c)-(d) and 4.7(b)). In this case, all three early-time pulses are moving downstream. This time evolution is depicted in Fig. 4.6(c) in the lab frame and in Fig. 4.6(d) in the comoving frame. In the comoving frame we can now observe the three downstream pulses, one fast pulse which is the one at low wavenumbers (green lines) and the two interesting slow pulses (red dashed lines) which are still located at high absolute wavenumbers. In the lab frame the two pulses at high absolute wavenumbers are travelling faster than in the normal case.

The spectral analysis in Fig. 4.7 confirms these explanations. We find the two previously mentioned high wavenumber pulses. For small ion velocities the effect analogous to Bloch oscillations is observed. Then the main incoming pulses have wavenumbers with opposite signs. In addition we observe the weak downstream pulse with small negative wavenumbers that is not desribed in the literature. We find that its magnitude depends on the strongly on how the fringes of the pulse in outside the flat subsonic region are treated. Therefore we suggest that the presence of this pulse could be a consequence of the finite initial and final excitation probability of ions outside the flat subsonic region.

We further compare the Klein-Gordon norm of the positive frequency early-time pulse with the prediction for thermal radiation (see Sec. 4.3.2 and [Unr95, JM99]). We calculate the Hawking temperature according to Eq. (4.18). If only nearest-neighbor Coulomb interactions are considered, the relative difference between these norms is lower than $\epsilon = 0.01$ for $N = 1000$ ions. For the long range Coulomb interactions a conservative estimate yields $\epsilon \leq 0.2$. The latter result holds for any arbitrary choice for the Hawking temperature at the wavenumbers $k = 2\pi/L \cdot 4 \ldots 6$. The bound on ϵ agrees with the differences between analysis based on the group and the phase velocity of the phonons (see Sec. 4.2.2 and Eq. (4.10)).

We also perform the analogous spectrally dissolved comparison (see Sec. 4.3.2 and [Unr95]), comparing the early-time positive frequency pulse with the prediction based on the thermal hypothesis. Only discrete frequencies appear in the system because only discrete wavenumbers are present. Therefore, it is in general not possible to exactly match the frequencies of the pulses. Especially, we cannot perform a thermal fit. Thus, we look at the two frequencies in the early-time pulses closest to the frequencies in the late-time pulse. We compare the early-time posi-

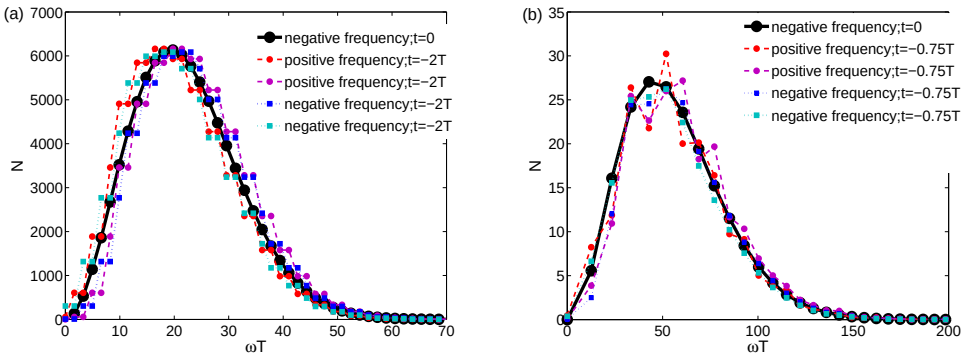

Figure 4.8: Comparison of spectrally resolved Klein-Gordon norms $\widetilde{\mathcal{N}}_k^0$ (late-time negative frequency pulse) at $t = 0$ with $\widetilde{\mathcal{N}}_k^+$ (early-time positive frequency pulse) and $\widetilde{\mathcal{N}}_k^-$ (early-time negative frequency pulse) (see Sec. 4.3.2) as a function of the lab frame frequencies at $t = -2T$ after propagation backwards in time starting from the final wavefunction in Eq. (4.62) with $s = 5$. We use $\sigma v_{\min} T = 0.375$, $N = 1000$. (a) Nearest-neighbor interactions at $t = -2T$ with $e^2/4\pi\epsilon_0 = \frac{1}{2N}\frac{mL^3}{T^2}$; (b) Full Coulomb interactions at $t = -0.75T$ with $e^2/4\pi\epsilon_0 = \frac{1}{2N}\frac{mL^3}{T^2}$ (see Appendix A.2).

tive frequency pulse $\widetilde{\mathcal{N}}_k^+$ with the predictions for it based on the late-time negative frequency pulse $\widetilde{\mathcal{N}}_k^0$ and based on the early-time negative frequency pulse $\widetilde{\mathcal{N}}_k^-$ (see (4.41)-(4.43)). The result of this analysis is shown in Fig. 4.8(a) for nearest-neighbor interactions and in Fig. 4.8(b) for full Coulomb interactions. For this analysis we choose the Hawking temperature at $k = 2\pi/L \cdot 5$ (see Eq. (4.18)), but similar results are obtained for the adjacent wavenumbers). This analysis again confirms the thermal hypothesis to the extend possible. The accuracy of our analysis is restricted by the discreteness of the system and the nonlinearity of the dispersion relation at small wavenumbers.

We summarize the findings of this section: Hawking radiation with a thermal spectrum is emitted from a black hole horizon on an ion ring, even for a finite system with a logarithmically diverging group velocity at low wavenumbers due to long-range interactions (see Fig. 4.3).

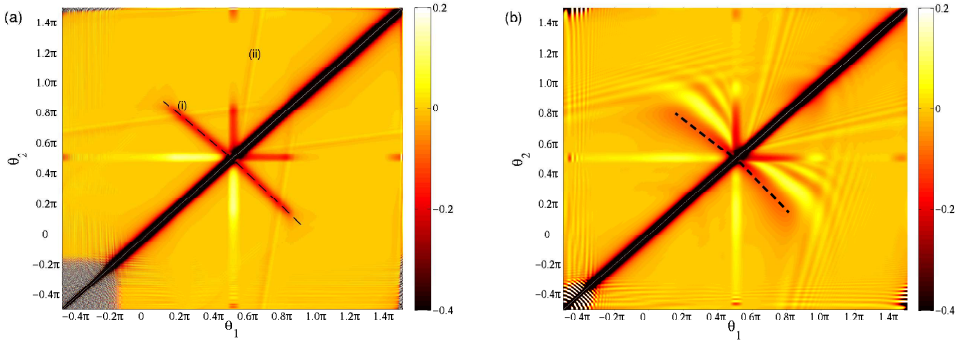

Figure 4.9: Momentum-momentum correlations $C_{ij}(t)$ at time $t = 0.5T$ with real space lab frame positions. Starting from homogeneously spaced ions with temperature $T_0 = 0$ a black hole region is created in the small time interval $\tau = 0.05T$. The dashed lines point to the signature corresponding to the emission of pairs of Hawking phonons. We consider $N = 1000$ ions, and $\sigma v_{\min} T = 2\pi \cdot 0.25$. (a) Nearest-neighbor interactions with $e^2/4\pi\epsilon_0 = \frac{1.127}{2N}\frac{mL^3}{T^2}$; (b) Full Coulomb interactions with $e^2/4\pi\epsilon_0 = \frac{0.2453}{2N}\frac{mL^3}{T^2}$ [HRF$^+$10] (see Appendix A.2).

4.4.2 Correlations

For an experimental proof of Hawking radiation on ion rings, we propose to observe the emission of Hawking radiation following the creation of a black hole horizon (see Sec. 4.5). We propose to measure the emitted phonons or the emerging correlations between the subsonic and the supersonic region (see [BFF$^+$08, CFR$^+$08, MP09a]). The latter is discussed in Sec. 4.3.3, in this section we are presenting simulation results for ion rings on the emerging correlations. We compare our results to the analytical findings for a continuum system with linear dispersion relation derived in Eq. (4.57) [BFF$^+$08]. In the quantum regime the emergent cross-correlations display the generation of entanglement. We study its properties, especially to analyze the crossover from the quantum to the classical Hawking effect.

Discrete System

We propose the experiment to start from the ground/thermal state of the excitation around homogeneously spaced ions at rest with temperature

T_0. Then the system is accelerated with a constant force which does not change the quantum state of the system defined relative to the equilibrium positions. Subsequently, a supersonic region is created in the small time interval τ. This is done by reducing the subsonic fluid velocity $v_{\min}$ in a Gaussian way, while leaving the average rotation velocity constant (see Appendix A.2 and Eq. (A.9)). We reduce excitations created at the white hole horizon at $\theta/2\pi \approx 1 - \sigma v_{\min} T$ by a wider transition region at this horizon. In an experiment the magnitude and velocity of these excitations can be watched through careful measurements.

We are analyzing the momentum-momentum correlations

$$C_{ij} = \langle \delta\hat{p}_i \delta\hat{p}_j \rangle \cdot T/(\hbar m). \tag{4.64}$$

In the continuum limit these momenta correspond to the time derivative of the scalar field $\hat{\Phi}$

$$\delta\hat{p}_i \sim (\partial_t + v(\theta)\partial_\theta)\, \hat{\Phi}(\theta, t). \tag{4.65}$$

The dynamics of the momentum-momentum correlations are given by the dynamics of the covariance matrix (see Eq. (A.13)). In Sec. 4.5.1 we are explaining how these correlations C_{ij} can be measured in an experiment.

Fig. 4.9 shows the simulation results for C_{ij}. It displays a fixed time after the black hole formation starting from the ground state, i.e., $T_0 = 0$. Correlations between the inside and the outside of the black hole are created close to the black hole horizon and are moving away from it as expected. As stated earlier these correlations correspond to the pairs of Hawking particles. We interpret their pure existence as a signature for Hawking radiation. Fig. 4.9(a) shows the simulation for interactions between neighboring ions only, Fig. 4.9(b) for long range Coulomb interactions. The correlations behave similarly in both cases (see discussion below). They can still be observed for initial temperatures two orders of magnitude above the Hawking temperature [BFF+08, CFR+08, MP09a] as shown in Fig. 4.10. In Sec. 4.4.2 we find that the Hawking effect is still quantum at such initial temperatures (see Fig. 4.14). In contrast to the entanglement, the cross-correlations actually remain present at arbitrarily large initial temperatures [FCB+10] (note $\Gamma \propto T_0$ for $k_B T_0 \gg \omega_k$, see Eq. (A.18)).

The most significant correlation signal (i), i.e., the line of negative cross-correlations, demonstrates a basic property of Hawking radiation, it corresponds to two upstream phonons, one inside and one outside the

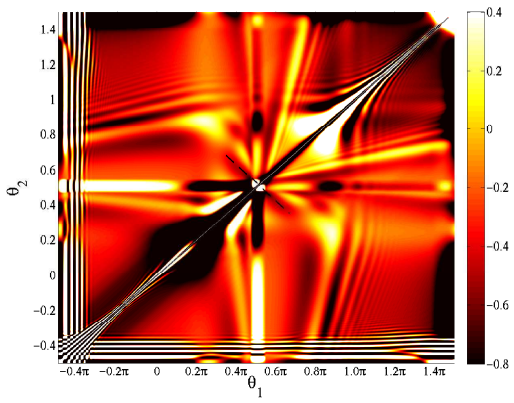

Figure 4.10: Momentum-momentum correlations $C_{ij}(t)$ for initial temperature $T_0 = 102T_{\rm H}$ at time $t = 0.5T$ with real space lab frame positions. We consider $N = 1000$ ions, $\sigma v_{\rm min} T = 2\pi \cdot 0.25$, $e^2/4\pi\epsilon_0 = \frac{0.2453}{2N}\frac{mL^3}{T^2}$, and $\tau = 0.05T$. Full Coulomb interactions are considered (compare with Fig. 4.9).

black hole. An additional correlation feature (ii) is fully inside the black hole, corresponding to a pair of upstream and downstream phonons inside the black hole. The features (i) and (ii) have already been reported for analog black holes in a BEC (see [BFF+08]). The propagation velocity of these correlations $c(\theta) \pm v(\theta)$ depends on the group velocity, i.e., the dispersion relation, and the ion velocity. The angle of the cross-correlation signature (i) is determined by the ratio of the phonon velocities inside and outside of the black hole $(c(\theta) - v(\theta)) \,/\, (c(\theta') - v(\theta'))$. The dashed lines in Fig. 4.9 show the predictions for the direction of the cross-correlation signal (see Sec. 4.3.3).

In contrast to Fig. 4.9, which is very similar to black hole analogues in a BEC [BFF+08], the correlation plot for full Coulomb interactions in Fig. 4.9(b) displays a more complicated structure. The cross-correlation signal, is broader and there are additional lines of oscillating correlations. With higher resolution and/or for larger Hawking temperatures these effects can also be observed for nearest-neighbor interactions. We attribute these changes to the more complicated and sublinear dispersion relation.

Even though the precise determination of the correlations for a nonlinear dispersion relation is a rather complicated issue (see, e.g., [SU10]), we

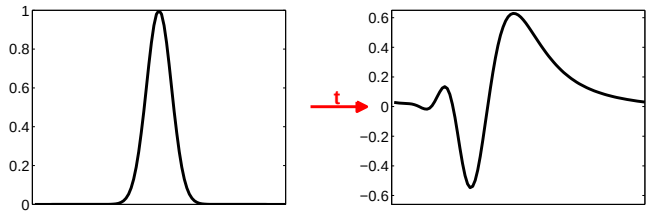

Figure 4.11: Schematic depiction of the pulse propagation on an ion ring. The left graph depicts an initial Gaussian pulse profile, the right graph the dispersed pulse after time t. Trails of oscillations are following the dispersed pulse.

may obtain a qualitative understanding by means of the following simple picture. Since group and phase velocity nearly coincide at small wavenumbers, the correlations are created near the horizon as a nice $1/\cosh^2$-pulse as in the case of a linear dispersion relation (see Eq. (4.57)).

However, as this pulse propagates away from the horizon, the nonlinear dispersion relation deforms it. For a fixed t', θ', the two-point function $\langle \delta\hat{p}(t,\theta)\delta\hat{p}(t',\theta')\rangle$ obeys the same wave equation as $\delta\hat{p}(t,\theta)$ itself. In a homogeneous region of a stationary spacetime this is the same as for the field Ψ (see Eq. (4.20)).

$$\left\{[\partial_t + \partial_\theta v]\,[\partial_t + v\partial_\theta] - [iD\,(-i\partial_\theta)]^2\right\}\langle \delta\hat{p}(t,\theta)\delta\hat{p}(t',\theta')\rangle = 0. \qquad (4.66)$$

Since modes with larger k propagate slower than those with smaller k, a pulse with an initial $1/\cosh^2$-shape will be deformed during the time evolution similar to Fig. 4.11. The main pulse (global maximum) becomes broader and oscillations develop, trailing the main pulse (local minima and maxima), which are caused by the slower modes with short wavelengths. This deformation applies to the outgoing Hawking radiation and the infalling partners in the same way as both are moving upstream. In a finite system the deviations from a linear dispersion are significantly larger for full Coulomb interactions than for nearest-neighbor interactions. As a result, this simple picture explains the difference between Figs. 4.9(a) and 4.9(b).

Comparison with Continuum System

In Sec. 4.3.3 we have calculated and analyzed the cross-correlation signal for a continuum system with strictly linear dispersion relation. We observe these correlations also for our discrete system with sublinear dispersion relation as shown in Fig. 4.9. In this Section we are quantitatively comparing the simulation results for ion rings with the analytical results for a continuous system, focussing on the peak magnitude of the cross-correlations (see Eq. (4.57)).

We perform this comparison for varying Hawking temperatures. It is tuned by changing the widths of the horizon region γ_1 (see Eq. (A.8)) keeping constant the other parameters. The comparison is shown for nearest-neighbor interactions in Fig. 4.12(a) and for full Coulomb interactions in Fig. 4.12(b), where the dots represent the simulated peak magnitude for the ion ring and the curve represents the analytic peak magnitude for the continuum system with a linear dispersion relation.

At small Hawking temperatures, the results agree very well for nearest-neighbor interactions, also for full Coulomb interactions the agreement is quite good for moderate Hawking temperatures. The deviation at large Hawking temperatures is caused by the discreteness of the system. For large Hawking temperatures the horizon region, which almost completely determines the properties of Hawking radiation, is small and contains only a few particles. Then the discreteness of the system becomes relevant. In the limit of very large Hawking temperatures the peak height should mainly depend on the lattice spacing [FCB+10].

Entanglement Generation

In this section we are discussing the creation of entanglement between the inside and the outside of a black hole following its creation. Entanglement is unique to quantum processes. Therefore, the existence of entanglement proves that one can observe the quantum version of the Hawking effect with our proposal. In contrast, correlations between the inside and the outside of the black hole are present both for initial thermal states $T_0 \gg T_\mathrm{H}$ in the *classical* regime and for initial *quantum* states $T_0 = 0$ [FCB+10]. So we analyze the crossover between classical and quantum Hawking radiation (stimulated versus spontaneous emission). Furthermore, our analysis emphasizes the importance we assigned to the cross-correlations. The emerging entanglement can be measured on two routes, either by measur-

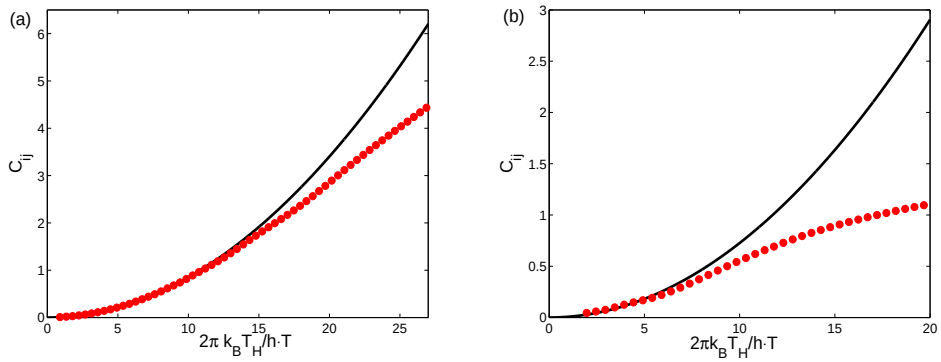

Figure 4.12: Peak Height $C_{ij}(t)$ of the cross-correlation signature in the momentum-momentum correlations (see Fig. 4.9) as a function of the Hawking temperature T_{H}. The dots are simulation results for a discrete system with nearest-neighbor interactions only, $N = 1000$ ions, $\sigma v_{\mathrm{min}} T = 2\pi \cdot 0.25$, and $\tau = 0.05T$. γ_1 is varied to get different Hawking temperatures T_{H}. $h = 2\pi\hbar$ is Planck's constant. (a) Nearest-neighbor interactions with $e^2/4\pi\epsilon_0 = \frac{1.127}{2N}\frac{mL^3}{T^2}$ and $0.00\bar{3} < \gamma_1 < 0.1$; (b) Full Coulomb interactions with $e^2/4\pi\epsilon_0 = \frac{0.2453}{2N}\frac{mL^3}{T^2}$, and $0.005 < \gamma_1 < 0.1$ (see Appendix A.2).

ing the covariance matrix through a measurement of correlation in the ion displacements (see Sec. 4.5.1) or by swapping the entanglement from the motional to the internal degrees of freedom of the ions [RCB05].

We are now briefly introducing the relevant entanglement measures before we present numerical results for the ion system. The covariance matrix Γ (see Eq. (4.8)) can be calculated (see Appendix A.3) and measured (see Sec. 4.5) for the ion system in harmonic approximation (see Eq. (4.5)). It gives access to two entanglement measures: the entropy of entanglement and the logarithmic negativity.

We consider a system with density matrix ρ divided into subsystems A and B. The entropy of entanglement is defined for a bipartite pure state. It is the Von-Neumann entropy of the reduced density matrix ρ_A of one subsystem A [BBP+96]

$$\mathbf{S}(\rho) = -\mathrm{tr}\left(\rho_{\mathrm{A}} \log_2 \rho_{\mathrm{A}}\right). \tag{4.67}$$

The state ρ is a product state for $\mathbf{S}(\rho) = 0$. As an entanglement measure $\mathbf{S}$ cannot increase under local operations and classical communications

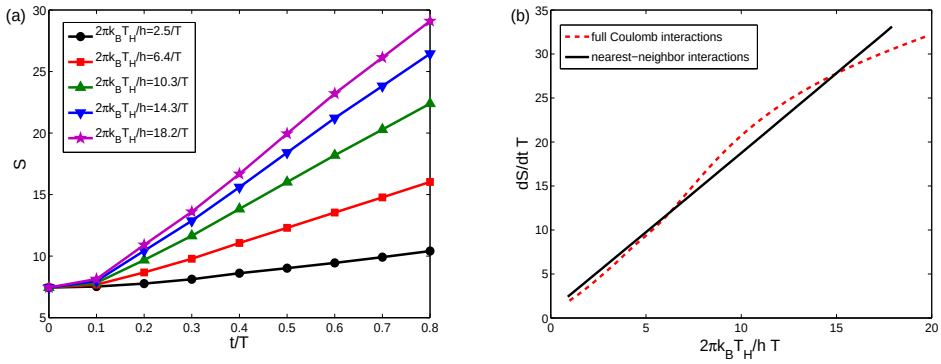

Figure 4.13: (a) Time evolution of the entropy of entanglement $\mathbf{S}(\Gamma)$ for different Hawking temperatures T_H with full Coulomb interactions (same parameters as Fig. 4.12(b)). (b) Rate of increase of the entropy of entanglement $d\mathbf{S}(\Gamma)/dt$ as a function of the Hawking temperature T_H. Full Coulomb interactions (red dashed line, same parameters as Fig. 4.12(b)), and nearest-neighbor interactions (black straight line, same parameters as Fig. 4.12(a)). The linear increase in entanglement is caused by the constant emission of entangled Hawking phonons.

(LOCC). For pure Gaussian states $\mathbf{S}(\rho)$ can efficiently be calculated from the covariance matrix Γ [VW02, BR03, WGK+04]. It is given by

$$\mathbf{S}(\Gamma) = \sum_{n=1}^{N} \left(\lambda_n^2 \log_2 \lambda_n^2 - (\lambda_n^2 - 1) \log_2 \left(\lambda_n^2 - 1\right)\right) \tag{4.68}$$

with the symplectic eigenvalues $\lambda_n,\ n = 1, \ldots, N$ of the covariance matrix Γ. They are the eigenvalues of $i\sigma\Gamma$ with the symplectic matrix

$$\sigma = \bigoplus_{n=1}^{N} \begin{pmatrix} 0 & 1 \\ -1 & 0 \end{pmatrix}, \tag{4.69}$$

which exchanges position and momentum of each mode.

We can also use the logarithmic negativity, which is an entanglement monotone, i.e., it does not decrease under LOCC [VW02]. In contrast to the entropy of entanglement, it can be calculated efficiently from the covariance matrix even for mixed states. It is defined as the logarithm of the trace-norm of the partial transpose of the density matrix

$$\mathbf{N}(\rho) = \log_2 \|\rho^{T_a}\| \tag{4.70}$$

with $\|M\| = \sqrt{M^\dagger M}$. The covariance matrix Γ^{T_a} of the partial transpose of ρ, i.e., ρ^{T_a}, follows from the covariance matrix Γ of ρ by multiplying with -1 all matrix entries of Γ which contain exactly one momentum operator of subsystem A. Let $\widetilde{\lambda_k},\ k = 1, \ldots, N$ denote the symplectic spectrum of Γ^{T_a}. Then the logarithmic negativity is

$$\mathbf{N}(\Gamma) = -\sum_{\substack{n=1 \\ 2\widetilde{\lambda_n}<1}}^{N} \log_2\left(2\widetilde{\lambda_n}\right). \tag{4.71}$$

A vanishing logarithmic negativity does not mean that the system is not entangled, but it means that such systems cannot be purified to maximally entangled states.

Now, we analyze the entanglement properties for black holes on ion rings. Using the entropy of entanglement we study how the entanglement is generated between the inside and the outside of a black hole starting from the ground state ($T_0 = 0$) at initial times. The entropy of a black hole is more fundamental than the logarithmic negativity, but it is only defined for pure states. Thus, we have to compare the whole supersonic with the whole subsonic region. On a ring this means that one cannot determine at which horizon the entanglement is created.

In Fig. 4.13(a) we find a linear increase of the entropy of entanglement in time after an initial period ($t \sim 0.2T$ in our case). This linear increase corresponds to the constant emission of Hawking radiation from a black hole. We have plotted the rate of this increase in Fig. 4.13(b). We find for nearest-neighbor interactions a linear dependence of the entropy of entanglement on the Hawking temperature of the black hole. For full Coulomb interactions we find a similar behavior.

The logarithmic negativity gives access to the entanglement developing for systems with finite initial temperatures $T_0 > 0$. The entanglement between two small regions adjacent to the black hole is presented in Fig. 4.14. The initial entanglement between the regions depends on the system temperature: For quantum systems at $T_0 = 0$ entanglement is present, for classical systems $T_0 \to \infty$ it cannot be detected. The entanglement is increasing linearly in time for sufficiently small T_0. This behavior is already described above for the entropy of entanglement (see Fig. 4.13(a)).

However, the logarithmic negativity allows further observations. For initial temperatures T_0 more than two orders of magnitude above the Hawking temperature T_H, no entanglement generation is visible in the

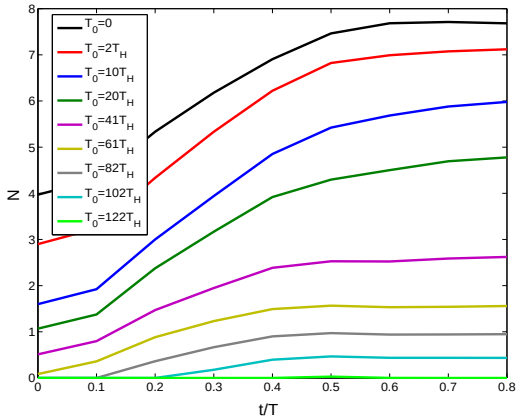

Figure 4.14: Time evolution of the logarithmic negativity **N** of a region with $0.2N$ ions ($N = 1000$) adjacent to the horizon for different initial temperatures T_0. The linear increase in entanglement is caused by the constant emission of entangled Hawking phonons. Full Coulomb interactions considered (same parameters as Fig. 4.9(b)).

logarithmic negativity. In contrast, the cross-correlation signal remains present for arbitrarily high initial temperatures. We observe here the transition from the *quantum* to the *classical* Hawking effect. We can conclude that for the initial temperatures $T_0 < T_0^{\mathrm{c}} \approx 100 T_{\mathrm{H}}$ ($N = 1000$) the observed Hawking effect is quantum, whereas one would naively expect this transition at $T_0^{\mathrm{c}} \approx T_{\mathrm{H}}$. $T_0^{\mathrm{c}}/T_{\mathrm{H}}$ is increasing with the number of ions, taking, for example, $N = 100$ ions and $e^2/4\pi\epsilon_0 = 0.6/(2N) \cdot (mL^3)/T^2)$ we find $T_0^{\mathrm{c}} \approx T_{\mathrm{H}} \approx 24$. $T_0^{\mathrm{c}}/T_{\mathrm{H}}$ is approximately proportional to the largest mode frequency of the system, which is sublinear in in N.

This might be understood with the following argument: As described in Sec. 4.3.2 Hawking radiation emerges from large wavenumbers before being emitted at small wavenumbers. The frequency related to these large wavenumbers is about N-times (number of ions) higher than the smallest frequency in the system. Along this line, the Hawking effect remains quantum for initial temperatures comparable to these highest frequencies of the system at large wavenumbers.

In Fig. 4.14 a saturation in the logarithmic negativity at later times is observed. This is in agreement with the fact that Hawking radiation is constantly emitted. After fully penetrating the small regions adjacent

to the horizon, no additional entanglement can develop between these regions.

4.5 Experimental Realization

So far we have studied the appearance of Hawking radiation on ion rings. We have demonstrated that the emitted radiation has a thermal spectrum with a geometrically justified Hawking temperature (see Sec. 4.4.1), and that it is created in pairs (see Sec. 4.4.2). We complete our analysis in this section by describing an experimental setup which will allow for the observation of Hawking radiation on an ion ring.

First, we present a suitable parameter regime for an experiment. The main condition on the experimental parameters is that the ion velocity must be approximately equal to the phonon velocity. This condition leads to the requirement $e^2/4\pi\epsilon_0 \approx 0.25/(2N)\, mL^3/T^2$. For $N = 1000$ singly charged ^9Be ions with an average spacing of $L/N = 2\mu m$ the rotation frequency of the ions would be $\omega_{\mathrm{rot}} = 2\pi \times 120kHz$. ω_{rot} represents the smallest mode frequency of the system. For $v_{\mathrm{min}} = (2\pi \times 0.8\bar{3})/T$, $\gamma_1 = 0.02$, and $\sigma v_{\mathrm{min}} T = 2\pi \cdot 0.25$ the Hawking temperature is $k_{\mathrm{B}}T_{\mathrm{H}}/\hbar \approx 5/T \approx 2\pi \times 95kHz$. If the initial temperature is two orders of magnitude above the Hawking temperature $T_0 \lesssim 100T_{\mathrm{H}}$, we show explicitly in Sec. 4.4.2 that the cross-correlation signature of Hawking radiation remains present (see Fig. 4.10) and we find in Sec. 4.4.2 that the Hawking radiation remains a quantum effect. Thus, it is not necessary to perform ground state cooling of all vibrational modes of the ions in an experiment.

Note that it has been demonstrated long ago how to trap ions in quadrupole ring traps [DP64, Chu69, DJA$^+$88] and measure their arrangement [BKW92, WKB$^+$92, SSH01]. The ideas of these experiments can be combined with modern cooling techniques applied to ions in linear Paul traps or in surface traps [EMK$^+$03, HHJ$^+$10]. Thus, the proposed experiment will allow to measure signatures of Hawking radiation for acoustic black holes with parameters and temperatures which can be reached in current experiments.

The general idea of the actual measurement process is the following. The Hawking effect is encoded in the motional degrees of freedom of the ions, which are described in this chapter with the ion displacements $\delta\theta_i$ and can be viewed as phonic modes. A different degree of freedom for ions is their internal state, here we address two hyperfine states of the ions.

Lasers couple the motional degrees of freedom to the two relevant internal states. In this way, the information on the Hawking effect is transfered to the internal states. The occupation of the internal states can be read out by fluorescence imaging.

In Sec. 4.5.1 we first propose a measurement sequence for the cross-correlation signature. Then we discuss a proposal to directly measure the Hawking phonons in Sec. 4.5.2. The proposal in Sec. 4.5.1 allows to determine any part of the covariance matrix (see Eq. (4.8)). Thus, it can be used to determine the emerging entanglement between the inside and the outside of the black hole (see Sec. 4.4.2). Note that it has been proposed earlier how to detect entanglement in the motional degrees of ions [RCB05]. The basic mechanism of all proposals is the coupling of the ion displacements to their internal levels with lasers.

4.5.1 Measurement of Ion Displacements

In this section we discuss how the cross-correlation signal analyzed in Sec. 4.4.2 can be detected in an experiment. We propose to measure correlations in the ion displacements by coupling the motional degrees of freedom of the ions to their internal states.

First, we explain how to relate the momentum-momentum correlations we discussed (see Eq. (4.64)) to experimentally accessible correlations in the ion displacement and analyze how accurately the latter should be measured. To this aim we rewrite Eq. (4.56) for a continuum system in a region of constant flow as

$$\delta\hat{p}(\theta) = \frac{L}{2\pi} mc(\theta)n(\theta)\frac{\partial_\theta \hat{\Phi}(\theta,t)}{n(\theta)}. \tag{4.72}$$

We can thus measure the momentum-momentum correlations by spatial derivatives of the ion displacements

$$\left\langle \left(\delta\hat{\theta}_i - \delta\hat{\theta}_{i+\Delta}\right)\left(\delta\hat{\theta}_j - \delta\hat{\theta}_{j+\Delta}\right)\right\rangle = \left(\frac{2\pi}{mL}\right)^2 \frac{\Delta^2}{n_i n_j c_i c_j}\langle \delta\hat{p}_i \delta\hat{p}_j\rangle. \tag{4.73}$$

The analysis shown in Fig. 4.12(b) confirms that we can use Eq. (4.57) to get the order of magnitude of the momentum-momentum correlations for a finite ion ring. Thus, we can estimate the magnitude of the cross-

correlation signature as

$$\left\langle \left(\delta\hat{\theta}_i - \delta\hat{\theta}_{i+\Delta}\right)\left(\delta\hat{\theta}_j - \delta\hat{\theta}_{j+\Delta}\right)\right\rangle \approx \left(\frac{2\pi}{L}\right)^2 \frac{\hbar T}{m}\frac{\pi^3\Delta^2}{N^3}\frac{\left(k_{\mathrm{B}}T_{\mathrm{H}}/\hbar\right)^2}{(c_i - v_i)(c_j - v_j)}, \tag{4.74}$$

where we used $n_i \approx n_j \approx N/(2\pi)$ and $c_i \approx c_j \approx (2\pi)/T$. Therefore, the angle-angle correlations must be detected in an experiment with the accuracy

$$\epsilon := \Delta\langle\delta\hat{\theta}_i\delta\hat{\theta}_j\rangle = \left(\frac{2\pi}{L}\right)^2 \frac{\hbar T}{m}\frac{\pi^3\Delta^2}{4N^3}\frac{\left(k_{\mathrm{B}}T_{\mathrm{H}}/\hbar\right)^2}{(c_i - v_i)(c_j - v_j)}. \tag{4.75}$$

In the following we are describing a setup to detect the angle-angle correlations of the ions with sufficient accuracy. We propose to illuminate the ion ring at two positions. The lasers should be focussed on one ion inside the supersonic and one ion inside the subsonic region on the ring. At each position a laser beam couples two internal levels $\left|g\right\rangle$ and $\left|e\right\rangle$ of the ions with the transition energy ω_I. The lasers should fullfill the resonance conditions

$$\omega = \omega_I + kv\frac{L}{2\pi} \tag{4.76}$$

relating their frequencies and wavenumbers, which takes into account the Doppler shift kv. The ion traverses the pulse beam in the time T/N which is much shorter than the time scale $T = 2\pi/\omega_{\mathrm{rot}}$ of phonons at small wavenumbers. Thus, we can neglect the ion motion for the further analysis. After going to the frame rotating with ω_0 and applying the rotating wave approximation the dipolar coupling Hamiltonian [WMI+98] of one illuminated ion becomes

$$\mathcal{H}_{dip} = \hbar\Omega\left(\sigma^+ e^{\frac{ikL}{2\pi}\delta\hat{\theta}} + H.c.\right), \tag{4.77}$$

where Ω is the Rabi frequency of the laser transition. Note that the ions remain in the Lamb-Dicke limit

$$\sqrt{\frac{\hbar}{mN\omega_{\mathrm{rot}}}}k \ll 2\pi \tag{4.78}$$

during the experiment, i.e., $kL\delta\hat{\theta} \ll 4\pi^2$.

We propose to prepare the internal state of each ion in the superposition $(\left|g\right\rangle + \left|e\right\rangle)/\sqrt{2}$ before the experiment. After the creation of the

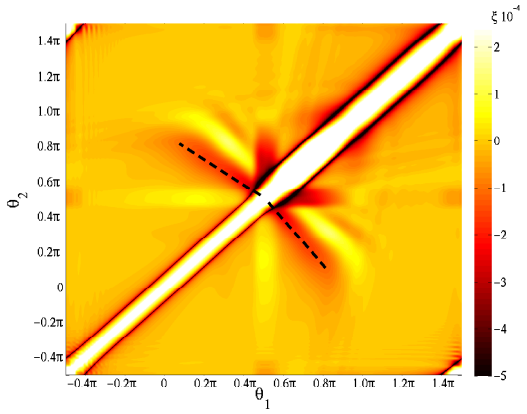

Figure 4.15: Correlations $\langle(\delta\hat{\theta}_i - \delta\hat{\theta}_{i+50})(\delta\hat{\theta}_j - \delta\hat{\theta}_{j+50})\rangle \cdot m/(\hbar T) \cdot L^2/(2\pi)^2$ at time $t = 0.6T$ with real space lab frame positions. These correlations are analougous to the momentum-momentum correlations shown in Fig. 4.9b. We consider $N = 1000$ ions, $\sigma v_{\min} T = 2\pi \cdot 0.25$, $e^2/4\pi\epsilon_0 = \frac{0.2453}{2N}\frac{mL^3}{T^2}$, and $\tau = 0.05T$. Full Coulomb interactions are considered.

black hole and the illumination with the lasers the probability that the two measured ions are in the states $\left|gg\right\rangle$ or $\left|ee\right\rangle$

$$P\left(\delta\hat{\theta}_1, \delta\hat{\theta}_2\right) = \frac{1}{2} + \left(\frac{L}{2\pi}\right)^2 \sin^2\left(2\Omega t\right) \frac{k^2}{2} \langle \delta\hat{\theta}_1 \delta\hat{\theta}_2 \rangle \tag{4.79}$$

is measured through a repetition of the experiment. We propose to use the Rabi frequency $2\Omega t = \pi/2$. If the measurement is repeated M times, the standard deviation of the average number of binomially distributed events P is

$$\Delta P = \sqrt{\frac{P(1-P)}{M}} \approx \frac{1}{2\sqrt{M}}. \tag{4.80}$$

It should be smaller than the required accuracy of the signal size and thus

$$M > \left(\frac{2\pi}{L}\right)^4 k^{-4} \epsilon^{-2} \approx \left(\frac{m\omega_{\text{rot}}}{\hbar k}\right)^2 \left[\frac{2N^3}{\Delta^2 \pi^4} \frac{(c_i - v_i)(c_j - v_j)}{(k_{\text{B}} T_{\text{H}}/\hbar)^2}\right]^2 \tag{4.81}$$

measurements are necessary.

We are now calculating M for the example of $N = 1000$ ^9Be ions, discussed in the beginning of this Sec. 4.5. We propose to use the $\lambda =$

$313nm$ transition in ^9Be [MMK+95]. We have checked that the cross-correlations remain clearly visible for the resolution $\Delta = 50$ (see Fig. 4.15). In this case $M > 1.1 \cdot 10^5$ measurements are required. This basic measurement proposal can certainly be improved by employing additional techniques, e.g., using interferences with additional lasers. But we do not propose further experimental setups here since these should be adopted to specific implementations of our proposal.

The accuracy of the classical equilibrium positions of the ions must satisfy $|\Delta\theta_i^0|^2 < \sqrt{\epsilon}$, such that it does not influence the cross-correlation signal. Inaccurate equilibrium positions can be caused by inaccurate external forces (see Appendix A.1) during the black hole formation. Assuming that the external force is $\widetilde{F}_i(t) = (1+\gamma)F_i(t)$ (see Eq. (A.3)) with $\gamma \ll 1$, the deviation in the classical positions fullfills the equation

$$\frac{L}{2\pi} m \frac{d^2\Delta\theta_i}{dt^2} = \gamma F_i(t). \tag{4.82}$$

Integrating Eg. 4.82, we can estimate

$$\begin{aligned} \frac{|\Delta\theta_i|}{\gamma} &< \left| \theta_i^0(\tau) - \theta_i^0(0) - \frac{d\theta_i^0(0)}{dt}\tau \right| + \frac{\tau^2}{2}\frac{2\pi}{L}\frac{|F_i^{\mathrm{c}}|}{m} \\ &\approx |\sigma v_{\min} T - 2\pi\sigma| + \frac{\tau^2}{2}\frac{2\pi}{L}\frac{e^2}{4\pi\epsilon_0 m}\frac{N^2}{L^2}(v_{\max} - v_{\min})\frac{\pi^2}{6} \end{aligned} \tag{4.83}$$

For $\tau = 0.05T$ we get $|\Delta\theta_i| < 2\pi \cdot 0.25\gamma$, thus the accuracy $\gamma < \sqrt{\epsilon}/(2\pi \cdot 0.25) \approx 5 \cdot 10^{-6}$ is required for the external forces.

4.5.2 Measurement of Hawking Phonons

The measurement scheme described in the previous section requires the accurate control of the ion acceleration during the creation of the black hole (see Eq. (4.83)). Here we propose a scheme to avoid this difficulty (see also [Sch06]). If the number of ions in the supersonic region $(1-2\sigma)N$ is small, the displacement of the ions due to the creation of the black hole will be small compared to the equilibrium motion of the ions. Then the creation of the black hole is adiabatic. In this case the measurement of cross-correlations is not possible. Instead, we describe in this subsection how to directly measure the emitted Hawking phonons outside of the black hole.

The following setup is studied: After the black hole formation in the small time interval τ, Hawking phonons are emitted at the black hole

horizon. We propose to detect these phonons by coupling the oscillation of the ions to their internal state with a laser. The laser drives a transition between two internal states $\left|a\right\rangle$ and $\left|b\right\rangle$ of the ions, which are prepared in the state $\left|a\right\rangle$. It illuminates $\widetilde{N}$ ions outside of the black hole and is following the motion of these ions for the time interval t_m. Since t_m determines the spectral width of the laser, it must be large compared to the inverse Hawking temperature $t_m \gg \hbar/(k_\mathrm{B}T_\mathrm{H})$. The laser frequency ω should fullfill the resonance condition

$$\omega = \omega_I + \omega_{p_0} + kv\frac{L}{2\pi}, \tag{4.84}$$

which takes into account the transition frequency of the ions ω_I, the Doppler shift kv, and the relevant phonon frequency ω_{p_0}. After going to the frame rotating with ω_I and ω_{p_0} and applying the rotating wave approximation the dipolar coupling Hamiltonian [WMI+98] in the Lamb-Dicke limit (see Eq. (4.78)) becomes

$$\mathcal{H}_{dip} = \sum_{j,p}\left(\frac{\hbar\Omega_p}{2}\sigma_j^+ a_p e^{i(p+k)Lj/N} + H.c.\right) + \sum_p \hbar\left(\omega_p - \omega_{p_0}\right) a_p^\dagger a_p, \tag{4.85}$$

where the sums extend over the illuminated ions j and the relevant phonon modes p. k denotes the wavenumber of the laser and

$$\Omega_p = -i\Omega k\sqrt{\frac{2\hbar}{m\omega_p}} \tag{4.86}$$

are the effective Rabi frequencies with the bare Rabi frequency Ω. We describe here the coupling of the phonon modes to a sideband transition. In the limit of a laser pulse with small spectral width $\widetilde{N} \ll Nt_m/T$ we can introduce the spin $\Sigma = \widetilde{N}/2$ operator $\Sigma^+ = \sum_j \exp\left(-ikLj/N\right)\sigma_j^+/2$ and transform it into a bosonic field $b^\dagger$ with the Holstein-Primakoff transformation

$$\Sigma^+ = b^\dagger\sqrt{2\Sigma - b^\dagger b} \approx b^\dagger\sqrt{\widetilde{N}} \tag{4.87}$$

For $\langle b^\dagger b\rangle \approx \langle a_p^\dagger a_p\rangle \lesssim k_\mathrm{B}T_\mathrm{H}/(\hbar\omega_\mathrm{rot}) \ll \widetilde{N}$ (see Eq. (4.89)), we can use $\Sigma^+ \sim \sqrt{\widetilde{N}}b^\dagger$. The expectation value $\langle b^\dagger b\rangle$ gives the number of ions in the state $\left|b\right\rangle$. So the coupling of the relevant phonon modes to the illuminated ions can be described by the Hamiltonian

$$\mathcal{H}_{dip} = \hbar\sqrt{\widetilde{N}}\sum_p\left(\Omega_p b^\dagger a_p + H.c.\right) + \sum_p \hbar(\omega_p - \omega_{p_0})a_p^\dagger a_p. \tag{4.88}$$

The number of excited ions after their illumination is

$$\langle b^\dagger b\rangle_{t_M} = \sum_p \frac{|\Omega_p|^2}{\sum_q |\Omega_q|^2} \sin^2\left(\sqrt{\sum_q |\Omega_q|^2}\, t_m\right) \langle a_p^\dagger a_p\rangle_0 \tag{4.89}$$

with the assumption of large Rabi frequencies $\sqrt{\widetilde{N}}\Omega_{p_0} \gg \omega_{p_0}$. Thus, the number of ions is proportional to the number of phonons around the mode ω_{p_0}. The standard deviation of the phonon number measurement is approximately

$$\sigma_m \approx \sqrt{\frac{\langle (\Delta b^\dagger b)^2\rangle_{t_m}}{M}} \approx \frac{\langle \Delta b^\dagger b\rangle_{t_m}}{\sqrt{M}} \lesssim \frac{k_\mathrm{B} T_\mathrm{H}}{\hbar\omega_\mathrm{rot}\sqrt{M}}. \tag{4.90}$$

Now, we are presenting an example that satisfies the requirements of this measurement proposal. We consider $N = 10^5$ singly charged ^9Be ions with ion spacing $L/N = 2\mu m$ and average rotation frequency $\omega_\mathrm{rot} = 2\pi \times 1.2kHz$ ($e^2/4\pi\epsilon_0 \approx 0.7/(2N)\, mL^3/T^2$). The black hole region contains $(1-2\sigma)N = 0.007N$ and the horizon region $2\gamma_1 N = 0.004N$ ions. The angular velocity in the subsonic region is $v_\mathrm{min} = 2\pi \times 0.99/T$ and in the supersonic region $v_\mathrm{max} = 2\pi \times 2.4/T$. The Hawking temperature in this system is $k_\mathrm{B}T_\mathrm{H}/\hbar \approx 106/T \approx 2\pi \times 20kHz$. In the small time interval $\tau = 0.05T$ of the black hole creation, the ions are normally traversing the angle $\Delta\theta \approx 2\pi \times 0.05$, which is large compared to the size of the black hole region. For the measurement we propose to illuminate $\widetilde{N} = 200$ ions for the time $t_M = T/4$. In this case $M = 100$ repetitions of the experiment are sufficient.

4.6 Conclusion

In summary, we have discussed in this chapter the details of a recent proposal to observe the Hawking effect with ions rotating on a ring [HRF$^+$10]. We have described how to create an analog black hole spacetime in this system (see Sec. 4.2). The horizon emits Hawking radiation with a thermal spectrum (see Sec. 4.4.1). We have analyzed the emergence of correlations and entanglement between the inside and the outside of a black hole after its creation (see Sec. 4.4.2). These correlations are a signature for the pair creation mechanism of Hawking radiation.

With this work we have deepened our analysis of the emerging entanglement (see Sec. 4.4.2). We cannot observe the creation of entanglement at too high initial temperatures. The generated cross-correlations, instead, remain present at arbitrarily high initial temperatures. Thus, we find the transition from the *quantum* to the *classical* Hawking effect (spontaneous versus stimulated emission).

Nevertheless, current technology allows to measure the *quantum* Hawking effect in an experiment. We have presented a detailed discussion of realistic measurement techniques. It is possible to directly measure the cross-correlation signal (see Sec. 4.5.1) or the emitted Hawking phonons (see Sec. 4.5.2).

To conclude, we expect ring traps to be extremely useful for future quantum simulations. They offer great opportunities, especially for studying translationally invariant systems.

Chapter 5

Conclusion and Outlook

In this thesis we have presented three proposals for quantum simulations of dynamical systems with neutral atoms in optical lattices and ions in electrodynamic traps. These setups with great potential for future quantum simulations and quantum computation have complementary strengths and weaknesses: On the one hand, it is relatively simple to prepare optical lattices with more than a thousand atoms [BDZ08, LSA+07], but it is challenging to control more than ten ions in the quantum regime. On the other hand, single ions can be manipulated very efficiently in experiments [WMI+98], but it is challenging to address single sites in optical lattices. Recent developments like surface traps for ions [CBB+05] and single atom microscopy in optical lattices could reduce these differences [SWE+10, BGP+09].

In chapter 2 we discussed possibilities for measuring Anderson localization in optical lattices by creating an additional disordered potential [SPL10]. Recently, this task was achieved [BJZ+08, RDF+08, DZR+10]. We have proposed alternative schemes in this thesis, in which a frozen species of particles generates the disorder potential for a mobile species [GC05, PVC05]. These proposals allow the control over the correlations within the disorder potential [HCR07] and possibly the observation of disorder-induced phases in the strongly-interacting regime [HDR10]. However, the recently developed atom microscopes could be used to generate disorder potentials with an even greater control and flexibility [SWE+10, BGP+09].

We further studied the quantum simulation of dissipative systems in chapter 3. Here we observe that phase transitions in the system are reflected in the decoherent dynamics [HC11]. We believe that engineering

decoherent evolutions will enrich the field of quantum simulations and quantum computations by magnifying system properties or stabilizing interesting quantum states [VWC09, KBD+08].

In chapter 4 we contribute to the field of analog gravity and have proposed the measurement of Hawking radiation from acoustic black holes on rotating ions trapped on a ring geometry. Several proposals for the measurement of Hawking radiation already exist [BN09]. However, the Hawking effect has not been clearly measured in the quantum regime, yet. We have shown that the unprecedented experimental control over trapped ions allows to realize Hawking radiation [HRF+10] and to study the emergence of entanglement between the inside and the outside of the black hole [HSR+11]. Thus, clear signatures for the quantum Hawking effect could be found with ion rings.

Appendix A

Ion Ring System

A.1 External Forces

In this Appendix we present the detailed form of the external forces appearing in the general Hamiltonian (4.1) and the harmonic Hamiltonian Eq. (4.5). These forces are chosen to enforce the imposed equilibrium motion of the ions $\theta_i^0(t)$ in Eq. (4.2).

The Coulomb force on the ith ion tangential to the ring is given by

$$F_i^{\mathrm{c}}\left(\theta_1(t),\ldots,\theta_N(t)\right) = \frac{e^2}{4\pi\epsilon_0}\sum_{j\neq i} F^{\mathrm{c}}\left(\theta_i(t)-\theta_j(t)\right) \tag{A.1}$$

with

$$F^{\mathrm{c}}(\Delta\theta) = \pi^2 \mathrm{sign}(\sin(\Delta\theta/2))\frac{\cos(\Delta\theta/2)}{L^2\sin(\Delta\theta/2)^2}, \tag{A.2}$$

where $\theta_i(t)$ gives the ion position at time t. The classical equations of motion are now $mL/(2\pi)\ddot{\theta}_i(t) = F_i^{\mathrm{c}}(t) + F^{\mathrm{e}}(\theta_i(t))$. We determine the local external force F^{e} from this equation such that it guarantees the imposed

equilibrium trajectories of the ions

$$\begin{aligned} F^{\mathrm{e}}(\theta,t) &= \left[\frac{L}{2\pi T^2}\right] g''_{v_{\min}}\left(g^{-1}(\theta)\right) \\ &+ \left[\frac{L}{2\pi T}\right] 2\frac{\partial g'_{v_{\min}}}{\partial v}\left(g^{-1}(\theta)\right)\cdot\frac{dv}{dt}(t) \\ &+ \left[\frac{L}{2\pi}\right]\frac{\partial^2 g_{v_{\min}}}{\partial v^2}\left(g^{-1}(\theta)\right)\cdot\left[\frac{dv}{dt}(t)\right]^2 \\ &+ \frac{\partial g_{v_{\min}}}{\partial v}\left(g^{-1}(\theta)\right)\cdot\frac{d^2v}{dt^2}(t) \\ &+ \sum_{i=1}^{N-1} F^{\mathrm{c}}\left(\theta - g_{v_{\min}}(g^{-1}(\theta)+\frac{i}{N})\right). \end{aligned} \tag{A.3}$$

This force is time-independent if the parameter $v_{\min}$ is time-independent.

In harmonic approximation (see Eq. (4.5)) the Coulomb force and the external force are encoded in the force matrix $\mathcal{F} = (f_{ij})$

$$\left(\frac{L}{2\pi}\right)^2 f_{ij}(t) = f^{\mathrm{c}}_{ij}(t) + \delta_{ij} f^{\mathrm{e}}_i(t). \tag{A.4}$$

The contribution from the Coulomb force is

$$f^{\mathrm{c}}_{ij}(t) = \frac{e^2}{4\pi\epsilon_0}\cdot\begin{cases} f^{\mathrm{c}}\left(\theta^0_i(t)-\theta^0_j(t)\right) & i\neq j \\ -\sum_{k\neq i} f^{\mathrm{c}}\left(\theta^0_i(t)-\theta^0_k(t)\right) & i=j \end{cases} \tag{A.5}$$

with

$$f^{\mathrm{c}}(\Delta\theta) = \pi^3\left|\frac{1+\cos(\Delta\theta/2)^2}{\sin(\Delta\theta/2)^3}\right|. \tag{A.6}$$

The contribution from the diagonal external force is

$$\begin{aligned} f^{\mathrm{e}}_i(t) &= \frac{m}{g'\left(\frac{i}{N}+\frac{t}{T}\right)}\left\{\left[\frac{L}{2\pi T^2}\right] g'''_{v_{\min}}\left(\frac{i}{N}+\frac{t}{T}\right)\right. \\ &+2\left[\frac{L}{2\pi T}\right]\frac{\partial g''_{v_{\min}}}{\partial v_{\min}}\left(\frac{i}{N}+\frac{t}{T}\right)\cdot\frac{dv}{dt}(t) \\ &+\left[\frac{L}{2\pi}\right]\frac{\partial^2 g'_{v_{\min}}}{\partial {v_{\min}}^2}\left(\frac{i}{N}+\frac{t}{T}\right)\cdot\left[\frac{dv}{dt}(t)\right]^2 \\ &\left.+\frac{\partial g'_{v_{\min}}}{\partial v_{\min}}\left(\frac{i}{N}+\frac{t}{T}\right)\cdot\frac{d^2v}{dt^2}(t)\right\} \\ &+\frac{e^2}{4\pi\epsilon_0}\cdot\sum_{j\neq i} f^{\mathrm{c}}\left(\theta^0_i(t)-\theta^0_j(t)\right)\left[1-\frac{f'\left(\frac{j}{N}+t\right)}{f'\left(\frac{i}{N}+t\right)}\right]. \end{aligned} \tag{A.7}$$

A.2 Velocity Profile

The classical equilibrium positions of the ions, thus their velocity profile, are imposed by the function g as specified in Eq. (4.2). We make the choice

$$\frac{g'(x)}{T} = \begin{cases} v_{\min} & 0 \leq x \leq \sigma - \gamma_1 \\ \beta + \alpha h\left(\frac{x-\sigma}{\gamma_1}\right) & -\gamma_1 < x - \sigma < \gamma_1 \\ v_{\max} & \sigma + \gamma_1 \leq x \leq 1 - \sigma - \gamma_2 \\ \beta - \alpha h\left(\frac{x-1+\sigma}{\gamma_2}\right) & -\gamma_2 < x - (1-\sigma) < \gamma_2 \\ v_{\min} & 1 - \sigma + \gamma_2 \leq x \leq 1 \end{cases} \tag{A.8}$$

with $\alpha = (v_{\max} - v_{\min})/2$ and $\beta = (v_{\max} + v_{\min})/2$ and $h(s) = 15/8s - 5/4s^3 + 3/8s^5$. We use $g(0) = 0$ to determine the equilibrium positions of the ions. In the supersonic region $\sigma v_{\min} T \lesssim \theta \lesssim 2\pi - \sigma v_{\min} T$ the constant angular ion velocity is $v_{\max}$ (see Eq. (4.4)) and in the complementary subsonic region its constant value is $v(\theta) = v_{\min}$. Thus, the black hole horizon is located close to $\theta_{\mathrm{H}} = \sigma v_{\min} T$. This stepwise definition has the advantage that the velocity profile is flat inside and outside of the horizon, that the width of both regions can be adjusted, and that the width of the horizon regions can be adjusted. This flexibility is useful for the detection of correlation patterns in Sec. 4.4.2. Also this profile must be sufficently continuous to generate a physically allowed equilibrium motion.

In a part of this paper we dynamically create a black hole metric from a flat metric. We choose to reduce the velocity in the subsonic region from $2\pi/T$ at $t = 0$, corresponding to homogeneously spaced ions, down to $v_{\min}$ at $t \gg \tau$ according to

$$v_{\min}(t) = v_{\min} + \left(\frac{2\pi}{T} - v_{\min}\right) \exp\left[-\left(\frac{t}{\tau}\right)^2\right]. \tag{A.9}$$

We choose a Gaussian profile to guarantee $\frac{\partial v}{\partial t}(t = 0) = 0$. In this case, the velocity profile becomes (compare with Eq. (4.3))

$$v(\theta, t) = \frac{g'_{v_{\min}}\left(g^{-1}(\theta)\right)}{T} + \frac{\partial g_{v_{\min}}}{\partial v_{\min}}\left(g^{-1}(\theta)\right) \cdot \frac{dv_{\min}}{dt}(t). \tag{A.10}$$

A.3 Equations of Motion and Equilibrium State

The quasi-free quantum dynamics of the harmonic system (4.5) are governed by the classical linear equations of motion for the first (see Eq. (4.7)) and second moments (see Eq (4.8)). The equations for the first moments can be written

$$\frac{\partial}{\partial t}\langle\hat{\xi}_i\rangle_t = \sum_j G_{ij}(t)\langle\hat{\xi}_j\rangle_t \tag{A.11}$$

with the matrix $\mathcal{G} = (G_{ij})$

$$\mathcal{G} = \begin{pmatrix} 0 & \left(\frac{2\pi}{L}\right)^2 \cdot \frac{1}{m} \\ \left(\frac{L}{2\pi}\right)^2 \mathcal{F} & 0 \end{pmatrix}. \tag{A.12}$$

The dynamics for the second moments are governed by the equation

$$\frac{\partial}{\partial t}\Gamma(t) = \mathcal{G}(t)\cdot\Gamma(t) + \Gamma(t)\cdot\mathcal{G}(t)^T. \tag{A.13}$$

We determine the thermal state with temperature T_0 of homogeneously spaced ions at rest by a mode decomposition of the system. The Fourier transform O diagonalizes the system (4.5)

$$\delta\widetilde{\theta}_k = \sum_{i=1}^{N} O_{ki}\delta\hat{\theta}_i, \;\; \delta\widetilde{p}_k = \sum_{i=1}^{N} O_{ki}^T\delta\hat{p}_i \tag{A.14}$$

to

$$\mathcal{H} = \sum_{k=1}^{N}\left[\frac{\delta\widetilde{p}_i^2}{2m} + \frac{m}{2}\omega_k^2\delta\widetilde{\theta}_k^2\left(\frac{L}{2\pi}\right)^2\right] \tag{A.15}$$

The mode frequencies are

$$\omega_k^2\delta_{kl} = \left(\frac{2\pi}{L}\right)^2 \left(OfO^T\right)_{kl}. \tag{A.16}$$

According to the Bose-Einstein statistic each mode is on average occupied by

$$\langle\hat{n}_k\rangle = \frac{1}{\exp\left(\frac{\hbar\omega}{k_B T_0}\right) - 1} \tag{A.17}$$

phonons. In equilibrium the first moments vanish $\langle\hat{\xi}_i\rangle = 0$ due to the parity symmetry of the harmonic Hamiltonian (4.5). The covariance matrix at temperature T_0 is given by

$$\begin{aligned}
\langle\delta\hat{\theta}_i\delta\hat{\theta}_j\rangle &= \left(\frac{2\pi}{L}\right)^2 \frac{\hbar}{m}\sum_{k=1}^{N} O_{ik}^T \frac{\langle\hat{n}_k\rangle + \frac{1}{2}}{\omega_k} O_{kj}, \\
\langle\delta\hat{p}_i\delta\hat{p}_j\rangle &= \hbar m \sum_{k=1}^{N} O_{ik}\omega_k \left(\langle\hat{n}_k\rangle + \frac{1}{2}\right) O_{kj}^T, \\
\langle\delta\hat{\theta}_i\delta\hat{p}_j\rangle &= 0.
\end{aligned} \tag{A.18}$$

Appendix B

Ion Ring Stability Analysis

In this Appendix we describe a stability analysis of our system. After a brief introduction to the method, we show results of the numerical simulations and put them into the context of previous works [GAC+00]. Finally, we show that the observed instabilities are not important for our proposal.

The solution of explicit linear differential equations like Eq. (A.11) can be written

$$\langle\hat{\xi}_i\rangle_t = \sum_j U_{ij}(t)\langle\hat{\xi}_j\rangle_t \tag{B.1}$$

with the monodromy matrix $\mathbf{U}(t)$ satisfying the initial condition $\mathbf{U}(0) = \mathbf{1}$ and the dynamics

$$\partial_t \mathbf{U}(t) = \mathbf{G}(t) \cdot \mathbf{U}(t). \tag{B.2}$$

If the system is periodic $\mathbf{G}(t+T) = \mathbf{G}(t)$, Floquet theorem states

$$\mathbf{U}(t) = \mathbf{X}(t) \cdot e^{\mathbf{R}t} \tag{B.3}$$

with the periodic matrix $\mathbf{X}(t+T) = \mathbf{X}(t)$ and the constant matrix $\mathbf{R}$ (see e.g., [Flo83]). Therefore, the stability of the motion is determined by the eigenvalue of the matrix $\mathbf{U}(T) = \exp(\mathbf{R}T)$ with the largest magnitude. We denote this magnitude by μ, the dynamics are unstable for $\mu > 1$. The monodromy matrix $\mathbf{U}$ does not only describe the first moments (see Eq. (B.1)), but also the evolution of the covariance matrix (see Eq. (A.13))

$$\Gamma(t) = \mathbf{U}(t)\Gamma(0)\mathbf{U}^T(t) = (\mathbf{U}(t) \otimes \mathbf{U}(t))\,\Gamma(0). \tag{B.4}$$

In our case the periodicity with period T is not the highest symmetry. The system is also invariant under combined translations in time and space (see

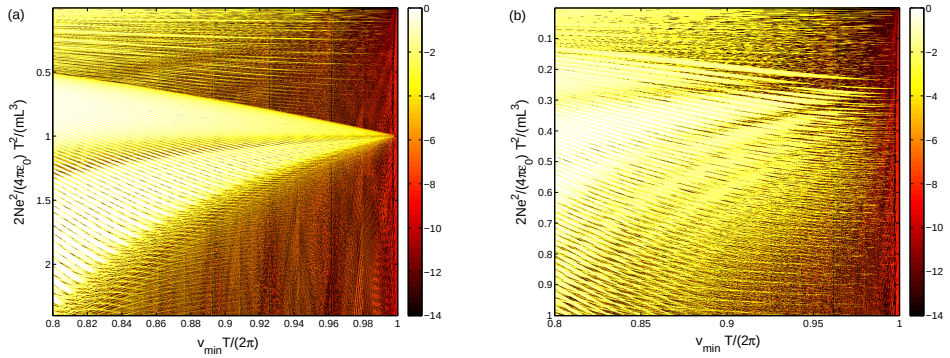

Figure B.1: $\log(\mu - 1)$ for $N = 100$ ions, and $\sigma v_{\min} T = 2\pi \cdot 0.25$. In this stability diagram values of $\log(\mu - 1)$ close to zero represent stable systems. (a) Only nearest-neighbor interactions considered; (b) Full Coulomb interactions considered.

Eq. 4.46). Thus $\mathbf{U}(T)$ follows from $\mathbf{U}(T/N)$

$$\mathbf{U}(T) = (\mathcal{T} \cdot \mathbf{U}(T/N))^N , \tag{B.5}$$

where $\mathcal{T}$ is the index translation matrix.

The results of the numerical stability analysis are shown in Fig. B.1(a) for nearest-neighbor interactions and in Fig. B.1(b) for full Coulomb interactions as a function of $\overline{(cT/(2\pi))^2} = 2Ne^2/(4\pi\epsilon_0) \cdot T^2/(mL^3)$ and $v_{\min} T/(2\pi)$. For $\sigma v_{\min} T = 2\pi \times 0.25$, $\overline{c^2}$ is the mean of the squares of the two sound velocities (see Eq. (4.16)) on the ion ring. The analysis shows a distinction between three parameter regions. If the system is supersonic on the whole ring (at small $\overline{c^2}$) the system is mostly stable with stripes of instabilities. If the system is subsonic on the whole ring (at large $\overline{c^2}$) the system is always stable. In the interesting intermediate regime a subsonic region coexists with a supersonic region on the ion ring, here the stability analysis is most complex. In this case the system is unstable apart from stripes of stability that bunch up in the central region which is most interesting for experiments. So we find that the appearance of instabilities is closely related to the presence of a black hole horizon. The structure of the instabilities is very similar to the result of the stability analysis in [GAC+00]. Black hole laser instabilities [Cor99] may contribute to these behavior. They occur in the presence of two horizon when particles bounce between the horizons and enhance themselves.

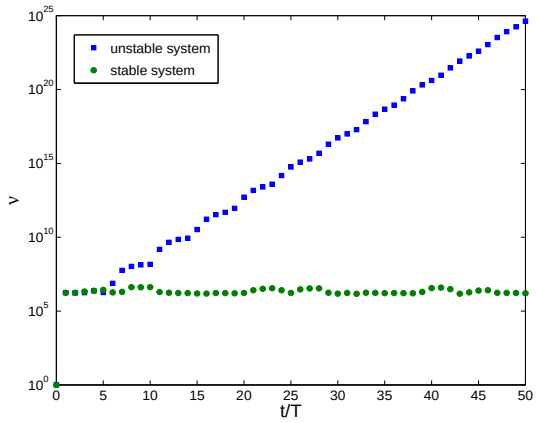

Figure B.2: Largest eigenvalue of $\mathbf{U}^\dagger(t)\mathbf{U}(t)$ at time steps t=nT. This quantity is an upper bound of observables. We consider $N = 1000$ ions, $\sigma v_{\min} T = 2\pi \cdot 0.25$, and $\tau = 0.05T$. We compare the stable system $e^2/4\pi\epsilon_0 = \frac{0.2453}{2N}\frac{mL^3}{T^2}$ (green dots) with the unstable system $e^2/4\pi\epsilon_0 = \frac{0.2446}{2N}\frac{mL^3}{T^2}$ (blue squares). Full Coulomb interactions are considered.

This stability analysis detects exponential instabilities. We show now that these exponential instabilities are not important for the proposed experiment. The increase of the experimental quantities is bounded by the maximal magnitude ν of the eigenvalues of $(\mathbf{U}^\dagger(T))^n(\mathbf{U}(T))^n$ for $n = 1, 2, \ldots$. ν is shown in Fig. B.2 for an exponentially stable and an exponentially unstable system. The exponential instability becomes dominant for $t > 5T$. Therefore, it does not have a consequence for the proposed experiment performed during $t \lesssim T$.

Bibliography

[AAL+79] E. Abrahams, P.W. Anderson, D.C. Licciardello, and T.V. Ramakrishnan, *Scaling theory of localization: Absence of quantum diffusion in two dimensions*, Phys. Rev. Lett. **42**, 673 (1979).

[And58] P.W. Anderson, *Absence of diffusion in certain random lattices*, Phys. Rev. Lett. **109**, 1492 (1958).

[BBP+96] C.H. Bennett, H.J. Bernstein, S. Popescu, and B. Schumacher, *Concentrating partial entanglement by local operations*, Phys. Rev A **53**, 2046 (1996).

[BCC+10] F. Belgiorno, S.L. Cacciatori, M. Clerici, V. Gorini, G. Ortenzi, L. Rizzi, E. Rubino, V.G. Sala, and D. Faccio, *Hawking Radiation from Ultrashort Laser Pulse Filaments*, Phys. Rev. Lett. **105**, 203901 (2010).

[BCJ+99] G.K. Brennen, C.M. Caves, P.S. Jessen, and I.H. Deutsch, *Quantum Logic Gates in Optical Lattices*, Phys. Rev. Lett. **82**, 1060 (1999).

[BD82] N.D. Birrel and P.C.W. Davies, *Quantum fields in curved spaces*, Cambridge University Press (1982).

[BDZ08] I. Bloch, J. Dalibard, and W. Zwerger, *Many-body physics with ultracold atoms*, Rev. Mod. Phys. **80**, 885 (2008).

[BFF+05a] R. Balbinot, S. Fagnocchi, A. Fabbri, and G.P. Procopio, *Backreaction in Acoustic Black Holes*, Phys. Rev. Lett. **94**, 161302 (2005).

[BFF+05b] R. Balbinot, A. Fabbri, S. Fagnocchi, and R. Parentani, *Hawking radiation from acoustic black holes, short distance and backreaction effects*, Riv. Nuovo Cim. **28**, 3 (2005).

[BFF05] R. Balbinot, S. Fagnocchi, and A. Fabbri, *Quantum effects in acoustic black holes: The backreaction*, Phys. Rev. D **71**, 064019 (2005).

[BFF+08] R. Balbinot, A. Fabbri, S. Fagnocchi, A. Recati, and I. Carusotto, *Nonlocal density correlations as a signature of Hawking radiation from acoustic black holes*, Phys. Rev. A **78**, 021603(R) (2008).

[BGP+09] W.S. Bakr, J.I. Gillen, A. Peng, S. Fölling, and M. Greiner, *A quantum gas microscope for detecting single atoms in a Hubbard-regime optical lattice*, Nature **462**, 74 (2009).

[BJZ+08] J. Billy, V. Josse, Z. Zuo, A. Bernard, B. Hambrecht, P. Lugan, D. Clément, L. Sanchez-Palencia, P. Bouyer, and A. Aspect, *Direct observation of Anderson localization of matter waves in a controlled disorder*, Nature **453**, 891 (2008).

[BKW92] G. Birkl, S. Kassner, and H. Walther, *Multiple-shell structures of laser-cooled $^{24}Mg^+$ ions in a quadrupole storage ring*, Nature **357**, 310 (1992).

[BLV05] C. Barceló, S. Liberati, and M. Visser, *Analogue Gravity*, Living Rev. Rel. **8**, 12 (2005).

[BMP+95] R. Brout, S. Massar, R. Parentani, and P. Spindel, *Hawking radiation without trans-Planckian frequencies*, Phys. Rev. D **52**, 4559 (1995).

[BN09] I. Buluta and F. Nori, *Quantum Simulators*, Science **326**, 108 (2009).

[BP02] H.-P. Breuer, and F. Petruccione, *The Theory of Open Quantum Systems*, Oxford University Press (2002).

[BR03] A. Botero and B. Reznik, *Modewise entanglement of Gaussian states*, Phys. Rev. A **67**, 052311 (2003).

[BSS+08] S. Braungardt, A. Sen, U. Sen, R.J. Glauber, and M. Lewenstein, *Fermion and spin counting in strongly correlated systems*, Phys. Rev. A **78**, 063613 (2008).

[CBB+05] J. Chiaverini, R.B. Blakestad, J. Britton, J.D. Jost, C. Langer, D. Leibfried, R. Ozeri, and D.J. Wineland, *Surface-Electrode Architecture for Ion-Trap Quantum Information Processing*, Quant. Inf. Comput. **5**, 419 (2005).

[CFR+08] I. Carusotto, S. Fagnocchi, A. Recati, R. Balbinot, and A. Fabbri, *Numerical observation of Hawking radiation from acoustic black holes in atomic Bose-Einstein condensates*, New J. Phys. **10**, 103001 (2008).

[CGJ+10] C. Chin, R. Grimm, P. Julienne, and E. Tiesinga, *Feshbach resonances in ultracold gases*, Rev. Mod. Phys. **82**, 1225 (2010).

[Chu69] D.A. Church, *Storage-Ring Ion Trap Derived from the Linear Quadrupole Radio-Frequency Mass Filter*, J. Appl. Phys. **40**, 3127 (1969).

[CJ98] S. Corley and T. Jacobson, *Lattice black holes*, Phys. Rev. D. **57**, 6269 (1998).

[Cor98] S. Corley, *Computing the spectrum of black hole radiation in the presence of high frequency dispersion: An analytical approach*, Phys. Rev. D **57**, 6280 (1998).

[Cor99] S. Corley and T. Jacobson, *Black hole lasers*, Phys. Rev. D **59**, 124011 (1999).

[CPH+10] S.R. Clark, J. Prior, M.J. Hartmann, D. Jaksch, and M.B. Plenio, *Exact matrix product solutions in the Heisenberg picture of an open quantum spin chain*, New J. Phys. **12**, 025005 (2010).

[CVH+05] D. Clément, A.F. Varón, M. Hugbart, J.A. Retter, P. Bouyer, L. Sanchez-Palencia, D.M. Gangardt, G.V. Shlyapnikov, and A. Aspect, *Suppression of Transport of an Interacting Elongated Bose-Einstein Condensate in a Random Potential*, Phys. Rev. Lett. **95**, 170409 (2005).

[CVR+06] D. Clément, A.F. Varón, J.A. Retter, L. Sanchez-Palencia, A. Aspect, and P. Bouyer, *Experimental study of the transport of coherent interacting matter-waves in a 1D random potential induced by laser speckle*, New J. of Phys. **8**, 165 (2006).

[CZ95] J.I. Cirac and P. Zoller, *Quantum Computations with Cold Trapped Ions*, Phys. Rev. Lett. **74**, 4091 (1995).

[Deu85] D. Deutsch, *Quantum Theory, the Church-Turing Principle and the Universal Quantum Computer*, Proc. R. Soc. Lond. A **400**, 97 (1985).

[DGS+09] S. Dürr, J.J. García-Ripoll, N. Syassen, D.M. Bauer, M. Lettner, J.I. Cirac, and G. Rempe, *Lieb-Liniger model of a dissipation-induced Tonks-Girardeau gas*, Phys. Rev. A **79**, 023614 (2009).

[DJA+88] B.I. Deutch, F.M. Jacobsen, L.H. Andersen, P. Hvelplund, H. Knudsen, M.H. Holzscheiter, M. Charlton, and G. Laricchia, *Antihydrogen Production by Positronium-Antiproton Collisions in an Ion Trap*, Phys. Script. **T22**, 248 (1988).

[DMK+08] S. Diehl, A. Micheli, A. Kantian, B. Kraus, H.P. Büchler, and P. Zoller, *Quantum states and phases in driven open quantum systems with cold atoms*, Nature Physics **4**, 878 (2008).

[DP64] J. Drees and W.Z. Paul, *Beschleunigung von Elektronen in einem Plasmabetatron*, Z. Phys. **180**, 340 (1964).

[DTD+09] A.J. Daley, J.M. Taylor, S. Diehl, M. Baranov, and P. Zoller, *Atomic Three-Body Loss as a Dynamical Three-Body Interaction*, Phys. Rev. Lett. **102**, 040402 (2009).

[DTM+10] S. Diehl, A. Tomadin, A. Micheli, R. Fazio, and P. Zoller, *Dynamical Phase Transitions and Instabilities in Open Atomic Many-Body Systems*, Phys. Rev. Lett. **105**, 015702 (2010).

[DWP90] D.H. Dunlap, H.-L. Wu, P.W. Phillips, *Absence of localization in a random-dimer model*, Phys. Rev. Lett. **65**, 88 (1990).

[DYD+10] S. Diehl, W. Yi, A.J. Daley, and P. Zoller, *Dissipation-Induced d-Wave Pairing of Fermionic Atoms in an Optical Lattice*, Phys. Rev. Lett. **105**, 227001 (2010).

[DZR+10] B. Deissler, M. Zaccanti, G. Roati, C. D'Errico, M. Fattori, M. Modugno, G. Modugno, and M. Inguscio, *Delocalization of a disordered bosonic system by repulsive interactions*, Nature Physics **6**, 354 (2010).

[DZS+03] B. Damski, J. Zakrzewski, L. Santos, P. Zoller, and M. Lewenstein, *Atomic Bose and Anderson Glasses in Optical Lattices*, Phys. Rev. Lett. **91**, 080403 (2003).

[EMK+03] J. Eschner, G. Morigi, F. Kaler, and R. Blatt, *Laser cooling of trapped ions*, J. Opt. Soc. Am. B **20**, 5 (2003).

[FCB+10] A. Fabbri, I. Carusotto, R. Balbinot, and A. Recati, *Density correlations and analog dynamical Casimir emission of Bogoliubov phonons in modulated atomic Bose-Einstein condensates*, Eur. Phys. J. D **56**, 391 (2010).

[Fey82] R.P. Feynman, *Simulating physics with computers*, Int. J. Theor. Phys. **21**, 467 (1982).

[FF03] P.O. Fedichev and U.R. Fischer, *Gibbons-Hawking Effect in the Sonic de Sitter Space-Time of an Expanding Bose-Einstein-Condensed Gas*, Phys. Rev. Lett. **91**, 240407 (2003).

[FFG+05] C. Fort, L. Fallani, V. Guarrera, J.E. Lye, M. Modugno, D.S. Wiersma, and M. Inguscio, *Effect of Optical Disorder and Single Defects on the Expansion of a Bose-Einstein Condensate in a One-Dimensional Waveguide*, Phys. Rev. Lett. **95**, 170410 (2005).

[FFI08] L. Fallani, C. Fort, and M. Inguscio, *Bose-Einstein condensates in disordered potentials*, Adv. At. Mol. Opt. Phys. **56**, 119 (2008).

[FLG+06] L. Fallani, J. E. Lye, V. Guarrera, C. Fort, and M. Inguscio, *Ultracold Atoms in a Disordered Crystal of Light: Towards a Bose Glass*, Phys. Rev. Lett. **98**, 130404 (2007).

[Flo83] G. Floquet, *Sur les équations différentielles linéaires à coefficients périodiques*, Ann. École Norm. Sup. 12, **47** (1883).

[FSG+08] A. Friedenauer, H. Schmitz, J. Glückert, D. Porras, and T. Schätz, *Simulating a quantum magnet with trapped ions*, Nature Physics **4**, 757 (2008).

[FT10] R. Fazio and A. Tomadin, *Quantum Simulators and Quantum Design*, Il Nuovo Saggiatore **26**, 5 (2010).

[FWG+89] M.P.A. Fisher, P.B. Weichman, G. Grinstein, and D.S. Fisher, *Boson localization and the superfluid-insulator transition*, Phys. Rev. B **40**, 546 (1989).

[GAC+00] L.J. Garay, J.R. Anglin, J.I. Cirac, and P. Zoller, *Sonic Analog of Gravitational Black Holes in Bose-Einstein Condensates*, Phys. Rev. Lett. **85**, 4643 (2000).

[GAC+01] L.J. Garay, J.R. Anglin, J.I. Cirac, and P. Zoller, *Sonic black holes in dilute Bose-Einstein condensates*, Phys. Rev. A **63**, 023611 (2001).

[GC05] U. Gavish and Y. Castin, *Matter-Wave Localization in Disordered Cold Atom Lattices*, Phys. Rev. Lett. **95**, 020401 (2005).

[GDS+09] J.J. García-Ripoll, S. Dürr, N. Syassen, D.M. Bauer, M. Lettner, G. Rempe, and J.I. Cirac, *Dissipation-induced hard-core boson gas in an optical lattice*, New J. Phys. **11**, 013053 (2009).

[Gio05] S. Giovanazzi, *Hawking Radiation in Sonic Black Holes*, Phys. Rev. Lett. **94**, 061302 (2005).

[GME02] M. Greiner, O. Mandel, T. Esslinger, T.W. Hänsch, and I. Bloch, *Quantum phase transition from a superfluid to a Mott insulator in a gas of ultracold atoms*, Nature **415**, 39 (2002).

[Gro95] L.K. Grover, *A fast quantum mechanical algorithm for database search*, Proceedings, 28th Annual ACM Symposium on the Theory of Computing (STOC), 212 (1996).

[GWS+05] H. Gimperlein, S. Wessel, J. Schmiedmayer, and L. Santos, *Ultracold Atoms in Optical Lattices with Random On-Site Interactions*, Phys. Rev. Lett. **95**, 170401 (2005).

[Haw74] S.W. Hawking, *Black hole explosions?*, Nature **248**, 30 (1974).

[HC11] B. Horstmann and J.I. Cirac, *Decoherence Dynamics and Quantum Phase Transition*, to appear soon (2011).

[HCR07] B. Horstmann, J.I. Cirac, and T. Roscilde, *Dynamics of localization phenomena for hard-core bosons in optical lattices*, Phys. Rev. A **76**, 043625 (2007).

[HDR10] B. Horstmann, S. Dürr, and T. Roscilde, *Localization of Cold Atoms in State-Dependent Optical Lattices via a Rabi Pulse*, Phys. Rev. Lett. **105**, 160402 (2010).

[Hei25] W. Heisenberg, *Über quantentheoretische Umdeutung kinematischer und mechanischer Beziehungen*, Zeitschrift für Physik **33**, 879 (1925).

[Hor07] B. Horstmann, *Dynamics of localization phenomena for hard-core bosons in optical lattices*, Diplomarbeit, Friedrich-Schiller Universität Jena (2007).

[HHJ+10] D. Hanneke, J.P. Home, J.D. Jost, J.M. Amini, D. Leibfried, and D.J. Wineland, *Realization of a programmable two-qubit quantum processor*, Nature Physics **6**, 13 (2010).

[HRF+10] B. Horstmann, B. Reznik, S. Fagnocchi, and J.I. Cirac, *Hawking Radiation from an Acoustic Black Hole on an Ion Ring*, Phys. Rev. Lett **104**, 250403 (2010).

[HSR+11] B. Horstmann, R. Schützhold, B. Reznik, S. Fagnocchi, and J.I. Cirac, *Hawking Radiation on an Ion Ring in the Quantum Regime*, New J. Phys. **13**, 045008 (2011).

[HT00] Y. Himemoto and T. Tanaka, *Generalization of the model of Hawking radiation with modified high frequency dispersion relation*, Phys. Rev. D **61**, 064004 (2000).

[Ish72] K. Ishii, *Localization of eigenstates and transport phenomena in the one-dimensional disordered system*, Suppl. Progr. Theor. Phys. **53**, 77 (1972).

[Jac91] T. Jacobson, *Black-hole evaporation and ultrashort distances*, Phys. Rev. D **44**, 1731 (1991).

[JBC+98] D. Jaksch, C. Bruder, J.I. Cirac, C.W. Gardiner, and P. Zoller, *Cold bosonic atoms in optical lattices*, Phys. Rev. Lett. **81**, 3108 (1998).

[JBC+99] D. Jaksch, H.-J. Briegel, J.I. Cirac, C.W. Gardiner, and P. Zoller, *Entanglement of Atoms via Cold Controlled Collisions*, Phys. Rev. Lett. **82**, 1975 (1999).

[JM99] T.A. Jacobson and D. Mattingly, *Hawking radiation on a falling lattice*, Phys. Rev. D. **61**, 024017 (1999).

[JV98] T.A. Jacobson and G.E. Volovik, *Event horizons and ergoregions in ^3He*, Phys. Rev. D **58**, 064021 (1998).

[JVD+03] E. Jané, G. Vidal, W. Dür, P. Zoller, and J.I. Cirac, *Simulation of quantum dynamics with quantum optical systems*, Quant. Inform. Comput. **3**, 15 (2003).

[JZ04] D. Jaksch and P. Zoller, *The cold atom Hubbard toolbox*, Annals of Physics **315**, 52 (2005).

[KBD+08] B. Kraus, H.P. Büchler, S. Diehl, A. Kantian, A. Micheli, and P. Zoller, *Preparation of entangled states by quantum Markov processes*, Phys. Rev. A **78**, 042307 (2008).

[KCK+10] K. Kim, M.-S. Chang, S. Korenblit, R. Islam, E.E. Edwards, J.K. Freericks, G.-D. Lin, L.-M. Duan, and C. Monroe, *Quantum simulation of frustrated Ising spins with trapped ions*, Nature **465**, 590 (2010).

[KIB93] V.E. Korepin, A.G. Izergin, and N.M. Bogoliubov, *Quantum Inverse Scattering Method and Correlation Functions*, Cambridge University Press (1993).

[KM93] B. Kramer and A. MacKinnon, *Localization: theory and experiment*, Rep. Prog. Phys. **56**, 1469 (1993).

[KMD+05] R.C. Kuhn, C. Miniatura, D. Delande, O. Sigwarth, and C.A. Müller, *Localization of Matter Waves in Two-Dimensional*

Disordered Optical Potentials, Phys. Rev. Lett. **95**, 250403 (2005).

[KMJ+10] H. Krauter, C.A. Muschik, K. Jensen, W. Wasilewski, J.M. Petersen, J.I. Cirac, and E.S. Polzik, *Entanglement generated by dissipation*, arXiv:1006.4344 (2010).

[KWW04] T. Kinoshita, T.R. Wenger, and D.S. Weiss, *Observation of a One-Dimensional Tonks-Girardeau Gas*, Science **305**, 1125 (2004).

[LCB+07] P. Lugan, D. Clément, P. Bouyer, A. Aspect, M. Lewenstein, and L. Sanchez-Palencia, *Ultracold Bose Gases in 1D Disorder: From Lifshits Glass to Bose-Einstein Condensate*, Phys. Rev. Lett **98**, 170403 (2007).

[LFM+05] J.E. Lye, L. Fallani, M. Modugno, D.S. Wiersma, C. Fort, and M. Inguscio, *Bose-Einstein Condensate in a Random Potential*, Phys. Rev. Lett. **95**, 070401 (2005).

[LIB+10] O. Lahav, A. Itah, A. Blumkin, C. Gordon, S. Rinott, A. Zayats, and J. Steinhauer, *Realization of a Sonic Black Hole Analog in a Bose-Einstein Condensate*, Phys. Rev. Lett. **105**, 240401 (2010).

[Lin76] G. Lindblad, *On the generators of quantum dynamical semigroups*, Commun. Math. Phys. **48**, 119 (1976).

[LP00] U. Leonhardt and P. Piwnicki, *Relativistic Effects of Light in Moving Media with Extremely Low Group Velocity*, Phys. Rev. Lett. **84**, 822 (2000).

[LSA+07] M. Lewenstein, A. Sanpera, V. Ahufinger, B. Damski, A. Sen(de), and U. Sen, *Ultracold atomic gases in optical lattices: mimicking condensed matter physics and beyond*, Adv. Phys. **56**, 243 (2007).

[LSM61] E. Lieb, T. Schultz, and D. Mattis, *Two soluble models of an antiferromagnetic chain*, Annals of Physics (NY) **16**, 407 (1961).

[MDW02] K.W. Miller, S. Dürr, and C.E. Wieman, *RF-induced Sisyphus cooling in an optical dipole trap*, Phys. Rev. A **66**, 023406 (2002).

[MGW+03] O. Mandel, M. Greiner, A. Widera, T. Rom, T.W. Hänsch, and I. Bloch, *Controlled collisions for multi-particle entanglement of optically trapped atoms*, Nature **425**, 937 (2003).

[MMK+95] C. Monroe, D.M. Meekhof, B.E. King, S.R. Jefferts, W.M. Itano, and D.J. Wineland, *Resolved-Sideband Raman Cooling of a Bound Atom to the 3D Zero-Point Energy*, Phys. Rev. Lett. **75**, 4011 (1995).

[MP08] F. Marquardt and A. Püttmann, *Introduction to dissipation and decoherence in quantum systems*, arxiv:0809.4404 (2008).

[MP09a] J. Macher and R. Parentani, *Black-hole radiation in Bose-Einstein condensates*, Phys. Rev. A **80**, 043601 (2009).

[MP09b] J. Macher and R. Parentani, *Black/white hole radiation from dispersive theories*, Phys. Rev. D **79**, 124008 (2009).

[MPC10] C.A. Muschik, E.S. Polzik, and J.I. Cirac, *Dissipatively driven entanglement of two macroscopic atomic ensembles*, arXiv:1007.2209 (2010).

[PC04] D. Porras and J.I. Cirac, *Effective Quantum Spin Systems with Trapped Ions*, Phys. Rev. Lett. **92**, 207901 (2004).

[PCC11] F. Pastawski, L. Clemente, and J.I. Cirac, *Quantum memories based on engineered dissipation*, Phys. Rev. A **83**, 012304 (2011).

[PKR+08] T.G. Philbin, C. Kuklewicz, S. Robertson, S. Hill, F. König, and U. Leonhardt, *Fiber-Optical Analog of the Event Horizon*, Science **319**, 1367 (2008).

[PMD+08] D. Porras, F. Marquardt, J. von Delft, and J.I. Cirac, *Mesoscopic spin-boson models of trapped ions*, Phys. Rev. A **78**, 010101(R) (2008).

[PMW+10] M. Pasienski, D. McKay, M. White, and B. DeMarco, *A disordered insulator in an optical lattice*, Nature Physics **10**, 1038 (2010).

[PO56] O. Penrose and L. Onsager, *Bose-Einstein Condensation and Liquid Helium*, Phys Rev. **104**, 576 (1956).

[Pop00] S. Popescu, personal communication.

[Pro08] T. Prosen, *Third quantization: a general method to solve master equations for quadratic open Fermi systems*, New J. Phys. **10**, 043026 (2008).

[Pro10] T. Prosen, *Spectral theorem for the Lindblad equation for quadratic open fermionic systems*, J. Stat. Mech. (2010) P07020.

[PS02] C.J. Pethick and H. Smith, *Bose-Einstein-Condensation in Dilute Gases*, Cambridge University Press (2002).

[PVC05] B. Paredes, F. Verstraete, and J.I. Cirac, *Exploiting Quantum Parallelism to Simulate Quantum Random Many-Body Systems*, Phys. Rev. Lett. **95**, 140501 (2005).

[PWM+04] B. Paredes, A. Widera, V. Murg, O. Mandel, S. Fölling, J.I. Cirac, G.V. Shlyapnikov, T.W. Hänsch, and I. Bloch, *Tonks-Girardeau gas of ultracold atoms in an optical lattice*, Nature **429**, 277 (2004).

[PZ05] T. Prosen and M. Znidaric, *Matrix product simulations of non-eqilibrium steady states of quantum spin chains*, J. Stat. Mech. (2009) P02035.

[RB03a] R. Roth and K. Burnett, *Ultracold bosonic atoms in two-colour superlattices*, J. Opt. B **5**, S50 (2003).

[RB03b] R. Roth and K. Burnett, *Phase diagram of bosonic atoms in two-color superlattices*, Phys. Rev. A **68**, 023604 (2003).

[RC07] T. Roscilde and J.I. Cirac, *Quantum emulsion: a glassy phase of bosonic mixtures in optical lattices*, Phys. Rev. Lett. **98**, 190402 (2007).

[RCB05] A. Retzker, J.I. Cirac, and B. Reznik, *Detecting Vacuum Entanglement in a Linear Ion Trap*, Phys. Rev. Lett. **94**, 050504 (2005).

[RDF+08] G. Roati, C. D'Errico, L. Fallani, M. Fattori, C. Fort, M. Zaccanti, G. Modugno, M. Modugno, and M. Inguscio, *Anderson localization of a non-interacting Bose-Einstein condensate*, Nature **453**, 895 (2008).

[Rez00] B. Reznik, *Origin of the thermal radiation in a solid-state analogue of a black hole*, Phys. Rev. D **62**, 044044 (2000).

[RM04a] M. Rigol and A. Muramatsu, *Universal properties of hard-core bosons confined on one-dimensional lattices*, Phys. Rev. A **70**, 031603(R) (2004).

[RM04b] M. Rigol and A. Muramatsu, *Emergence of quasi-condensates of hard-core bosons at finite momentum*, Phys. Rev. Lett. **93**, 230404 (2004).

[RM05a] M. Rigol and A. Muramatsu, *Ground-state properties of hard-core bosons confined on one-dimensional optical lattices*, Phys. Rev. A **72**, 013604 (2005).

[RM05b] M. Rigol and A. Muramatsu, *Emergence of quasi-condensates of hard-core bosons at finite momentum*, Phys. Rev. Lett. **94**, 240403 (2005).

[RMM+08] G. Rousseaux, C. Mathis, P. Maissa, T.G. Philbin, and U. Leonhardt, *Observation of negative-frequency waves in a water tank: a classical analogue to the Hawking effect?*, New J. Phys. **10**, 053015 (2008).

[RRC10] M. Roncaglia, M. Rizzi, and J.I. Cirac, *Pfaffian State Generation by Strong Three-Body Dissipation*, Phys. Rev. Lett. **104**, 096803 (2010).

[RSC06] A.M. Rey, I.I. Satija, and C.W. Clark, *Quantum coherence of hard-core bosons: Extended, glassy, and Mott phases*, Phys. Rev. A **73**, 063610 (2006).

[Sac99] S. Sachdev, *Quantum Phase Transitions*, Cambridge University Press (1999).

[San06] L. Sanchez-Palencia, *Smoothing effect and delocalization of interacting Bose-Einstein condensates in random potentials*, Phys. Rev. A **74**, 053625 (2006).

[SBL+08] N. Syassen, D.M. Bauer, M. Lettner, T. Volz, D. Dietze, J.J. García-Ripoll, J.I. Cirac, G. Rempe, and S. Dürr, *Strong Dissipation Inhibits Losses and Induces Correlations in Cold Molecular Gases*, Science **320**, 1329 (2008).

[Sch06] R. Schützhold, *Detection Scheme for Acoustic Quantum Radiation in Bose-Einstein Condensates*, Phys. Rev. Lett. **97**, 190405 (2006).

[Sch26] E. Schrödinger, *Quantisierung als Eigenwertproblem*, Annalen der Physik **384**, 361 (1926).

[SCL+07] L. Sanchez-Palencia, D. Clément, P. Lugan, P. Bouyer, G.V. Shlyapnikov, and A. Aspect, *Anderson Localization of Expanding Bose-Einstein Condensates in Random Potentials*, Phys. Rev. Lett. **98**, 210401 (2007).

[SDK+05] T. Schulte, S. Drenkelforth, J. Kruse, W. Ertmer, J. Arlt, K. Sacha, J. Zakrzewski, and M. Lewenstein, *Routes Towards Anderson-Like Localization of Bose-Einstein Condensates in Disordered Optical Lattices*, Phys. Rev. Lett. **95**, 170411 (2005).

[SDK+06] T. Schulte, S. Drenkelforth, J. Kruse, R. Tiemeyer, K. Sacha, J. Zakrzewski, M. Lewenstein, W. Ertmer, and J.J. Arlt, *Analysis of localization phenomena in weakly interacting disordered lattice gases*, New J. Phys. **8**, 230 (2006).

[SFS+09] H. Schmitz, A. Friedenauer, C. Schneider, R. Matjeschk, M. Enderlein, T. Huber, J. Glückert, D. Porras, and T. Schätz, *The 'arch' of simulating quantum spin systems with trapped ions*, Appl. Phys. B **95**, 195 (2009).

[Sho94] P.W. Shor, *Polynomial-Time Algorithms for Prime Factorization and Discrete Logarithms on a Quantum Computer*,

Proceedings of the 35th Annual Symposium on Foundations of Computer Science, Santa Fe, NM 20 (1994).

[Sho95] P.W. Shor, *Scheme for reducing decoherence in quantum computer memory*, Phys. Rev. A **52**, 2493 (1995).

[SKS+04] A. Sanpera, A. Kantian, L. Sanchez-Palencia, J. Zakrzewski, and M. Lewenstein, *Atomic Fermi-Bose Mixtures in Inhomogeneous and Random Lattices: From Fermi Glass to Quantum Spin Glass and Quantum Percolation*, Phys. Rev. Lett **93**, 040401 (2004).

[SPL10] L. Sanchez-Palencia and M. Lewenstein, *Disordered quantum gases under control*, Nature Physics **6**, 87 (2010).

[SRH07] P. Sengupta, A. Raghavan, and S. Haas, *Disorder-enhanced phase coherence in trapped bosons on optical lattices*, New J. Phys. **9**, 103 (2007).

[SS00] H. Saida and M. Sakagami, *Black hole radiation with high frequency dispersion*, Phys. Rev. D **61**, 084023 (2000).

[SSH01] T. Schätz, U. Schramm, and D. Habs, *Crystalline ion beams*, Nature **412**, 717 (2001).

[SU05] R. Schützhold and W.G. Unruh, *Hawking Radiation in an Electromagnetic Waveguide?*, Phys. Rev. Lett **95**, 031301 (2005).

[SU08] R. Schützhold and W.G.Unruh, *Origin of the particles in black hole evaporation*, Phys. Rev. D **78**, 041504 (2008).

[SU10] R. Schützhold and W.G. Unruh, *Quantum correlations across the black hole horizon*, Phys. Rev. D **81**, 124033 (2010).

[SVB+08] K. Southwell, V. Vedral, R. Blatt, D. Wineland, I. Bloch, H.J. Kimble, J. Clarke, F.K. Wilhelm, R. Hanson, and D.D. Awschalom, *Quantum coherence*, Nature **453**, 1003 (2008).

[SWE+10] J.F. Sherson, C. Weitenberg, M. Endres, M. Cheneau, I. Bloch, and S. Kuhr, *Single-atom-resolved fluorescence imaging of an atomic Mott insulator*, Nature **467**, 68 (2010).

[Tho74] D.J. Thouless, *Electrons in disordered systems and the theory of localization*, Phys. Rep. **13**, 93 (1974).

[Unr81] W.G. Unruh, *Experimental Black-Hole Evaporation?*, Phys. Rev. Lett. **46**, 1351 (1981).

[Unr95] W.G. Unruh, *Sonic analogue of black holes and the effects of high frequencies on black hole evaporation*, Phys. Rev. D **51**, 2827 (1995).

[US03] W.G. Unruh and R. Schützhold, *On slow light as a black hole analogue*, Phys. Rev. D **68**, 024008 (2003).

[US05] W.G. Unruh and R. Schützhold, *Universality of the Hawking effect*, Phys. Rev. D **71**, 024028 (2005).

[VGC04] F. Verstraete, J.J. Garcia-Ripoll, and J.I. Cirac, Phys. Rev. Lett. **93** 207204 (2004).

[VW02] G. Vidal and R.F. Werner, *Computable measure of entanglement*, Phys. Rev. A **65**, 032314 (2002).

[VWC09] F. Verstraete, M.M. Wolf, and J.I. Cirac, *Quantum computation and quantum-state engineering driven by dissipation*, Nature Physics **5**, 633 (2009).

[WGK+04] M.M. Wolf, G. Giedke, O. Krüger, R.F. Werner, and J.I. Cirac, *Gaussian entanglement of formation*, Phys. Rev. A **69**, 052320 (2004).

[Wic50] G.C. Wick, *The Evaluation of the Collision Matrix*, Phys. Rev. **80**, 268 (1950).

[WKB+92] I. Waki, S. Kassner, G. Birkl, and H.I. Walther, *Observation of ordered structures of laser-cooled ions in a quadrupole storage ring*, Phys. Rev. Lett. **68**, 2007 (1992).

[WMI+98] D.J. Wineland, C. Monroe, W.M. Itano, D. Leibfried, B.E. King, and D.M. Meekhof, *Experimental issues in coherent quantum-state manipulation of trapped atomic ions*, J. Res. Natl. Inst. Stand. Technol. **103**, 259 (1998).

[WPM+09] M. White, M. Pasienski, D. McKay, S.Q. Zhou, D. Ceperley, and B. DeMarco, *Strongly Interacting Bosons in a Disordered Optical Lattice*, Phys. Rev. Lett. **102**, 055301 (2009).

[WTP+11] S. Weinfurtner, E.W. Tedford, M.C.J. Penrice, W.G. Unruh, and G.A. Lawrence, *Measurement of Stimulated Hawking Emission in an Analogue System*, Phys. Rev. Lett. **106**, 021302 (2011).

[ZBB+05] P. Zoller, Th. Beth, D. Binosi, R. Blatt, H. Briegel, D. Bruss, T. Calarco, J.I. Cirac, D. Deutsch, J. Eisert, A. Ekert, C. Fabre, N. Gisin, P. Grangiere, M. Grassl, S. Haroche, A. Imamoglu, A. Karlson, J. Kempe, L. Kouwenhoven, S. Kröll, G. Leuchs, M. Lewenstein, D. Loss, N. Lütkenhaus, S. Massar, J.E. Mooij, M.B. Plenio, E. Polzik, S. Popescu, G. Rempe, A. Sergienko, D. Suter, J. Twamley, G. Wendin, R. Werner, A. Winter, J. Wrachtrup, and A. Zeilinger, *Quantum information processing and communication. Strategic report on current status, visions and goals for research in Europe.*, Eur. Phys. J. D **36**, 203 (2005).

Acknowledgments

Most importantly, I would like to thank my thesis supervisor J. Ignacio Cirac for the support he provided me during my thesis. My projects have been made possible by his great ideas and I profited a lot from his connections with clever scientists. It is remarkable that such an ingeneous physicist is able to create an environment which is very stimulating scientifically and personally at the same time. I am deeply grateful that he has given me the opportunity to perform research among so many motivated people at the Max-Planck-Institute for Quantum Optics (MPQ).

My thanks also extend to my co-authors. Tommaso Roscilde gave me a lot of guidance for research in general and for my works on the realization of disordered potentials in optical lattices in particular. These projects benefited from his great knowledge of condensed matter phenomena and numerical techniques. In this context I would like to thank Stephan Dürr for contributing his ideas about dynamical doping and supporting us with his deep knowledge of ultracold atomic systems.

Tommaso also supported my thinking about decoherence dynamics. I am thankful to Michael Wolf for contributing his ideas to this project. The project about the simulation of black holes is a collaboration with Benni Reznik, Serena Faggnocchi, and Ralph Schützhold. I have learnt a lot from Benni and Serena about analog black holes and am very thankful for the intense and fruitful discussions with them.

I would especially like to thank all the people that stimulated me scientifically and privately at the MPQ. In random order I want to mention: Toby Cubitt, Norbert Schuch, Tassilo Keilmann, Juan-Jose Garcia-Ripoll, Valentin Murg, Geza Giedke, Mari-Carmen Banuls, Henning Christ, Maria Eckholt-Perotti, Christine Muschik, Verena Maier, Oliver Buerschaper, Dominik Bauer, Matthias Lechner, Diego Porras, Fernando Pastawski, Veronika Lechner, Eric Kessler, Heike Schwager, Matteo Rizzi, Leonardo Mazza, Anika Pflanzer, Michael Lubasch, and Tobias Schätz. Unfortu-

nately, there would not be enough space to prize their contributions in depths.

I have received the most important motivation for my thesis from my officemates: Toby Cubitt, Maria Eckholt-Perotti, Christine Muschik, Leonardo Mazza, and Anika Pflanzer. I will always remember discussing about cycling with Toby, dancing with Christine, eating Italian dinner and watching movies with Leonardo, and last but certainly not least talking with Anika and Maria.

Despite the help of all these people, finishing my PhD was only possible with the support of my family. I thank my parents for their helping hands and my sister Birte for always listening to me.

I gratefully acknowledge funding from the Nano Systems Intitative Munich.